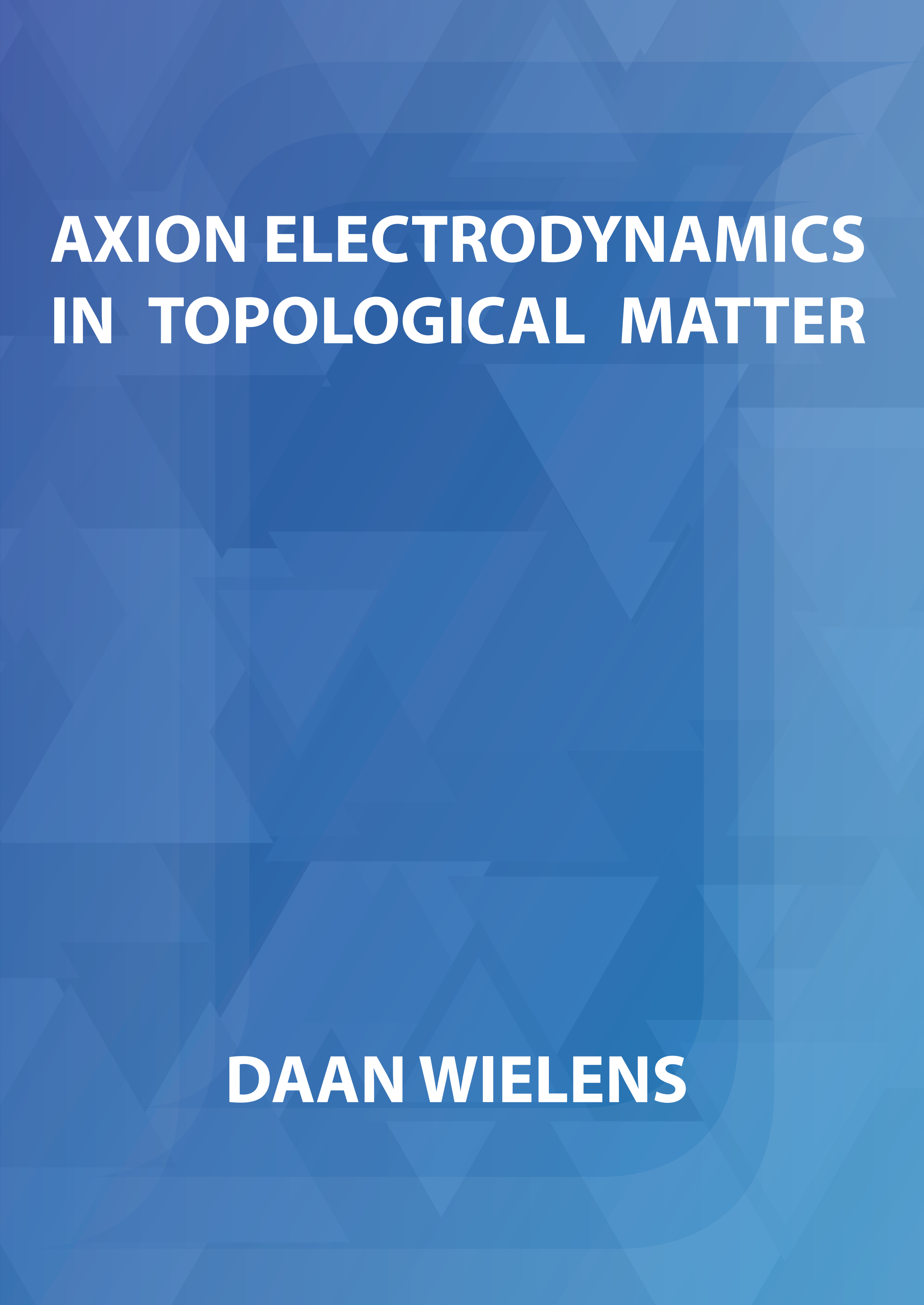

AXION ELECTRODYNAMICS IN TOPOLOGICAL MATTER

DAAN WIELENS

AXION ELECTRODYNAMICS IN TOPOLOGICAL MATTER

Daan Wielens

AXION ELECTRODYNAMICS IN TOPOLOGICAL MATTER

DISSERTATION

to obtain
the degree of doctor at the University of Twente,
on the authority of the Rector Magnificus,
prof. dr. ir. A. Veldkamp,
on account of the decision of the doctorate board,
to be publicly defended
on Thursday the 4th of November, 2021, at 14:45
by

Daan Harm Wielens

born on the 25th of December, 1993
in Enschede, the Netherlands

This dissertation has been approved by:

Promotor:
prof. dr. ir. A. Brinkman

And co-promotor:
dr. C. Li

The work described in this thesis was carried out in the Quantum Transport in Matter group, MESA+ Institute for Nanotechnology, University of Twente, the Netherlands.

This work was financially supported by NWO through a VICI grant.

Axion electrodynamics in topological matter
PhD Thesis, University of Twente
Printed by: GildePrint Drukkerijen, Enschede, the Netherlands
ISBN: 978-90-365-5270-7
DOI: 10.3990/1.9789036552707

© D.H. Wielens, 2021.
All rights reserved. No parts of this thesis may be reproduced, stored in a retrieval system or transmitted in any form or by any means without permission of the author.
Alle rechten voorbehouden. Niets uit deze uitgave mag worden vermenigvuldigd, in enige vorm of op enige wijze, zonder voorafgaande schriftelijke toestemming van de auteur.

Doctorate Board:

Chair and secretary:	
prof. dr. J.L. Herek	University of Twente
Promotor:	
prof. dr. ir. A. Brinkman	University of Twente
Co-promotor:	
dr. C. Li	University of Twente
Members:	
prof. dr. J. van den Brink	Leibniz Institute for Solid State and Materials Research Dresden
dr. E van Heumen	University of Amsterdam
prof. dr. ir. J.W.M. Hilgenkamp	University of Twente
dr. ir. M.P. de Jong	University of Twente
prof. dr. A.V. Kimel	Radboud University
prof. dr. T.T.M. Palstra	University of Twente

Contents

Chapter 1

Introduction

The electric and magnetic fields have always played important roles in our civilization, from the first simple compasses to the intricate electrical circuits in computer chips. While downsizing transistors on computer chips has led to better performances for decades, fundamental limits are hampering further improvements, such that alternative material platforms to current silicon-based technology become of great interest. We study topological materials, which host exotic properties and have unique electromagnetic properties, as a candidate for a new generation of electronic devices.

1.1 Electrodynamics

Electric and magnetic phenomena have interested and inspired mankind for millennia. Electric phenomena can be found everywhere in nature, from the violent discharge during a lightning strike to the defense mechanism of electric animals such as electric eels and rays, but the utilization of electric phenomena only started a few centuries ago. The direct observation of magnetic phenomena in nature is less straightforward, but applications of magnetism were already found long ago when naturally magnetized materials were used as compasses [1].

Up to the 19th century, electric and magnetic phenomena were two unrelated subjects. It was Ørsted who noticed in 1820 that an electric current can deflect a compass needle and thereby discovered the connection between electricity and magnetism. A few decades after Ørsted's discovery, aided by important work from Ampère and Faraday, it was Maxwell who unified the laws of electricity and magnetism into what is known as Maxwell's equations [2].

The importance of the understanding of (the interplay between) electric and magnetic fields has led to countless applications. An early example of this is Faraday's dynamo, that served as a basis for the electric generator, a device that is used in power plants to generate the electricity that drives our current society. A more recent example is the transistor, a three-terminal device where the flow of an electrical current between two terminals (the source and drain) is controlled by an electric field that is generated by the third terminal, the gate. By modulating the voltage on the gate, there can be a finite current flowing from source to drain (the 'on' state, denoted by 1) or no current (the 'off' state, denoted by 0). Computer chips house billions of transistors, closely packed in complicated circuits at the nanometer scale, and with chips being integrated in virtually every powered device, it is once again clear that understanding the laws of electrodynamics is crucial in the modern age.

1.2 Axion physics

During Maxwell's work on unifying the equations for electrodynamics, he found that the electromagnetic fields travel at the speed of light, and as such postulated that light itself must be a form of electromagnetic radiation. With the proof of Hertz in 1888 that radio waves exist and hence that the visible spectrum of light is only a small portion of electromagnetic radiation, scientists have been using and detecting electromagnetic radiation for all kinds of experiments, ranging from x-ray scans in hospitals to detecting radiation from outer space.

To see where axion physics comes into play, we consider a different branch of physics that also examines the universe and outer space: the realm of particle physics. Here, fundamental interactions between elementary particles are investigated in the framework of quantum field theory, where the electrodynamics of Maxwell was recast into quantum mechanical terms.

It is the quantum field theory[1] where a particle called 'axion' was first introduced in 1977 to explain the absence of charge-parity violation in the strong interaction between quarks [3]. Since then, the particle was proposed to be a candidate for dark matter [4] and several experimental setups have been proposed and/or realized to measure its existence [5–8], but no evidence has been found so far. Ten years after the theoretical proposal of the axion particle in quantum field theory, Wilczek proposed that the physics of axion particles may also be applied to condensed matter physics [9]. Another twenty years later, Qi *et al.* [10] discovered that the same concepts of the field theory can also be applied to a class of materials called topological insulators, where the axion-related term leads to a modification of the classical Maxwell's equations. These modifications result in new, unusual types of coupling between the electric and magnetic fields, called the topological magnetoelectric effect (TME), which we will introduce in detail in Chapter 2. Is is the aim of this thesis to set up experiments towards the possible detection of the topological magnetoelectric effect.

While the work presented in this thesis is quite fundamental, we wish to emphasize that different applications regarding the topological magnetoelectric effect have been proposed. The axion materials could be used for the detection of dark matter axions [11], where the axion dark matter couples to the axionic quasiparticles in the host topological insulator. Furthermore, the dynamical chiral magnetic effect in antiferromagnetic axion materials could be used for low-power electronics [12]. The axion field theoretical description has also been extended to include superconductors. Exotic effects of the electromagnetic field in a topological superconductor have been

---

[1] To be precise, the field of quantum chromodynamics. There are four known fundamental interactions, among which the well-known electromagnetism and gravity are two of them. The others are weak and strong interactions, where the latter concerns the forces that bind quarks into protons and neutrons. While quantum electrodynamics studies electromagnetic radiation (i.e. photons) and uses electric charge, quantum chromodynamics studies gluons and uses the notion of color.

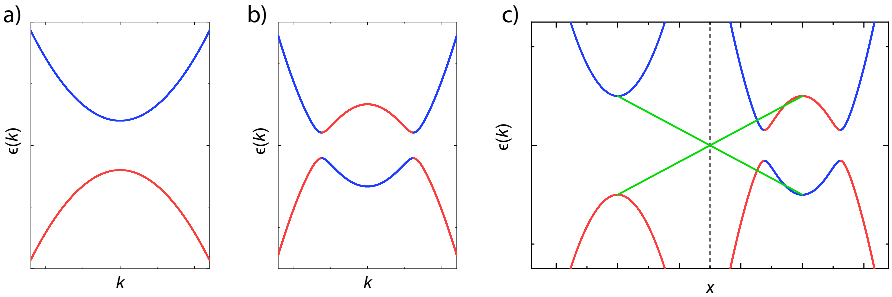

Figure 1.1: Schematic band structures of materials. **(a)** Band structure of a normal (i.e. trivial) insulator, where we show the energy ϵ as a function of momentum k. The red (blue) bands indicate the valence (conduction) bands of the material. **(b)** Band structure of a topological insulator. Due to various effects, including spin-orbit coupling, the bands are inverted. **(c)** Schematic picture of the surface states. Here, we plot the band structures of the trivial insulator (left) and topological insulator (right) as a function of real space position x. At the interface (denoted by the dashed gray line), bands of the same color must connect and thus surface states are formed.

predicted [13].

1.3 Topological insulators

In condensed matter physics we study the properties of materials. Atoms consist of a nucleus[2] which is surrounded by shells of electrons that circle around the atom's core. We typically focus on crystalline materials, i.e. materials in which the atoms form ordered and repetitive structures, i.e. a crystal lattice. While electrons of an isolated atom are located at quantized orbitals, these orbitals overlap when atoms are brought together, and they split into new orbitals. For a crystal, we have to consider many electrons and therefore the number of orbitals is huge. Since the spacing of adjacent orbitals is very small, for crystals we can consider this huge amount of closely spaced orbitals as a continuum and call it an energy band [14].

The electronic properties of a material are dominated by the valence electrons of the material. If the valence band (VB) is completely filled (i.e. all states are occupied) with electrons and an energy gap exists in the spectrum of bands between the valence band and the conduction band

---

[2] The nucleus contains protons and neutrons, which are composed of quarks, bound together by the gluons that we encounter in quantum chromodynamics.

(CB), so that there are no available states around the Fermi energy (see Fig. 1.1(a)), we call the material an insulator, while a material is called a metal when there are available states near the Fermi energy.

The order of the energy bands in materials is typically dictated by the energy of the individual atomic orbitals, but it can be altered by other effects. An effect that becomes pronounced in crystals containing heavy elements is spin-orbit coupling (SOC), which can lead to substantial shifts of energy levels within the band diagram. For certain materials, such as Bi-based compounds, two bands can even invert so that the order of the bands is changed (see Fig. 1.1(b)) [15]. Mathematically speaking, the order of bands can be described by a classification number called a topological invariant. Even though the bands are inverted, a band gap is still present due to hybridization of the bands, and as such these insulating materials are called topological insulators (TIs).

When a topological insulator is now brought into contact with a non-topological (i.e. trivial) insulator, these materials will have a different order of their bands. At the interface, the bands that originate from the same orbital must connect, and hence a band crossing is inevitable. The band crossing is shown in Fig. 1.1(c) in green and the resulting states are called surface states, since they live on the surface of the topological insulator[3]. The linearity of the energy versus momentum of the surface states resembles the linear dispersion relation that follows from the Dirac equation, and therefore the surface states are typically described as a Dirac cone. The peculiar result of having surface states means that while the bulk of the material is insulating, the surface of the material is conducting. The surface states have very interesting properties, such as the spin-momentum locking [16], and have various applications in spintronics [17, 18]. Topological insulators can also be doped with transition metal elements to create magnetic topological insulators. The prediction of the quantum anomalous Hall (QAH) state in 2010 [19] in magnetically doped topological insulators started the search for this novel effect, which was experimentally realized in 2013 [20]. While the QAH state is closely related to axion electrodynamics and thereby forms an interesting platform to study, it also has interesting applications of its own. The chiral edge modes could be used for dissipationless transport and microwave circuits [21]. Furthermore, combining superconductors with magnetic topological insulators can lead to Majorana edge

---

[3] Note that the picture combines bands in k-space with a representation in real space, which is by no means a true physical picture. One should simply take from the image that the bands of different colors (on both sides of the interface) need to connect.

modes, which have possible applications in quantum computing [22, 23].

1.4 Outline

Despite the fact that axion electrodynamics in topological matter was already introduced in 2008 [10], there has been no definitive experimental proof of the topological magnetoelectric effect so far. One of the most striking phenomena related to the TME was predicted in 2009 by Qi *et al.* [24], when it was proposed that an electric charge placed above a topological material would lead to a magnetic field that seems to originate from a magnetic monopole. This would violate Maxwell's equations, which stated that magnetic monopoles do not exist. In reality, as we will see in Chapter 2, the magnetic monopole response is more complex, but nevertheless the experimental observation of this field would be very interesting. In this thesis, we search for experimental signatures of the topological magnetoelectric effect in different types of topological materials.

We start our study in **Chapter 2** with a review of axion electrodynamics. We discuss the modifications to Maxwell's equations and see how the modifications change the coupling between the electric and magnetic fields when topological materials are introduced. We discuss the theory behind three experimental proposals that were designed to probe the topological magnetoelectric effect. We will describe the attempt to realize these experiments in Chapters 5-7.

In **Chapter 3** we introduce the thin film deposition of the topological insulator $(\mathrm{Bi}_{1-x}\mathrm{Sb}_x)_2\mathrm{Te}_3$ (BST) by molecular beam epitaxy. We discuss the deposition of the thin films and show that we are able to deposit the material on different substrates. We then develop methods for device fabrication, which will be used for all devices presented throughout this thesis. We finish the chapter with transport measurements on the BST thin films, in which we show that gate tuning the devices enables us to cross the Dirac point and have an inversion of carrier type, both of which are considered to be hallmark features of topological insulators. We furthermore perform measurements at low temperatures and find signatures of electron-electron interactions in our thin films.

The topological insulator thin films of Chapter 3 can be doped by transition metals, which is the main topic of **Chapter 4**. Thin films of magnetically doped topological insulators have been shown to exhibit the quantum anomalous Hall effect, and have further shown to have a connection to the axion electrodynamics and its topological magnetoelectric effect. In this chapter we review the theory of the quantum anomalous Hall effect and its requirements regarding the materials that can be used. We then discuss the deposition of thin films of vanadium-doped BST. We perform transport measurements on these films to understand the magnetic properties of our thin films, which are important for the experiments in Chapter 6, where we make use of these magnetic topological insulators.

In **Chapter 5** we perform the first experiment to search for signatures of the topological magnetoelectric effect. We make use of the Dirac semimetal $\mathrm{Bi}_{0.97}\mathrm{Sb}_{0.03}$, a topological material whose Dirac cones are a bulk property, rather than the surface Dirac states of topological insulators. We fabricate non-local devices to measure the chiral magnetic effect, in which parallel external electric and magnetic fields lead to a negative magnetoresistance. We find that the chiral charge polarization associated with this effect decays over a larger distance and thus can be distinguished from regular Drude transport, and as such find evidence for the chiral magnetic effect in $\mathrm{Bi}_{0.97}\mathrm{Sb}_{0.03}$.

The search for the aforementioned magnetic monopole is discussed in **Chapter 6**. We designed a novel measurement setup where a superconducting quantum interference device (SQUID) is placed above a magnetic topological insulator film in a dilution refrigerator. While the magnetic topological insulator thin films of Chapter 4 do not show the quantum anomalous Hall effect yet, we carefully investigate the measured magnetic flux from our devices as a function of the applied gate voltage. While we find no signature of the topological magnetoelectric effect in our experiments, we do notice a discrepancy between experiments where the devices are biased with a dc current or not. We find that heat dissipation of the devices causes the temperature-dependent magnetization to change, which is measured with our SQUID setup.

In **Chapter 7** we search for fractional charges originating from the TME when an array of superconducting islands with a hole in the array is placed on top of a topological insulator. The critical current of the device oscillates with the applied magnetic field and due to axion electrodynamics it is expected that extra oscillations with a period that is four times larger can be found in these devices, on top of the regular oscillations. We fabricate such arrays on an exfoliated flake of $\mathrm{BiSbTeSe}_2$ and on a reference, non-topological, Au thin film and find that the measured oscillations are in good agreement with a numerical model with a scaling prefactor. We do not find clear signatures of a topological magnetoelectric effect in the topological device. The limited size of the flake makes it hard to fabricate arrays with desirable dimensions, and with the thin films of BST as new platform we fabricate Josephson junctions on the thin films to study their properties.

Chapter 2

Review of axion electrodynamics in condensed matter physics

The field of axion electrodynamics first emerged in high energy physics and then found its way to the field of condensed matter physics when it was found that modifications to Maxwell's equations can be present near the boundaries of topological materials. In this chapter, we review the derivation of the equations governing axion electrodynamics, and then discuss the experimental proposals that form the basis of the upcoming Chapters 5-7. While the equations are well established already for a long time, their implications and the requirements for the observation of the topological magnetoelectric effects in topological matter are still under debate. We aim to give an overview of the recent advances and open questions within the field.

2.1 Introduction

The origin of a particle called 'axion' goes back to 1977, when it was postulated to solve the strong charge-parity problem in quantum chromodynamics [3]. The particle received its name half a year later, and was in fact named after a laundry detergent named Axion, as the particle 'cleaned up' a problem with an axial current [25, 26]. While axions are regarded as a form of dark matter in high energy physics [27], their existence has not been shown experimentally up to now. The notion of field theory was also applied to topological insulators in 2008, which led to the modification of the standard electrodynamics, called axion electrodynamics [10]. The implications of axion electrodynamics lie within the axion field, $\theta(\mathbf{r}, t)$, which enters the modified equations as a prefactor. While $\theta = 0$ for trivial materials, its value differs for topological materials [10, 12, 28–31]. While the actual value of θ for topological materials is usually regarded to be π within the topological insulator (TI), it is still under debate which materials fulfill the requirements for the observation of axion electrodynamics. Because of the unusual coupling between electric and magnetic fields that arises from axion electrodynamics, the different effects that can arise are usually unified under the name 'topological magnetoelectric effects' (TME).

In this chapter, we will start by reviewing the equations governing axion electrodynamics. These equations form the basis of the experiments of Chapters 5-7. Afterwards, we will discuss the theoretical aspects of each experiment in more detail. We then discuss the recent progress in the understanding of axion electrodynamics, which is still under debate at the moment of writing, and the requirements to observe it in topological matter. We finish the chapter with a discussion on recent experiments that probe the TME in several ways.

2.2 Derivation of axion electrodynamics

In this section, we aim to introduce the relevant results of axion electrodynamics in an intuitive way without introducing all details of field theory and Einstein notation. In our derivation, we start from the well-known set of Maxwell's equations [32],

$$
\begin{aligned}
\boldsymbol{\nabla} \cdot \mathbf{B} &= 0 \\
\boldsymbol{\nabla} \times \mathbf{E} &= -\frac{\partial \mathbf{B}}{\partial t} \\
\boldsymbol{\nabla} \cdot \mathbf{E} &= \frac{\rho}{\epsilon_0} \\
\boldsymbol{\nabla} \times \mathbf{B} &= \mu_0 \left(\mathbf{j} + \epsilon_0 \frac{\partial \mathbf{E}}{\partial t} \right).
\end{aligned} \tag{2.1}
$$

Here, $\mathbf{B}$ is the magnetic field, $\mathbf{E}$ is the electric field, ρ is the charge density, $\epsilon_0 = 8.854 \cdot 10^{-12}$ F/m is the permittivity of free space, $\mu_0 = 1.256 \cdot 10^{-6}$ H/m is the permeability of free space and $\mathbf{j}$ is the current density. Maxwell's equations unify the laws of electricity and magnetism and describe the electric and magnetic fields in the presence of charges, currents and fields that change over time. It is worth noting that while an electric charge (density) can lead to a electric monopole field, the magnetic counterpart simply states $\boldsymbol{\nabla} \cdot \mathbf{B} = 0$ and hence magnetic monopoles do not occur in nature. The first experimental proposal to measure an effect arising from axion electrodynamics was titled 'Inducing a Magnetic Monopole with Topological Surface States' [24] and hence this would violate the Maxwell's electrodynamics. To understand the nature - and subtleties of the experimental proposal - we need to understand electrodynamics when TIs are at hand.

2.2.1 Field theory

Maxwell's equations can also be expressed in terms of the scalar potential ϕ and the vector potential $\mathbf{A}$,

$$
\begin{aligned}
\mathbf{B} &= \boldsymbol{\nabla} \times \mathbf{A}, \\
\mathbf{E} &= -\boldsymbol{\nabla}\phi - \frac{\partial \mathbf{A}}{\partial t}.
\end{aligned} \tag{2.2}
$$

In field theoretical problems one usually has to consider both time and space, and as such 'four-vectors' are introduced. The scalar and vector potential are combined into a four-vector called the four-potential

$$
A^\mu = (\phi/c, \mathbf{A}). \tag{2.3}
$$

Greek letters, such as $\mu = 0, 1, 2, 3$, are used to indicate the indices over which one needs to perform a summation. Typically, $0 = t$, $1 = x$, $2 = y$, $3 = z$. Rather than writing down summations in every equation, one simplifies $y = \sum_{\mu=0}^{3} c_\mu x^\mu = c_0 x^0 + c_1 x^1 + c_2 x^2 + c_3 x^3$ into $y = c_\mu x^\mu$. In field theory, the electromagnetic tensor $F^{\mu\nu}$ plays a central role. It is defined in terms of the four-gradient $\partial^\mu = \left(\frac{1}{c}\frac{\partial}{\partial t}, -\boldsymbol{\nabla}\right)$ and the four-potential

$$F^{\mu\nu} = \partial^\mu A^\nu - \partial^\nu A^\mu. \tag{2.4}$$

The components of the electromagnetic tensor are given by

$$F^{\mu\nu} = \begin{pmatrix} 0 & -E_x/c & -E_y/c & -E_z/c \\ E_x/c & 0 & -B_z & B_y \\ E_y/c & B_z & 0 & -B_x \\ E_z/c & -B_y & B_x & 0 \end{pmatrix}. \tag{2.5}$$

To incorporate the sources into Maxwell's equations, the charge and current densities are introduced in the form of the four-current $J^\mu = (c\rho, \mathbf{j})$. Maxwell's equations can now be rewritten in terms of four-vectors as

$$\partial_\mu F^{\mu\nu} = \mu_0 J^\nu. \tag{2.6}$$

2.2.2 Lagrangian dynamics

Up to now, we have simply rewritten Maxwell's equations in a different formalism. To see how they involve into axion electrodynamics, we need to consider Lagrangian mechanics. Here, one considers a Lagrangian $L = T - V$, where T and V are the kinetic and potential energy, respectively. The Euler-Lagrange equations can be used to solve the system of equations and retrieve the equations of motion from a given Lagrangian.

In field theory, one uses Lagrangian densities. Typically, for Maxwell's equations, one considers the following Lagrangian density [33],

$$\mathcal{L}_0 = -\frac{1}{4\mu_0} F_{\mu\nu} F^{\mu\nu} - A_\mu J^\mu. \tag{2.7}$$

The first term comprises the electric and magnetic fields, the second term captures the sources. Note that if one rewrites this in terms of the more familiar electric and magnetic fields, one obtains $F_{\mu\nu}F^{\mu\nu} = F_{00}F^{00} + F_{01}F^{01} + \ldots + F_{33}F^{33} = 2\left(\mathbf{B}^2 - \frac{\mathbf{E}^2}{c^2}\right)$ and hence

$$\mathcal{L}_0 = \frac{1}{2}\left(\epsilon_0 \mathbf{E}^2 - \frac{1}{\mu_0}\mathbf{B}^2\right). \tag{2.8}$$

Solving the Euler-Lagrange equations for this Lagrangian density, yields Maxwell's equations of Eqn. 2.6 as the equations of motion, as expected.

For axion electrodynamics, it was proposed to add an extra term to the Lagrangian density, which has the form [3, 9]

$$\mathcal{L}_\theta = -\frac{\alpha\theta}{4\pi\mu_0} F_{\mu\nu}\tilde{F}^{\mu\nu}. \tag{2.9}$$

Here, $\alpha = \frac{1}{4\pi\epsilon_0}\frac{e^2}{\hbar c}$ is the fine-structure constant, θ is the axion field and $\tilde{F}^{\mu\nu}$ is the dual tensor[1]. Rewriting the Lagrangian density in terms of electric and magnetic fields reveals the unusual coupling between the electric and magnetic fields, which is the most important implication of axion electrodynamics, and which is often introduced in literature in the following form [9, 15, 24, 30, 33, 34],

$$\mathcal{L}_\theta = \frac{\theta}{2\pi}\frac{\alpha}{2\pi}\mathbf{E}\cdot\mathbf{B}. \tag{2.10}$$

The axion Lagrangian density can also be solved through the Euler-Lagrange equation. If one considers a θ which is independent of space and time (such as for all trivial matter), one finds that the axion Lagrangian density does not alter Maxwell's equations [35]. Note that this implies that the electromagnetic fields in the bulk of a TI are not changed. However, if one allows θ to vary in space or time, the Euler-Lagrange equation does yield a different result. Such changes are found at the interfaces of TIs and trivial materials, where θ must change from π to 0. To obtain the modifications to Maxwell's equations, one can solve the Euler-Lagrange equation for the full Lagrangian density $\mathcal{L} = \mathcal{L}_0 + \mathcal{L}_\theta$ and find

$$\partial_\mu\left(F^{\mu\nu} + \kappa\theta\tilde{F}^{\mu\nu}\right) = \mu_0 J^\nu. \tag{2.11}$$

Here, $\kappa \equiv \alpha/\pi$. The fact that we allowed $\theta = \theta(\mathbf{r}, t)$ to vary in space and time results in the second term of the l.h.s., which will lead to additional terms in Maxwell's equations.

2.2.3 Axion electrodynamics

We can rewrite Eqn. 2.11 in terms of **E** and **B** fields by choosing specific values of μ and ν. For example, when we consider $\nu = 0$, the results of the

---

[1] It is convenient to think of the dual tensor as a version of the electromagnetic tensor in Eqn. 2.5 with the positions of the electric and magnetic fields being interchanged.

summation of μ becomes

$$\begin{aligned}\partial_0\left(F^{00}+\kappa\theta\tilde{F}^{00}\right)+\partial_1\left(F^{10}+\kappa\theta\tilde{F}^{10}\right)+\partial_2\left(F^{20}+\kappa\theta\tilde{F}^{20}\right)&\\ +\partial_3\left(F^{30}+\kappa\theta\tilde{F}^{30}\right)&=\mu_0 J^0\\ \frac{\partial}{\partial x}\left(\frac{E_x}{c}+\kappa\theta B_x\right)+\frac{\partial}{\partial y}\left(\frac{E_y}{c}+\kappa\theta B_y\right)+\frac{\partial}{\partial z}\left(\frac{E_z}{c}+\kappa\theta B_z\right)&=\mu_0 c\rho.\end{aligned} \tag{2.12}$$

The electric field components make up the divergence of the field; the magnetic field is multiplied by θ which also depends on position, so that we have to use the product rule. We end up with

$$\frac{1}{c}\boldsymbol{\nabla}\cdot\mathbf{E}+\kappa\left[\boldsymbol{\nabla}\theta\cdot\mathbf{B}+\theta(\boldsymbol{\nabla}\cdot\mathbf{B})\right]=\mu_0 c\rho. \tag{2.13}$$

Since $\boldsymbol{\nabla}\cdot\mathbf{B}=0$ is still valid[2], this reduces to

$$\boldsymbol{\nabla}\cdot\mathbf{E}+\kappa c\boldsymbol{\nabla}\theta\cdot\mathbf{B}=\frac{\rho}{\epsilon_0}. \tag{2.14}$$

We follow a similar procedure for $\nu=1,2,3$ and combine these results in a vector equation to obtain

$$\boldsymbol{\nabla}\times(c\mathbf{B}-\kappa\theta\mathbf{E})=c\mu_0\mathbf{j}+\frac{1}{c}\frac{\partial}{\partial t}\left(\mathbf{E}+\kappa\theta c\mathbf{B}\right). \tag{2.15}$$

The source-free Maxwell equations are not changed, and therefore the new set of equations is

$$\begin{aligned}\boldsymbol{\nabla}\cdot\mathbf{E}+\kappa c\boldsymbol{\nabla}\theta\cdot\mathbf{B}&=\frac{\rho}{\epsilon_0}\\ \boldsymbol{\nabla}\times(c\mathbf{B}-\kappa\theta\mathbf{E})&=c\mu_0\mathbf{j}+\frac{1}{c}\frac{\partial}{\partial t}\left(\mathbf{E}+\kappa\theta c\mathbf{B}\right)\\ \boldsymbol{\nabla}\cdot\mathbf{B}&=0\\ \boldsymbol{\nabla}\times\mathbf{E}&=-\frac{\partial\mathbf{B}}{\partial t}.\end{aligned} \tag{2.16}$$

We can modify the equations such that the axion terms are on the r.h.s.,

$$\boldsymbol{\nabla}\times c\mathbf{B}=\mu_0\left[\mathbf{j}+\epsilon_0\frac{\partial\mathbf{E}}{\partial t}+\mathbf{j}_\theta\right], \tag{2.17}$$

---

[2] We have used the fact that two source-free equations of Maxwell's equations do not change under the addition of the axion Lagrangian [33].

where

$$\mathbf{j}_\theta \equiv \frac{\kappa}{\mu_0 c}\left(\boldsymbol{\nabla}\times\theta\mathbf{E}+\frac{\partial}{\partial t}\theta\mathbf{B}\right) \tag{2.18}$$

is the axion current density. Similarly,

$$\boldsymbol{\nabla}\cdot\mathbf{E}=\frac{1}{\epsilon_0}\left[\rho+\rho_\theta\right], \tag{2.19}$$

where

$$\rho_\theta \equiv -\epsilon_0\kappa c\boldsymbol{\nabla}\theta\cdot\mathbf{B} \tag{2.20}$$

is the axion charge density.

Thus, Eqns. 2.17 and Eqns. 2.19 capture axion electrodynamics by including the axion current and charge densities to the Maxwell's equations. For trivial systems, where $\theta = 0$, they simply vanish, while for topological materials, where $\theta = \pi$, the modifications lead to new effects. Eqns. 2.18 and 2.20 show that the effects occur due to spatial or temporal variations in θ. In the following sections, we will discuss the implications of these variations in θ, along with experimental proposals to detect the effects.

2.3 Inducing magnetic monopoles

The first proposal to measure the topological magnetoelectric effect was postulated by Qi *et al.* in 2009 [24], where they argued that placing an electric point charge above the surface of a (magnetic) topological insulator would generate a magnetic field that looks like it originates from a magnetic point charge, i.e. the ‘magnetic monopole’. In their analysis, they make use of the method of image charges to calculate resulting electric and magnetic fields. Here, we work from the framework of axion electrodynamics that we established in Sec. 2.2 and consider a more realistic measurement setup. We compare our findings with the ones proposed originally and also discuss some limitations for the observation.

We consider the geometry of Fig. 2.1. The device is a top gated structure. The observation of the TME is said to require broken time-reversal symmetry [24, 30] and as such, the original proposal uses a magnetically doped topological insulator. Here, we choose to use V-doped $(\mathrm{Bi}_{1-x}\mathrm{Sb}_x)_2\mathrm{Te}_3$ (see Chapter 4). The top gate electrode is separated by a dielectric layer. We now consider the case where we apply a finite potential V to the gate electrode (with respect to the surface of the TI). The potential will generate an

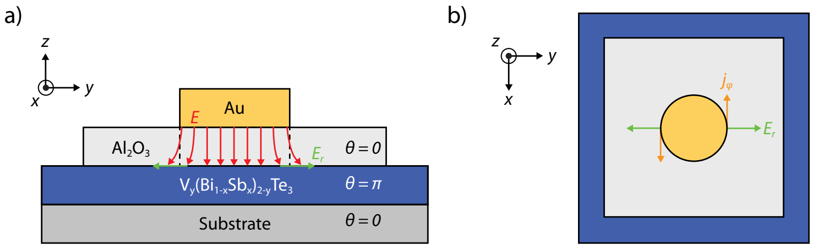

Figure 2.1: Schematic overview of an experiment setup to measure the TME by placing a charge (reservoir) above a MTI film. **(a)** Side view of the experiment. A top gated device is fabricated. Upon charging the top gate (i.e. apply $|V| > 0$) charge is generated at the gate dielectric. The resulting electric field (red arrows) is perpendicular to the surface of the TI everywhere except near the edges of the gate, where an in-plane component (green arrows) is present. **(b)** Top view of the experimental setup. The in-plane electric field (green) gives rise to a current perpendicular to the field (orange).

electric field **E** which is indicated in Fig. 2.1(a) as the red lines. We start from Eqn. 2.17, which, for a static applied electric field, reduces to[3]

$$\boldsymbol{\nabla} \times \mathbf{B} = \frac{\kappa}{\mu_0 c}\left[(\boldsymbol{\nabla}\theta) \times \mathbf{E} + \theta(\boldsymbol{\nabla} \times \mathbf{E})\right]. \tag{2.21}$$

The electric field of our top gate has no rotation and as such we are left with a gradient in θ,

$$\boldsymbol{\nabla} \times \mathbf{B} = \frac{\kappa}{\mu_0 c}(\boldsymbol{\nabla}\theta) \times \mathbf{E}. \tag{2.22}$$

We assume that the electric field is screened throughout the bulk of the TI and hence its effects on the bottom surface will be of less importance. We then focus only at the top surface of the TI. At the interface, θ changes abruptly from π to 0. Hence, we could use a Heaviside function $H(z)$ to describe the axion angle as $\theta = \pi H(-z)$. The derivative of the Heaviside function is a delta function, and hence the gradient in Eqn. 2.22 results in

$$\nabla\theta = -\pi\delta(z)\hat{\mathbf{z}}. \tag{2.23}$$

We thus find that the rotation of the induced magnetic field becomes

$$\boldsymbol{\nabla} \times \mathbf{B} = -\mu_0 \frac{e^2}{2h}\delta(z)\hat{\mathbf{z}} \times \mathbf{E}. \tag{2.24}$$

---

[3] We expand $\nabla \times \theta\mathbf{E}$, since both θ and $\mathbf{E}$ depend on position.

Because the gradient of θ is only non-zero in the z-direction, it implies that only in-plane electric fields will generate a response at the surface of a TI. Fig. 2.1(a) schematically shows the electric field lines (red lines) when a voltage is applied to the top gate. While the electric field lines for the bulk of the gate are fully perpendicular to the interface of the TI, the field lines near the edges of the gate do have an in plane component (green lines) pointing outwards. Because of the radial symmetry of the gate (see the top view in Fig. 2.1(b) as well) we denote this in-plane field as E_r. The cross product in Eqn. 2.24 ensures that the induced surface current[4] (i.e. the r.h.s. of the equation) is perpendicular to both E_r and $\nabla\theta$, and as such the surface current flows along the edges of the top gate, as indicated in Fig. 2.1(b) by the circulating current j_φ. Furthermore, Eqn. 2.24 shows that the current is proportional to a quantized Hall conductance of $\sigma_{\text{xy}} = (1/2) \cdot (e^2/h)$. Because of the quantized Hall conductance, an applied electric field leads to a quantized Hall current on the surface of the TI, which then leads to a magnetic polarization.

In the proposal by Qi *et al.* [24] the magnetic response of the device can be either detected by a magnetic force microscope (MFM) or by a SQUID. In MFM measurements a tip, carrying a magnetic flux and an electric charge q_e, scans over the surface of the TI. If a charged impurity is located on the surface of the TI, the MFM tip can sense the magnetic response of the impurity by scanning both tip voltage and position. While the electric charge of the tip can influence the measurement, the monopole contribution decays over $1/r^3$ while the charge interactions decay over $1/r^6$, so that the monopole contribution dominates over larger ranges [24]. The MFM setup restricts one to scan impurities over the surface, which are not controllable. As such, the strength of the TME can not be varied. Furthermore, (magnetic) domains also influence the MFM measurements and isolating the true response of the impurity can thus be a difficult task. The experimental setup involving a SQUID makes use of a macroscopic manifestation of the TME. In the original proposal, a top gate is surrounded by a SQUID which is patterned on the TI film as well. Here, we propose to place a separate SQUID sensor close to (i.e. above) the device. Applying a voltage to the top gate induces charges on the surface of the TI[5], which induce magnetic charges

---

[4] Ampère's law, which tells us that the rotation of the magnetic field is a current, still holds.

[5] If we consider that our top gate is a parallel plate capacitor, the induced carrier density can be calculated via $\Delta n_s = (\epsilon_0\epsilon_r)/(ed) \cdot V_{\text{TG}}$, provided that ϵ_r is constant regardless of temperature and applied gate voltage.

according to [24]

$$q_m = \frac{2\alpha}{(\epsilon_1 + \epsilon_2)(\mu_1^{-1} + \mu_2^{-1}) + \alpha^2} \frac{1}{\sqrt{\epsilon_0 \mu_0}} q_e, \tag{2.25}$$

where q_m is the magnetic charge (units A·m), $\epsilon_{1,2}$ are the dielectric constants of vacuum and the TI respectively, and $\mu_{1,2}$ are their permeabilities, and q_e is the applied electric charge. If we consider a small gate of $r = 1$ μm and a modest carrier density of $5 \cdot 10^{11}$ cm^{-2}, we can induce a charge of $q_e = 2.5 \cdot 10^{-15}$ C. Provided that a typical SQUID sensor is at a distance $d \gg r$, the gate can still be seen as a 'monopole' and we could convert the electric charge into magnetic charge according to Eqn. 2.25. We choose $\mu_1 = \mu_2 = 1$. The volume directly in between the gate electrode (i.e. the electric charge) and the TI is the dielectric (typically Al_2O_3) and as such we consider $\epsilon_1 = 9$. For a typical TI we consider $\epsilon_2 = 30$ [36, 37]. The induced magnetic charge is then $q_m = 1.402 \cdot 10^{-10}$ A/m. Similar to the electric field of a point charge, $\mathbf{E} = \frac{1}{4\pi\epsilon_0}\frac{q_e}{r^2}\hat{\mathbf{r}}$ we could construct the field of a magnetic monopole $\mathbf{B} = \frac{\mu_0}{4\pi}\frac{q_m}{r^2}\hat{\mathbf{r}}$. The flux passing the SQUID can be computed by $\Phi = \int \mathbf{B} \cdot \mathrm{d}\mathbf{a}$ and is found to be

$$\Phi = \frac{\mu_0 q_m}{2} \left[1 - \frac{d}{\sqrt{d^2 + R_{\mathrm{SQUID}}^2}} \right], \tag{2.26}$$

where R_{SQUID} is the (effective) radius of the SQUID. For a SQUID with an effective area of 10 μm^2 [38] at a distance of $d = 65$ μm (Sec. 6.3) we find $\Phi = 5 \cdot 10^{-4}$ Φ_0, which is small, but observable.

While the original proposal introduces the concept of an image magnetic monopole, the divergence of the magnetic field is still zero, as Gauss's law for magnetism is not changed by axion electrodynamics (see Eqn. 2.16). The absence of a 'true' monopole (i.e. $\boldsymbol{\nabla} \cdot \mathbf{B} \neq 0$) was furthermore confirmed in Ref. [39] where the magnetic field was calculated explicitly and was found to resemble a Pearl vortex. The magnetic field calculated in Eqn. 2.24 reduces to such vortex field when the size of the gate becomes comparable to a point charge. For a gate of finite size, such as in realistic experiments, the field rather looks like the field of an extremely thin solenoid. Such magnetic field can be detected by an extremely sensitive magnetometer, such as a superconducting quantum interference device (SQUID). The experimental attempt to realize the proposed experiment will be discussed in Chapter. 6.

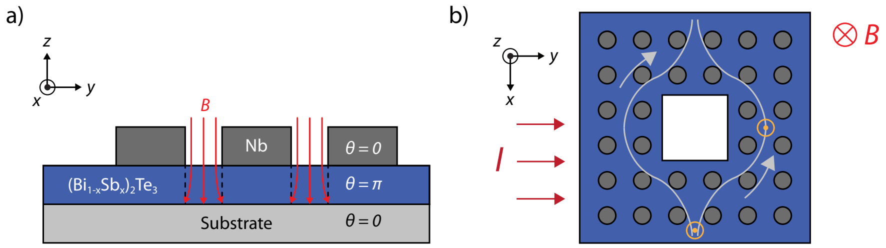

Figure 2.2: Schematic overview of the experimental setup. **(a)** Side view of the experiment. Nb islands are deposited on top of the BST film. When a magnetic field is applied perpendicular to the interface of the TI, flux lines penetrate the interface (red lines). **(b)** Josephson junction array (JJA) where an applied current comes in from the left. Josephson vortices (orange circles) move perpendicular to the applied current and interfere around the hole.

2.4 Measuring the Witten effect through Josephson junction arrays

Another proposal to measure the topological magnetoelectric effect was postulated by Nogueira *et al.* [40]. Here, they argue, based on earlier calculations in Ref. [41], that the interface between a topological insulator and a type-II superconductor (SC) can host the TME as well.

Type-II superconductors exhibit Abrikosov vortices, which are small regions where the superconductor is in the normal state and through which the externally applied magnetic field can penetrate the superconductor. Abrikosov vortices contain a quantized amount of flux, called the magnetic flux quantum $\Phi_0 = h/2e$. When a type-II superconductor is in contact with a TI, the vortex pierces the interface. The TI again has $\theta = \pi$ and the (normal metal) superconductor has $\theta = 0$. Hence, the electromagnetic response at the SC-TI interface is governed by axion electrodynamics. It was suggested in Refs. [40, 41] that this response can be studied in a Josephson junction array (JJA), i.e. an array of superconducting islands which forms a network of Josephson junctions. Below, we will first introduce the electromagnetic response at the interface and then discuss the experimental setup in more detail.

We consider the geometry of Fig. 2.2. The superconductor (dark gray) is patterned in small islands on top of the topological insulator film (blue). We apply a magnetic field perpendicular to the film. The magnetic field penetrates the film in between the array of superconducting islands. If the phase difference of the superconducting order parameter across a closed loop of Josephson junctions in the array is 2π, a Josephson vortex (yellow circles in Fig. 2.2(b)) is formed in between the four islands. If the critical current, I_c, of the Josephson junctions is large enough, Josephson vortices have a flux equal to a single magnetic flux quantum. The hole in the array (visible in the middle of Fig. 2.2(b)) will be used for the interference experiment as will be discussed below.

We now derive the consequences of axion electrodynamics at the SC-TI interface as was first introduced in Refs. [40, 41]. In a trivial material, the electric charge can be computed with Gauss's law,

$$\frac{1}{\epsilon_0}Q = \oint \mathbf{E}\cdot \mathrm{d}\mathbf{a} = \int (\boldsymbol{\nabla}\cdot\mathbf{E})\,\mathrm{d}\mathbf{r}, \tag{2.27}$$

where d**a** and d**r** are area and volume elements, respectively. For the interface between a SC and TI, we have to use the Eqn. 2.19, so that

$$\frac{1}{\epsilon_0}Q = \int \mathrm{d}\mathbf{r}\left(\frac{\rho}{\epsilon_0} - \kappa c\left[\boldsymbol{\nabla}\theta\cdot\mathbf{B} + \theta(\boldsymbol{\nabla}\cdot\mathbf{B})\right]\right). \tag{2.28}$$

The first term of the r.h.s. corresponds to any present charge density in the system. In the absence of any topological system, the latter two terms vanish and the integral over the charge density results in a charge, as one expects from Gauss's law. The latter two terms in the r.h.s. are due to axion electrodynamics.

In 1979, Witten showed within the framework of high energy physics that if magnetic monopoles exist, they can bind a fractional charge to them [42]. We consider a uniform but non-zero θ and hence focus on the last term of Eqn. 2.28,

$$\frac{1}{\epsilon_0}Q = \frac{q}{\epsilon_0} - \int \mathrm{d}\mathbf{r}\,\kappa c\theta(\boldsymbol{\nabla}\cdot\mathbf{B}). \tag{2.29}$$

The magnetic flux of a monopole is[6] $\Phi_B = h/e$, and thus for a monopole

---

[6] The flux of a monopole is twice the magnetic flux quantum that we defined earlier, since the latter is usually associated with superconductors which have Cooper pairs with charge $2e$.

we get

$$\begin{aligned}\frac{1}{\epsilon_0}Q &= \frac{q}{\epsilon_0} - \kappa c\theta\Phi_B \\ &= \frac{q}{\epsilon_0} - \frac{1}{\pi}\frac{1}{4\pi\epsilon_0}\frac{e^2}{\hbar c}c\theta\frac{h}{e} \\ &= \frac{q}{\epsilon_0} - \frac{\theta e}{2\pi\epsilon_0}. \end{aligned} \tag{2.30}$$

Since the charge $q = ne$, we arrive at

$$Q = e\left(n - \frac{\theta}{2\pi}\right). \tag{2.31}$$

If no external charges are present, i.e. $n = 0$, every magnetic monopole will bind a fractional charge $Q = e\theta/2\pi$ to it. This is called the Witten effect.

In reality, magnetic monopoles are absent and furthermore $\boldsymbol{\nabla}\cdot\mathbf{B} = 0$ remains unchanged within axion electrodynamics. However, at our SC-TI interface we do have a gradient in θ (similar to the case of Sec. 2.3). Hence, we focus on the second term in the r.h.s. of Eqn. 2.28,

$$\frac{1}{\epsilon_0}Q = \int \mathrm{d}\mathbf{r} - \kappa c\boldsymbol{\nabla}\theta\cdot\mathbf{B}. \tag{2.32}$$

We now apply a uniform magnetic field perpendicular to the SC-TI interface. Vortices arise within the JJA[7]. Since the magnetic field is perpendicular to the sample, the resulting field of the vortices only depends on the radial coordinate at the interface. Furthermore, the gradient in θ only exists in the z-direction, so we can invoke Eqn. 2.23 again. We now obtain

$$\begin{aligned}\frac{1}{\epsilon_0}Q &= \frac{q}{\epsilon_0} - \int \mathrm{d}\tau\, \kappa c\theta(\boldsymbol{\nabla}\theta\cdot\mathbf{B}) \\ &= \frac{q}{\epsilon_0} - \kappa c\int_{-\infty}^{0}\mathrm{d}z\,\frac{\partial\theta}{\partial z}\int \mathrm{d}^2r\, B(r) \\ &= \frac{q}{\epsilon_0} - \kappa c\pi\int \mathrm{d}^2r\, B(r). \end{aligned} \tag{2.33}$$

---

[7] These are the Josephson vortices. If a slab of a type-II superconductor is considered, Abrikosov vortices arise within the superconductor itself.

The integral over the interface now encloses a number of vortices, N_v. The magnetic flux of a vortex equals Φ_0, so that

$$\begin{aligned} \frac{1}{\epsilon_0}Q &= \frac{q}{\epsilon_0} - \kappa c \pi N_v \Phi_0 \\ &= \frac{q}{\epsilon_0} - \frac{1}{\pi}\frac{1}{4\pi\epsilon_0}\frac{e^2}{\hbar c} c \pi N_v \frac{h}{2e}. \end{aligned} \tag{2.34}$$

If we consider no external charges and consider a single vortex, we get

$$Q = -e/4. \tag{2.35}$$

As such, every vortex will bind a fractional charge to it.

The fractional charge at a topological insulator surface is proposed to be measured by an interference experiment in a JJA [40]. We have shown above that each Josephson vortex at the TI surface in a JJA will bind a charge proportional to the flux. In the case of n vortices, and thus n flux quanta at the interface of a TI and a trivial insulator, the Josephson vortices have a charge of $Q = n\frac{e}{4}$ at the interface. The vortices in Josephson junction arrays are spatial arrangements of the phase of the superconducting order parameter, which move through the array in response to forces generated. For example, Josephson vortices, once unpinned, move perpendicularly to the external current [43, 44]. We can make use of an Aharonov-Bohm (AB) type of interference experiment to observe the fractional charges. The effect results in charged particles acquiring a phase, $\Delta\phi = \frac{q}{\hbar} B \cdot S$, when moving around an external magnetic field. Here B is the external magnetic field and S is the area where the magnetic field is present. If there is a ring-like geometry (as illustrated in Fig. 2.2(b)), the phase picked up by the moving Josephson vortices leads to oscillation of the $I_c(B)$ of the JJA. The period of this oscillation depends on the geometry of the JJA and the size of the hole. In addition to the conventional charge (in form of Cooper pairs), if the fractional charges are present in a JJA, the phase picked up by the $e/4$ charge is 4 times smaller, resulting in a 8π-periodic oscillation. It is this configuration that was proposed by Nogueira *et al.* [40] to detect the fractional charge formed due to the axion dynamics.

The experimental attempt to realize this proposal will be discussed in Chapter 7.

2.5 The chiral magnetic effect

In the previous sections we have addressed two of the three occurrences of θ in the equations governing axion electrodynamics, Eqn. 2.16. In this section, we will address the last option, which is a temporal derivative of θ. For this specific experiment, we consider Dirac or Weyl semimetals. In contrast to topological insulators, which have a linear dispersion relation for the surface states (i.e. a 2D linear dispersion relation for a 3D TI), a Dirac semimetal has a linear dispersion relation in all three directions. As such, the Dirac states become bulk states. A Weyl semimetal is a Dirac semimetal in which the Dirac cones have been separated in momentum space [45].

The starting point for the chiral magnetic effect is Eqn. 2.17,

$$\boldsymbol{\nabla} \times \mathbf{B} = \mu_0 \left[\mathbf{j} + \epsilon_0 \frac{\partial \mathbf{E}}{\partial t} + \frac{\kappa}{\mu_0 c} \left(\boldsymbol{\nabla} \times \theta \mathbf{E} + \frac{\partial}{\partial t} \theta \mathbf{B} \right) \right]. \tag{2.36}$$

We consider the case where θ is spatially uniform but can vary in time. In addition, we apply a static magnetic field with no rotation, and we apply no external magnetic field. We are left with

$$\mathbf{j} = -\frac{e^2}{4\pi^2 \hbar} \dot{\theta} \mathbf{B}. \tag{2.37}$$

Hence, a current is induced which is parallel to the applied magnetic field, and its strength depends on the time derivative of θ.

To investigate the nature of $\dot{\theta}$, we return to the Weyl semimetals. Weyl semimetals have a low-energy effective Hamiltonian [12],

$$H = \chi \hbar v_F \mathbf{k}, \tag{2.38}$$

where $\chi = \pm 1$ is the chirality. The sum of chiralities of the Weyl nodes needs to be zero, and as such the simplest Weyl system contains two Weyl nodes with opposite chirality. In Eqn. 2.37 we have shown that a static magnetic field alone would be enough to generate a current. In reality, a non-equilibrium situation needs to be created in order for the effect to manifest itself [46, 47].

We can create such non-equilibrium conditions by applying an external electric field to the Weyl semimetal as well, parallel to the applied magnetic field. Here, we follow the derivation by Nielsen and Ninomiya [48]. The energy levels of the Weyl semimetal are given by the Landau levels, as shown

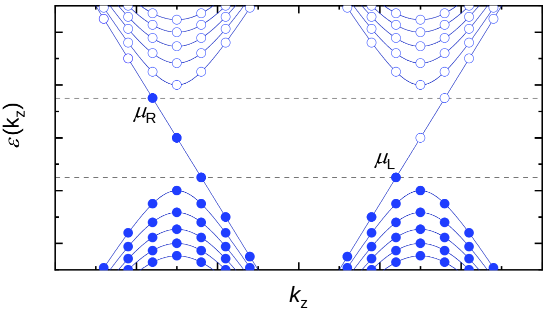

Figure 2.3: Landau levels for the Weyl fermions. The dots correspond to empty (white) and filled states. The zeroth Landau level is linear. Because of the applied parallel electric and magnetic fields, a difference between the chemical potentials μ_R and μ_L arises, leading to the chiral chemical potential $\mu_5 = (\mu_R - \mu_L)/2$.

in Fig. 2.3, for which the zeroth level disperses linearly, in contrast to the other levels. When the electric and magnetic fields are applied in the same direction, all states will move according to $\hbar d\mathbf{k}/dt = -e\mathbf{E}$. We focus on the zeroth Landau levels which have $\varepsilon = \chi v_F \hbar k_z$ where ε is the energy and we consider $\mathbf{B} = B_z$. Upon combining these equations we obtain

$$\frac{d\varepsilon}{dt} = -\chi e v_F E_z. \tag{2.39}$$

The linearity of the zeroth Landau level means that the motion of the Weyl fermions correspond to Weyl fermions disappearing from the right-moving states (denoted by chemical potential μ_R) and Weyl fermions appearing in the left-moving states (μ_L). The creation and annihilation rates of the Weyl fermions are determined by the chemical potentials $\mu_{R,L}$. The density of states for the right-moving states are [35]

$$\frac{dN_R}{dz} = \frac{1}{2\pi}\frac{dk}{dt}, \qquad \frac{d^2N_R}{dxdy} = \frac{eB}{2\pi\hbar}, \tag{2.40}$$

and for the left-moving states, one obtains $dN_L/dt = -dN_R/dt$. By combining Eqns. 2.39 and 2.40 we obtain the charge pumping rate of the chiral charge, N_C,

$$\frac{d^4N_C}{dtd^3x} = \frac{d^4N_R}{dtd^3x} - \frac{d^4N_L}{dtd^3x} = \frac{e^2}{2\pi^2\hbar}E_zB_z. \tag{2.41}$$

This chiral charge pumping is also known as the Adler-Bell-Jackiw or chiral anomaly [49, 50]. The system equilibrates at a chiral chemical potential [51],

$$\mu_5 = \frac{\mu_R - \mu_L}{2}, \tag{2.42}$$

which, even though the Weyl fermions can relax, remains non-zero, and hence leads to the non-equilibrium conditions required to observe the induced current of Eqn. 2.37. The role of the axion angle θ is recognized as $\dot{\theta} = \mu_5$ [35]. The energy required to generate the chiral chemical potential is taken from the electric field by an additional current, and it is the additional current of Eqn. 2.37, leading to a negative magnetoresistance, that is known as the chiral magnetic effect,

$$\mathbf{j}_{\mathrm{CME}} = -\frac{e^2}{4\pi^2\hbar}\mu_5\mathbf{B}. \tag{2.43}$$

Later, the chiral magnetic effect was also derived in a semi-classical approach which does not require the presence of Landau levels [52]. Still, a non-zero chiral chemical potential is generated and the presence of parallel electric and magnetic fields lead to an extra induced chiral current.

The chiral magnetic effect may be the least ‘direct’ manifestation of axion electrodynamics as the role of the axion angle is buried deeply within quantum electrodynamics. Nevertheless, its implications through the extra current that is induced when parallel electric and magnetic fields are generated can be observed in Dirac or Weyl semimetals. We will show experimental evidence for the observation of the chiral magnetic effect in Chapter 5.

2.6 Discussion

So far we have shown the implications of axion electrodynamics and have introduced three different experiments to probe the consequences of the topological magnetoelectric effect. While the chiral magnetic effect has been observed in different materials (Chapter 5 and Refs. [51, 53–55]), experiments in search of the more direct probes for the axion electrodynamics, i.e. the physics related to the spatial derivative of θ, have not shown definitive results yet. Moreover, different theoretical predictions do not fully agree on requirements for the observation of the TME. In this section, we discuss some concerns and performed experiments within the field.

The axion angle θ is generally considered to be $\pi(\mathrm{mod}\,2\pi)$ within a topological insulator as time reversal symmetry needs to be preserved [10, 12, 28, 30, 56]. For magnetic topological insulators, differences in the value of θ arise. While the value is considered to be quantized in Ref. [28], other calculations show that the value can be arbitrary for MTIs, where its value would depend on the magnetization [12]. A continuous spectrum for θ can lower the strength of the TME significantly. We note that a non-quantized, non-topological magnetoelectric response was already reported for Cr_2O_3 [57] and in multiferroic materials [58].

The theoretical proposals of the magnetic monopoles and the fractional charges are based on situations where only a single surface of the TI is considered. In realistic experimental setups, typically film thicknesses of 5-10 nm are used, and as such the two surfaces are close to each other. It is thus of importance that TME effects arising from one surface are not counteracted by the other surface. The gradient of θ that we defined in Eqn. 2.23 may either point in the same direction for both surfaces, or may point in opposite directions. For a homogeneous system, such as a quantum anomalous Hall (QAH) insulator[8], the magnetization of both surfaces points in the same direction. As such, the gradient in θ also points in the same direction when considered along the z-axis of the material [28]. However, Eqn. 2.23 considers the surface normal, which is opposite for both surfaces and hence the sign in the gradient of θ is opposite for both surfaces as well. Thus, both surfaces would produce an opposite response which, if both surfaces produce effects of the exact same size, would cancel. In an experimental setup however, the influence of the gate (Sec. 2.3) or magnetic field (Sec. 2.4) can be different at the surface located the farthest from the applied source and hence cancellation will no longer be perfect.

A more promising material would have an opposite magnetization at both surfaces, and as such produce a non-canceling TME response. For such material, the gradient of θ along the z-axis is opposite for both surfaces and hence is parallel when considering the surface normal. While its theoretical prediction came together with the original work on the TME [10], the experimental realization of the so-called axion insulator only took place a few years after the discovery of the QAH state [59, 60]. The axion insulator is realized by creating a heterostructure of MTI and TI layers. Here, in

---

[8] We will introduce the quantum anomalous Hall effect in detail in Chapter 4.

general, two layers of a MTI are separated by a normal layer of BST. While the MTI layers can be of the same kind (twice Cr-doped BST [59] or twice V-doped BST [61]), they can also be two different layers, i.e. one layer of Cr-doped BST and one layer of V-doped BST [60, 61]. For large external magnetic fields, both layers are still parallel to each other and $\sigma_{\mathrm{xy}} = \pm e^2/h$, similar to the QAH state. However, for an intermediate (non-zero) field strength, the magnetization of both layers can be anti-parallel, and hence both σ_{xx} and σ_{xy} are zero. This is the then called the axion insulator state, which would be the perfect situation for the observation of the TME. More recently, such axion insulator state was also observed in the septuple-layer (SL) material $\mathrm{MnBi_2Te_4}$, which has an antiferromagnetic ordering between successive SLs [62].

While the axion insulator state was established in a variety of materials, the existence of a regime where $\sigma_{\mathrm{xx}} = \sigma_{\mathrm{xy}} = 0$ does not directly prove the existence of axion electrodynamics. In fact, recently it was proposed by Fijalkowski *et al.* [31] that the axion insulators as described above will not show any sign of the TME, as they are effective 2D systems, while the axion Lagrangian of Eqn. 2.10 is only present for 3D topological insulators. Furthermore, in Chapter 4 we show that the regime where $\sigma_{\mathrm{xx}} = \sigma_{\mathrm{xy}} = 0$ can also be observed in a QAH system upon reversal of the magnetization. As such, there is a random order of the domains. Fijalkowski *et al.* [31, 63] argue that no proof exists that the 'axion insulator' phase actually has a magnetization pointing outwards for both surfaces, as this is difficult to measure experimentally. Hence, the heterostructures of a MTI-TI-MTI stack would not show axion-related physics. They then argue that the quantum anomalous Hall (QAH) state is the state in which one can observe the TME. This deviates from the original proposal of Qi *et al.* [10] where the axion insulator state was argued to be the hallmark state. Thus, at present the exact relation between the quantum anomalous Hall state, the axion insulator and the topological magnetoelectric effect remains unclear.

In addition to the recent experiments on V-doped BST samples [31], there has been a class of different experiments to measure the TME. Instead of electronic transport, the thin film is irradiated by polarized THz electromagnetic waves. The modifications in Maxwell's equations lead to a rotation of the polarization, which can be detected either in the transmitted wave (Faraday rotation) or in the reflected wave (Kerr rotation) [10, 12, 28]. In the quantized limit, the Faraday angle is $\theta_F = \tan^{-1}(\alpha)$ and thus takes a fundamentally quantized value. The experiment has been performed on films of the 3D TI Bi_2Se_3 under applied magnetic field to break time-reversal symmetry [64], and in Cr-doped BST which are close to the QAH state [65]. Both experiments show trends towards quantization of the Faraday and Kerr rotation angles and thus are regarded as evidence for axion electrodynamics. However, in a commentary letter Beenakker [66] pointed out that both Cr-doped BST and Bi_2Se_3 under magnetic field lead to the quantum Faraday effect, which occurs only when the Hall conductivity at both surfaces is the same, such as for the QAH system, for which we discussed above that the TME might be canceled. In addition, when the system would be an axion insulator, both surfaces would generate an opposite Faraday rotation and hence there is no net rotation. Despite the commentary letter, later it was discussed that although the quantum Faraday effect can indeed be used to describe the optical measurements, they can also be explained in terms of axion electrodynamics [67], leaving a conclusion on the presence or absence of axion electrodynamics elusive for now.

The different points that were mentioned above show that some of the theoretical concepts are still under debate. Experimental results might therefore contribute by providing understandable evidence, such as experimental proof of presence or absence of the TME in specific materials, and help both the theoretical and experimental community in further experiments within the field.

2.7 Conclusion

We have discussed the framework of axion electrodynamics and reviewed the modifications to Maxwell's equations. For systems in which the axion angle changes with respect to position, such as at the interface of a TI and a normal material or superconductor, we show that additional magnetic and electric responses arise. We propose to measure the magnetic response of an electric charge by means of a top gated magnetic topological insulator and a SQUID sensor, and we propose to measure the fractional charge by means of interference in a Josephson junction array. We furthermore discussed the analogy between the temporal derivative of the axion field and the chiral chemical potential, for which the application of parallel electric and magnetic fields in Weyl semimetals leads to the chiral magnetic effect.

We have also discussed the recent advances and open questions which are still to be answered with more theoretical and experimental studies. While the general understanding within the field of research is evolving, new experiments bring radical changes in interpretation and show that the field of axion electrodynamics is far from fully understood. The direct experiments proposed in this chapter may contribute to the the question whether axion electrodynamics is present in topological systems to resolve the discrepancies in current experimental and theoretical studies.

Chapter 3

Deposition and electronic characterization of topological insulators thin films

The experiments throughout this thesis are performed on devices which are fabricated on thin films of topological insulators. In this chapter, we discuss the deposition of thin films of $(Bi_{1-x}Sb_x)_2Te_3$ *by molecular beam epitaxy. We establish a fabrication process that enables us to create a variety of devices to study the electronic properties of the thin films. We then conduct a series of such electronic transport measurements to investigate the properties of the grown thin films. The fabrication processes, along with the material properties of* $(Bi_{1-x}Sb_x)_2Te_3$ *form the basis for materials and devices that are presented in the remainder of this thesis.*

3.1 Introduction

The study of topological insulators (TIs) started on single crystals of the material $Bi_{1-x}Sb_x$ [68] and binary materials such as Bi_2Te_3 [69], where angle-resolved photoemission spectroscopy (ARPES) measurements were performed to confirm the topological surfaces states (TSS) and transport measurements on bulk crystals were performed. While even advanced experiments can be performed on devices which were fabricated on exfoliated flakes of such bulk crystals (an example is the study presented in Chapter 5), variations in flake thickness and size make systematic studies difficult. Furthermore, single crystals suffer from large bulk conduction channels due to Te vacancies, so that the TSS remain hidden in electronic transport measurements.

Thin film deposition of TIs has led to materials which exhibit less bulk carriers as the film thickness is reduced drastically. In addition, deposition techniques such as molecular beam epitaxy (MBE) lower the amount of Te vacancies by applying a surplus of Te atoms during the film growth, which furthermore reduces the amount of bulk carriers.

In this chapter, we discuss the process of MBE deposition by considering the ternary TI $(Bi_{1-x}Sb_x)_2Te_3$ (BST). We also consider the fabrication process for typical devices such as Hall bars, with and without gates. We conclude the chapter with a basic characterization of the BST films by means of transport measurements. The BST films also appear in Chapter 7, where Josephson junctions are fabricated on the MBE grown films. Furthermore, BST serves as a basis for magnetically doped topological insulators (MTIs), where a magnetic dopant is introduced to the system. We will discuss the growth and devices of MTI films later in Chapters 4 and 6, respectively.

3.2 Ternary topological insulators

Telluride materials with the crystal structure X_2Te_3, such as Bi_2Te_3 and $(Bi_{1-x}Sb_x)_2Te_3$, all crystallize in the same rhombohedral crystal structure and belong to the $R\bar{3}m$ space group with five atoms in a unit cell. The crystal structure is shown in Fig. 3.1(a). Here, the red atoms correspond to Te, and the blue atoms can either be Bi (resulting in Bi_2Te_3), Sb (Sb_2Te_3) or both ($(Bi_{1-x}Sb_x)_2Te_3$). In the latter case, the Bi and Sb atoms distribute themselves randomly across the Bi/Sb lattice sites. Atoms are bonded covalently within five layers of atoms, counted in the c-direction, called quintuple layers (QLs). The QLs are bonded by weaker van der Waals bonds. These

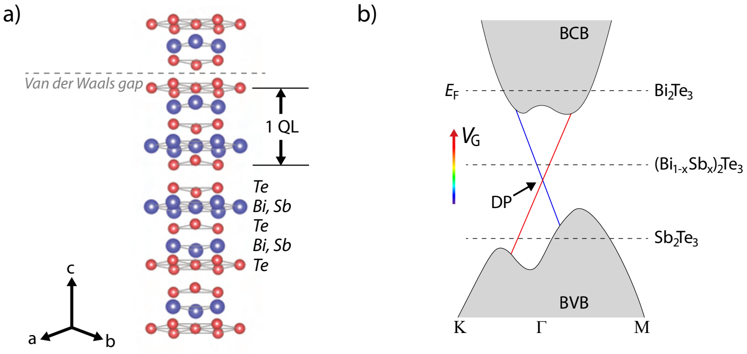

Figure 3.1: Properties of ternary topological insulators. **(a)** The crystal structure of $(Bi_{1-x}Sb_x)_2Te_3$. The red spheres correspond to Te atoms. The blue spheres represent the Bi and Sb atoms, which share the same lattice sites and are randomly distributed in ternary compounds. Five atomic layers are covalently bonded (bonds not shown for clarity) while in between these layer stacks weaker van der Waals bonds are present. The five atomic layers, being a stack of Te-Bi/Sb-Te-Bi/Sb-Te, are also called quintuple layers (QL) and are about 1 nm in height. The height of the entire unit cell is about $c = 30.5$ Å and $a = b = 4.30$ Å. **(b)** Evolution of the electronic band structure of $(Bi_{1-x}Sb_x)_2Te_3$ upon changing the Bi:Sb ratio or by gate tuning. For Bi_2Te_3, the Fermi level resides in the BCB, while for Sb_2Te_3 it resides in the BVB. By changing the composition the compound the Fermi level can be tuned to the DP.

weak forces between layers lead to a layered growth mechanism, which is called van der Waals epitaxy [70]. Van der Waals systems have been studied extensively in the past, and gained major interest after the Nobel prize of 2010 was awarded to Novoselov and Geim for their work in 2004 on mechanical exfoliation of highly oriented pyrolytic graphite (HOPG) to graphene, an atomically thin sheet of carbon atoms [71]. Here, the relatively weak van der Waals forces between layers of graphite are broken due to the strength of the exfoliation process, enabling one to obtain extremely thin layers of the material[1].

We now turn to the band structure of the materials at hand, see Fig. 3.1(b). While the binary telluride TIs (Bi_2Te_3, Sb_2Te_3) exhibit topological surface states, their high bulk conductivity hampers the detection of topological signals in transport measurements, since for example the Fermi level of Bi_2Te_3

---

[1] Note that it is the same principle of mechanical exfoliation that also serves the basis of the devices presented in Chapter 5 and Sec. 7.2.

lies in the bulk conduction band (BCB) due to the Te vacancies and Te-Bi antisite defects [72, 73]. Furthermore, the Dirac point (DP) is located within the bulk valence band (BVB). In contrast to the *n*-type behavior of Bi_2Sb_3, Te vacancies and Te-Sb antisites make the Fermi level of Sb_2Te_3 reside in the BVB, while its DP lies within the band gap. By alloying the two materials the properties can be tuned over a wide range. Upon increasing the Sb content in $(Bi_{1-x}Sb_x)_2Te_3$, the DP shifts upwards in energy from the BVB. Simultaneously, the Fermi level shifts downwards. The extensive and systematic studies in Refs. [72, 73] have shown the TSS in ARPES measurements and have shown the crossover from *n*-type transport to *p*-type transport. An alternative route to tuning the material's properties closer towards the DP is by means of gate tuning, in which the Fermi level changes due to the applied electric field over a suitable dielectric layer. By first tuning the Bi:Sb ratio so that the Fermi level is close to the DP, the films can subsequently be gate tuned through the DP even for moderate gate voltages. Fig. 3.1(b) summarizes the discussion on the band structure into a single figure. The BVB and BCB are shown as gray areas, and the TSS are depicted as blue and red lines. The DP lies at the crossing of these TSS. The Fermi level is shown for three cases. The topmost case corresponds to either pure Bi_2Te_3, or to BST while being tuned by a positive gate voltage (with respect to the gate voltage required to be at the DP). The middle case corresponds to a BST film having an almost perfect ratio of Bi:Sb, so that the Fermi level is close to the DP. Lastly, the bottom case corresponds to pure Sb_2Te_3, or to BST while being tuned by a negative gate voltage. Note that while the location of the DP remains the same during gate tuning experiments, it does change upon changing the Bi:Sb ratio [72]. The excellent gate tunability of the ternary compound BST, along with its moderately insulating bulk, makes it a prototype material to study a great variety of topological effects.

3.3 Molecular Beam Epitaxy of BST thin films

The thin films presented in this thesis were grown in an Octoplus 300 MBE system of Dr. Eberl MBE Komponenten. A schematic overview of the system is shown in Fig. 3.2. The system is equipped with standard Knudsen cells for the evaporation of high-purity Bi (5N), Sb (5N) and Te (5N). For V (4N), the system also contains an e-beam evaporator and a custom high-temperature Knudsen cell[2]. A base pressure of about $5 \cdot 10^{-11}$ mbar

---

[2] We will incorporate vanadium into topological films in Chapter 4.

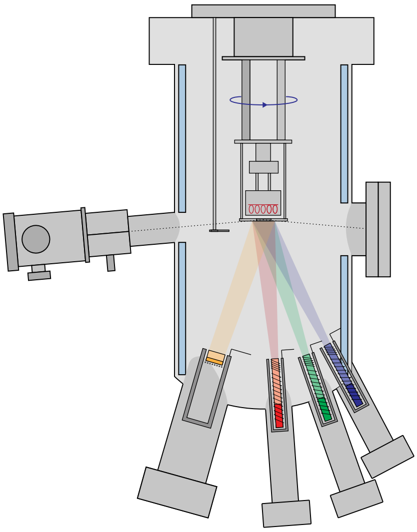

Figure 3.2: Schematic overview of the MBE system. The standard Knudsen cells have two sets of filaments surrounding the crucibles (red, green, blue). The bottom filament heats the material to the desired temperature, while the top filament is slightly warmer to prevent redeposition on the crucible walls. The custom high-temperature Knudsen cell has a cup-like crucible (yellow) which is heated from underneath. All sources are equipped with shutters. The substrate is loaded upside down into the bottom plate of the manipulator stage (dark gray rectangle). The sample plate is heated by irradiation from the tungsten filament (red spirals). The manipulator has its own shutter. The sample holder typically rotates at 3 RPM to guarantee homogeneous depositions. A RHEED gun (left side of the system) and phosphor screen (right side) allow for growth monitoring. A liquid nitrogen cooling shroud covers the interior of the growth chamber (light blue).

is realized by combining a turbomolecular pump, getter pump and a liquid nitrogen cooling shroud. The system is equipped with a quartz crystal monitor (QCM) to calibrate the fluxes of the individual sources, a residual gas analyzer (RGA) to monitor the composition of the background gas and equipment for reflection high-energy electron diffraction (RHEED) to monitor the growth process. Substrates are clamped onto flag-style Omicron holders, which are heated from the back by irradiation of a tungsten filament.

The MBE deposition process typically depends on various parameters, such as choice of substrate, the temperature of the substrate, the temperatures (fluxes) of the crucibles, and pre- and/or post-annealing steps. Extensive reviews discuss the influence of these parameters at length [74, 75]. We will first introduce the growth parameters and then discuss the growth on a set of different substrates. The particular substrates used in this chapter will be used for the experiments in the upcoming chapters as well, where the substrate of choice depends on the goal of the experiments. The temperature of the substrate plays an important role as it determines the kinetics of the adatoms. If the substrate temperature is too low, atoms will not have enough energy to migrate over the surface to find the energetically most favorable lattice site. If the temperature is too high, atoms cluster together and the film consists of 3D islands rather than a smooth, closed 2D layer. At even higher temperatures, the sticking coefficient of TI materials becomes so low that no films are formed. The temperatures of the Knudsen cells determine their evaporation rate, which is enhanced at higher temperatures. The QCM allows us to calibrate the fluxes of the different sources and hence ensure that the stoichiometry of films is reproducible over long periods of time. To reduce the number of Te vacancies, one typically applies a Te flux that is 10× larger than calculated for the desired stoichiometry. Since the substrate temperature during the film growth is higher than the sticking temperature of Te, the surplus of Te atoms will not stick to the substrate or film, unless there is a Bi/Sb atom to bind to. This property leads to a true layer-by-layer growth mechanism [76]. Because of this, the growth rate of the films depends on the fluxes of Bi and Sb, but not on the exact flux of Te. Typical growth rates for our films vary from 0.05 QL/min to 0.2 QL/min.

So far, binary and ternary TIs have been successfully grown on a great variety of substrates, including Al_2O_3 (0001) [77–79], Si (111) [73–75, 80], $SrTiO_3$ (111) [81, 82], InP (111)A [83, 84]. The van der Waals bonds between the different QLs relax the requirements that are usually present for standard epitaxial growth; the lattice mismatch between substrates and telluride TIs can be quite substantial. We have investigated the growth of BST on three substrates: Al_2O_3 (0001), $SrTiO_3$ (111) and Fe-doped InP (111)A. While the lattice mismatch between the TI and InP is the smallest, the other substrates are as interesting because of their own advantages: Al_2O_3 substrates are relatively cheap and hence useful for future applications, while $SrTiO_3$ has a huge dielectric constant at low temperatures [85], allowing one to gate tune the films by means of a back gate.

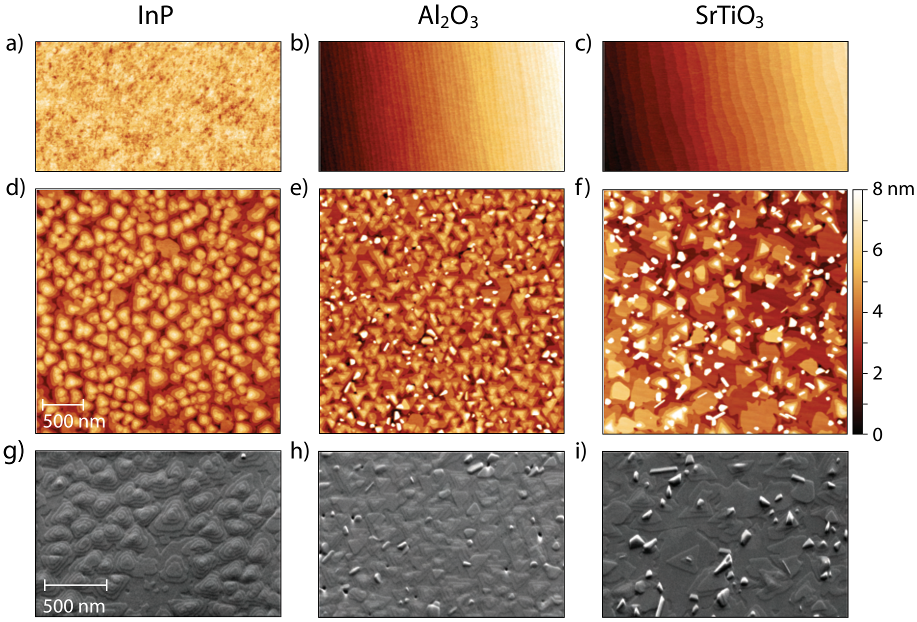

Figure 3.3: Morphology of BST thin films. All AFM images (panels a-f) have an identical lateral scale. The same holds for the SEM images (panels g-i). **(a)** Cleaned InP substrate. No clear structure is present. The RMS roughness of the scanned area is 180 pm. **(b)** Cleaned and annealed Al_2O_3 substrate. Atomically flat terraces are present. **(c)** Cleaned, BHF treated and annealed $SrTiO_3$ substrate. Wider terraces are present. **(d)** 10 nm BST film grown on InP. The film is smooth and shows rounded triangular domains. **(e)** 10 nm BST film grown on Al_2O_3. Triangular domains point in two directions, of which one is preferred strongly. Misoriented crystals are present as well. **(f)** 10 nm BST film grown on $SrTiO_3$. Occasional triangular domains are found, but no clear orientation is present. Misoriented crystals occur more often and more severely compared to Al_2O_3. **(g-i)** SEM images of the films shown in panels d-f, taken under an angle to improve visualization of the absence or presence of misaligned crystals.

Substrate preparation

The substrates are prepared by different treatments. First, we will discuss InP substrates. A layer of photoresist protects the diced substrates, and is removed by bathing the substrates in acetone in an ultrasonic cleaner. The substrates are then cleaned in an ethanol bath and blow-dried by a nitrogen gun. If the substrates show any particles, their surface is polished gently on a lens tissue while being soaked in ethanol. The applied force on the substrate should be kept minimal to prevent the substrates from breaking[3]. An atomic force microscope (AFM) image of a cleaned InP substrate is shown in Fig. 3.3(a). Its surface is relatively rough and shows no clear features. Al_2O_3 substrates are cleaned in acetone and ethanol as well, after which they follow the same lens tissue polishing. Afterwards, the samples are annealed in a tube furnace at 1030 °C for 1.5 hours without a supplied gas flow. The annealing step leads to atomically flat terraces on the surface of the substrate. An AFM image of a treated Al_2O_3 substrate is shown in Fig. 3.3(b). $SrTiO_3$ substrates undergo the same treatment as Al_2O_3 substrates, but have an additional step before the annealing. By immersing the substrates in water, the topmost SrO layer of the $SrTiO_3$ substrates is hydroxylated. This increases the etch-selectivity of the SrO with respect to the TiO_2 layers in a buffered HF solution [86]. After the BHF treatment, the substrates are polished on lens tissue again. The substrates are annealed in the tube furnace at 950 °C for 1.5 hours in an oxygen flow[4]. Similarly to the Al_2O_3 substrate, the substrate shows atomically flat terraces at its surface after the annealing. An AFM image of a treated $SrTiO_3$ substrate is shown in Fig. 3.3(c).

Film deposition by MBE

Inside the MBE chamber, each substrate requires a different treatment prior to the film deposition. The InP substrates are heated to[5] 510 °C and are kept at this temperature for 15 minutes to ensure the removal of the native oxide layer [88]. During the annealing, a Te flux is applied to prevent phosphorus outdiffusion [89]. Recently acquired scanning transmission electron microscopy (STEM) data, shown in Fig. 3.4, shows that a monolayer is present between the substrate and the first QL. Although no energy-dispersive x-ray spectroscopy (EDX) was performed on the interfacial region, we believe that the layer may be a Te monolayer, originating from the annealing process. This would be similar to observations on films grown on Si(111) [90]. The STEM data furthermore confirms the high quality of the grown film. The Al_2O_3 and $SrTiO_3$ substrates are both annealed at

---

[3] InP substrates are quite brittle compared to the tougher oxide substrates such as Al_2O_3 and $SrTiO_3$.

[4] While it might be tempting to perform the substrate anneal in the MBE chamber *in-situ* before the deposition, the absence of oxygen during the annealing process can render the substrates superconducting [87]. We have observed this as well when the substrate was annealed at 950 °C for 2 hours. The critical temperature of the device was $\sim$ 150 mK.

[5] Substrate temperatures mentioned here have been carefully calibrated and therefore deviate from temperature setpoints of the MBE system itself.

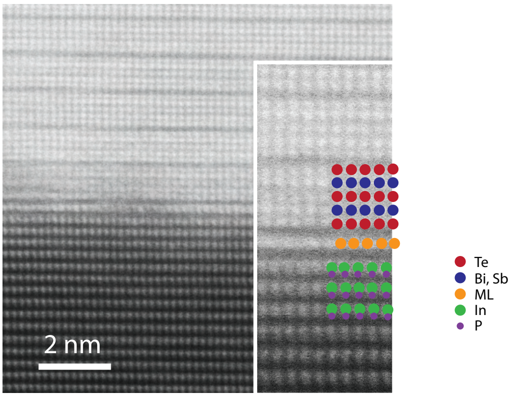

Figure 3.4: Scanning transmission electron microscopy (STEM) image of a BST film grown on an InP substrate[6]. The inset shows a more detailed overview of the interface. Here, some colored spheres have been added to guide the eye. The red and blue spheres show a QL of the BST film (according to Fig. 3.1(a)). The Van der Waals gap can be observed in between different QLs. In between the substrate (green and purple spheres) and the film, a monolayer (ML) is present. We believe that this ML is consisting out of Te atoms.

550 °C for 60 minutes. Both substrates are also kept in a Te-rich environment during the annealing procedure. After annealing, the temperature of the substrate of choice is reduced to the growth temperature of[7] 225 °C. In addition to the Te flux, the shutters of the Bi and Sb crucibles are opened and the substrate rotation is initiated. The growth rate of the films was determined to be 0.07 nm/min and a flux ratio of (Bi+Sb):Te of 1:10 was used. The typical chamber pressure during depositions is $8 \cdot 10^{-11}$ mbar. After growth, all shutters are closed and the substrate and sources are cooled down to room temperature and the resting temperatures, respectively. A RHEED picture is taken to verify the quality of the grown layer, for which we observe streaks, corresponding to 2D film growth [91].

---

[6] This image was acquired during a demonstration session of Hitachi High-Tech for which we have provided samples. The preparation of the lamella, data acquisition and processing have been performed by researchers of Hitachi High-Tech.

[7] This temperature was obtained through the optimization of the growth parameters. A manuscript is being prepared for the results that are presented in this section. Although I have grown films on all substrates presented here, my main involvement in this paragraph was the growth on InP substrates.

Structural characterization
We have prepared thin films of 10 nm on the three substrates for which the growth conditions (i.e. substrate temperature, fluxes of individual crucibles and growth duration) were identical. While x-ray diffraction (XRD) and x-ray photoelectron spectroscopy (XPS) results show that the lattice parameters and stoichiometry of the films are identical, clear differences in morphology were observed in AFM experiments. The results are shown in Figs. 3.3(d-f). All films contain the typically observed QL steps [74, 75, 89, 92]. Triangular domains are present in all films, although the Al_2O_3 and $SrTiO_3$ films also show additional features (masked white regions). The triangular shape is typical for the rhombohedral unit cell, and the spiraling nature of the domains is observed in more films. A detailed description of the nature of the triangular features was given in Ref. [93], where the described growth method is attributed to a difference in growth rate along the different in-plane axes of the crystals. The masked regions in the AFM images of Al_2O_3 and $SrTiO_3$ were investigated further by scanning electron microscope (SEM) measurements. The results of the SEM characterization, along with the film grown on InP, are shown in Figs. 3.3(g-i). The images were taken under a moderate tilt angle. The masked regions in the AFM images correspond to the tilted crystal-like features observed in the SEM images. Additional energy dispersive x-ray spectroscopy (EDX) and electron backscatter diffraction (EBSD) measurements were performed on the samples, but they showed no difference between film and the features. TEM measurement on magnetically doped BST films have shown that the composition of the features is identical to the rest of the film [94]. Furthermore, the features are crystalline, and therefore believed to be misoriented crystallites. Additional TEM studies on our samples, including EDX measurements at the interface, should give more insight in the nature of the crystallites on the different substrates.

3.4 Device fabrication

After film deposition devices are fabricated *ex-situ*. In general, the fabrication process can be subdivided into three steps. However, not all devices require all of the steps. The first step is to etch the film into desired structures. The second step comprises the deposition of a dielectric layer for top gating experiment (optional). The third step is the deposition of metal contacts (also optional, depending on the desired device). We will discuss these steps, including details on the lithography process which is shared among the steps, in detail below.

Lithography

To shape the films and subsequent layers in the desired structures, either optical or electron beam (e-beam) lithography processes are used. For optical lithography, we spincoat OLIN 907-12 photoresist on top of the sample at 6000 RPM for 45 s and successively bake the layer for 1 min on a hot plate at 100 °C. The sample is then placed in the mask aligner and after selecting and aligning the appropriate design, the resist is exposed to UV light with $\lambda = 365$ nm at 10 mW/cm^2 for 7 s. The illuminated parts of the resist are dissolved in diluted AZ-351 developer[8] (AZ-351:H_2O 1:5) for 45 s, after which the development is stopped by soaking the sample in H_2O twice for 30 s. For e-beam lithography, we spincoat the sample with PMMA A4 950 resist at 4000 RPM for 60 s and bake the sample for 5 min at 160 °C. Afterwards, a conductive coating, AR-PC 5090.02, is spincoated on top of the sample at 4000 RPM for 60 s. This layer is baked for 2 min at 100 °C. The conductive coating layer prevents the (insulating) substrates from charging during the e-beam process. Depending on the geometry and process, proximity effect correction (PEC) may or may not be applied to small features. Dose tests have been carried out for different device types and different substrates separately. A typical base dose lies around 650 μC/cm^2, with a beam current of 1 nA and an acceleration voltage of 100 kV. After the exposure, we first remove the conductive coating by bathing the sample in H_2O for 60 s. Then, the resist is developed in diluted MIBK (MIBK:IPA 1:3) for 45 s, after which the development is stopped by soaking the sample in H_2O twice for 30 s.

Etching

Etching the films can be done in different ways, such as Ar ion milling or wet etching[9]. Selecting a suitable method for etching depends on its selectivity for the different materials. Ideally, the film is strongly etched while the substrate is left unharmed. Furthermore, some etching procedures can damage the resist layers used for structuring, which render them impossible to remove, hampering any further fabrication steps.

---

[8] It was found that the standard OPD 4262 developer etches the topological films.

[9] Surprisingly, a surgical blade can also be used to carve a Hall bar into films, a technique that has in fact been used for magnetically doped BST films, which still show a fully developed quantum anomalous Hall effect, regardless of their poorly defined device geometry [20].

Of the two etching techniques available in our lab, Ar ion milling of the TI films is much more reproducible than wet etching. However, we can only use Ar ion milling for films grown on InP and Al_2O_3, as $SrTiO_3$ substrates become highly conductive during the milling process [95], rendering the devices useless. For films grown on InP and Al_2O_3, we etch the films at a power of 50 W with an acceleration voltage of 100 V. The etch rate was found to be 69 nm/min, so that etch times are generally very short (less than 30 s). This is beneficial as longer etch sessions can damage resists (especially e-beam resist) so that they can not be removed afterwards. After the milling process, the resist is removed in acetone. Wet etching is done in a solution of 1HCl: $0.8H_2O_2$: $8CH_3COOH$: $16H_2O$ (volume ratio) [96]. The mass concentrations of the chemicals were 36% HCl, 33% H_2O_2 and 99.7% CH_3COOH. The etch rate was determined to be 30 nm/min, although large fluctuations in the required etching time were observed.

Deposition of the dielectric layer

For top gated Hall bar devices, the second process step is fabricating a dielectric layer. We deposit a layer of 30 nm Al_2O_3 by atomic layer deposition (ALD) at a substrate temperature of 100 °C. We use trimethylaluminium (TMA) and H_2O as precursors. The relatively low substrate temperature is chosen to prevent damage to the film during the process. After the deposition, optical lithography is used once more to structure the oxide layer. The AZ-351 developer etches the oxide layer as well, which is why the development of the resist and the etching of the Al_2O_3 layer is combined. With an etch rate of ~4.5 nm/min in the diluted AZ-351 developer, we develop and etch the layer for a total of 7.5 min. We finish the process by stripping the resist in acetone.

Metal deposition

The final step in device fabrication is depositing electrodes. Depending on the devices, these can be standard Au electrodes (used for top gated Hall bars discussed in this chapter and top gated Hall bars and axion devices discussed in Chapter 6) or superconducting Nb electrodes (for Josephson devices discussed in Chapter 7). After optical or e-beam lithography steps to pattern the resist layer, electrode metals are deposited by sputter deposition. For top gated Hall bar devices, the top gate contact is deposited together with the Hall bar electrodes. To minimize the risk of puncturing the dielectric layer, we omit the deposition of a Ti adhesion layer and perform a soft deposition of Au for the first 10 nm. Here, we use a high Ar

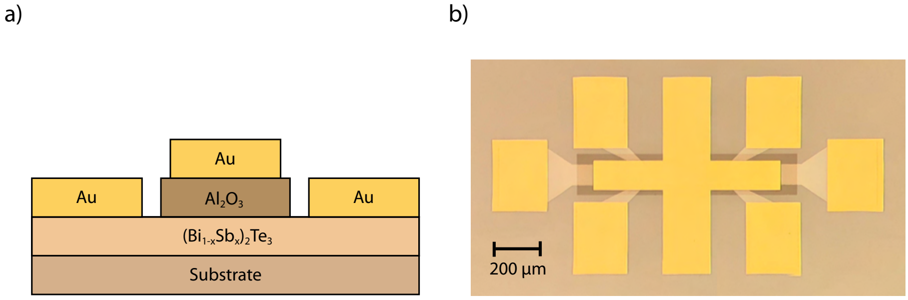

Figure 3.5: Finished top gate devices. **(a)** Side view of a device. The contact electrodes are placed directly on top of the film, while the top gate consists of a dielectric with an electrode on top. **(b)** Optical image of a top gated Hall bar device. The colors of the different layers are identical to those used in panel (a). The TI film is etched into a Hall bar. The top gate consists of the rectangular Al_2O_3 layer followed by an Au electrode. The Hall bar terminals are covered by Au electrode pads as well. The device shown here has a channel width W of 100 μm. The length L between the voltage probes is 400 μm.

deposition pressure of $8 \cdot 10^{-2}$ mbar. The RF forward power is too low to measure, but the target bias is 200 V. Afterwards, we continue with a deposition at a moderate power of 50 W for the bulk Au at a deposition pressure of $2 \cdot 10^{-2}$ mbar. The resulting total thickness of the electrodes is approximately 80 nm. After deposition, the sample is left in acetone overnight, after which it is thoroughly sprayed by a wash bottle of acetone to complete the lift-off process. For the deposition of Nb electrodes, we first clean the surface of the TI by an RF plasma at 10 W for 30 s, to improve the interface quality. After cleaning the Nb target by pre-sputtering for several minutes, a Nb layer of 60 nm is deposited by DC magnetron sputtering at 250 W. To prevent the Nb from oxidation, a capping layer of 2 nm Pd is deposited by RF sputtering at 300 W. During the RF steps we keep the deposition pressure at $1.33 \cdot 10^{-2}$ mbar, while the pressure is lowered to $7.3 \cdot 10^{-3}$ mbar during the DC magnetron sputtering.

Fig. 3.5 shows the final result of the fabrication process of a top gated Hall bar device. Each chip contains 5 different Hall bars with different channel widths W of 10, 20, 40, 60 and 100 μm and a channel length L of 400 μm so that suitable L/W ratio can be chosen: ideally one wants to use a narrow channel to increase the accuracy of the performed measurements, but one should also take care that the total device resistance does not become too large as this will cause problems in combination with the typical filters installed in measurement setups.

3.5 Transport measurements on BST thin films

While top gated Hall bar devices have been fabricated on different substrates (such as InP substrates in Chapter 6), we will limit our discussion to a different type of device here. In efforts to create Josephson junctions of BST thin films (see Chapter 7), we started by fabricating devices on STO substrates. The back gate makes the fabrication significantly easier compared to fabricating a top gate on top of sputter deposited Nb electrodes which are only spaced 40 nm apart. The fabrication process of the device is discussed in more detail in Chapter 7, although all process steps used were already discussed in the preceding text. The most important for the discussion here is that the optical Hall bar does not contain Au electrodes. Instead, Au wires are bonded manually with silver paste directly onto the sample[10]. While the fabricated devices are back gate tunable films rather than the top gate tunable devices that we discussed in Sec. 3.4, their transport properties are very similar.

3.5.1 Magnetotransport

Electronic transport measurements have been performed in a Oxford Triton 200 dilution refrigerator with a base temperature of 20 mK, equipped with a 8 T superconducting solenoid magnet. All magnetotransport measurements were carried out at 500 mK in order to guarantee a stable temperature during magnetic field sweeps, and to make sure that the effects of electron-electron interactions (which we will discuss later in Sec. 3.5.3) are not present. The sample was biased with an ac excitation current of 1 nA and the longitudinal and transverse resistance are measured by standard lock-in techniques in a four probe configuration at a frequency of ~3 Hz. The back gate was trained extensively by repeatedly sweeping the gate voltage up and down a few times over the entire range of interest. The leakage current was found to be smaller than 30 pA over this range.

---

[10] Using conventional wire bonding equipment was found to rupture the films.

In Fig. 3.6(a) we show the longitudinal resistivity[11], $\rho_{\mathrm{xx}} = R_{\mathrm{xx}}/(L/W)$, of a 10 nm $(\mathrm{Bi}_{0.4}\mathrm{Sb}_{0.6})_2\mathrm{Te}_3$ film as a function of applied back gate voltage. The Dirac point (DP), usually referred to as the gate voltage where the resistance is the largest, was found to be at a back gate voltage $V_{\mathrm{BG}} = 65$ V. The resistance remains somewhat higher on the electron-doped side of the DP, which has been reported before for thicker films on SrTiO_3 [98].

We subsequently performed magnetic field sweeps at different gate voltages. The symmetrized longitudinal resistivity and anti-symmetrized transverse resistivity, ρ_{xy}, are shown in Figs. 3.6(b-c), respectively. The longitudinal resistivity increases with magnetic field for all gate voltages, and shows weak anti-localization (WAL) at low magnetic fields. The transverse resistivity has a positive slope for gate voltages larger than the DP, but changes sign for lower gate voltages. This indicates that the transport is no longer mediated by electrons but by holes, as was shown in Fig. 3.1(b). The inverse of the slope of $\rho_{\mathrm{xy}}(B)$ is an indication for the carrier density, and as such we note that the carrier density for the hole-mediated transport is larger than for the electron-mediated transport. This is also reflected in the longitudinal resistivity, which is lower for holes. Recent ARPES measurements have shown that the Dirac point lies very close to the bulk valence band [99], which is consistent with the transport data presented here. Note that the change in sign of ρ_{xy} does not happen at the same voltage as the DP in ρ_{xx}. The thin film hosts surface states at the top and bottom surface, which can have different carrier densities and mobilities. While the bottom layer is in contact with the substrate, the top layer was exposed to air and could be degraded. Also, the gate might tune one surface more effectively than the other surface.

3.5.2 Dual gate measurements

In addition to the back gate tunable Hall bar discussed above, we fabricated top gated Hall bar devices on different substrates. In this section we focus on one particular device, fabricated on SrTiO_3. The excellent back gate tunability of the SrTiO_3 substrate combined with the top gate fabrication process established in Sec. 3.4 leads to a dual gate device. This allows us to

---

[11] Note that strictly speaking a resistivity would have units Ω·m, while here we have units Ω. Throughout this work, we follow the convention where the sheet resistance $R_{\square} \equiv \rho_{\mathrm{xx}}$ and $R_{\mathrm{xy}} \equiv \rho_{\mathrm{xy}}$ and all have units Ω [97] due to the (quasi)-2D nature of the films.

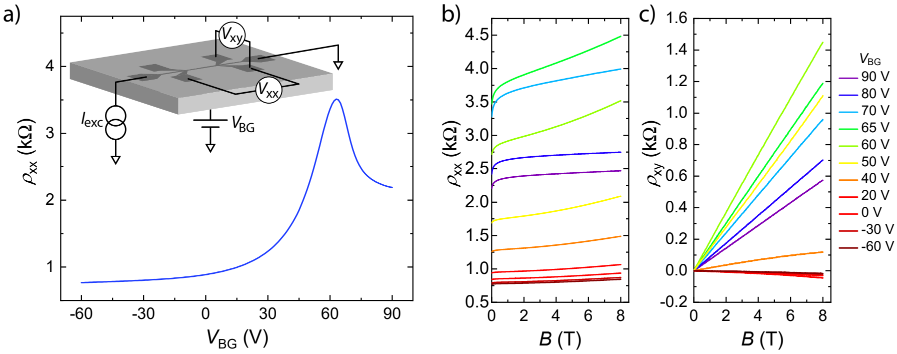

Figure 3.6: Magnetotransport measurements on a 10 nm thick BST film at 500 mK. **(a)** The longitudinal resistivity as a function of back gate voltage. A maximum in the resistivity is found at 65 V, marking the location of the DP. The inset shows a schematic overview of the electrical connections used to perform the measurements. **(b)** The symmetrized longitudinal resistivity as a function of magnetic field for different back gate voltages. The resistivity increases for increasing magnetic fields. **(c)** The anti-symmetrized transverse resistivity as a function of magnetic field. The sign of the resistance changes, indicating a transition from n-type to p-type charge carriers.

gate tune both surfaces simultaneously. A schematic overview of the device is shown in Fig. 3.7(a).

For a dual gated structure, one can measure the longitudinal resistance R_{xx} as a function of the top gate voltage V_{TG} and the back gate voltage V_{BG}. We consider a TI film with a top surface (at the interface with the top gate) and a bottom surface (at the interface with the back gate). Provided that the bulk is sufficiently insulating, different regimes can be attained. We will discuss the two extreme cases. If the film is very thick, the top gate is tuning the top surface only, as the bottom surface is decoupled by the insulating bulk of the material. Vice versa, the back gate only tunes the bottom surface. If one plots $R_{\mathrm{xx}}(V_{\mathrm{BG}}, V_{\mathrm{TG}})$, the resistance would look like Fig. 3.7(b), where blue indicates a low resistance and red a high resistance. Both gates tune their own surfaces independently and hence the increment of R_{xx} due to the top (back) gate takes place parallel to the top (back) gate axis. Such gate maps were reported for thick flakes of BSTS [100]. For these devices, the interlayer coupling, expressed as the capacitance in between the two surfaces of the TI, C_{TI}, is zero. In the other limit, if the film is very thin, the top gate no longer only influences the top surface, but

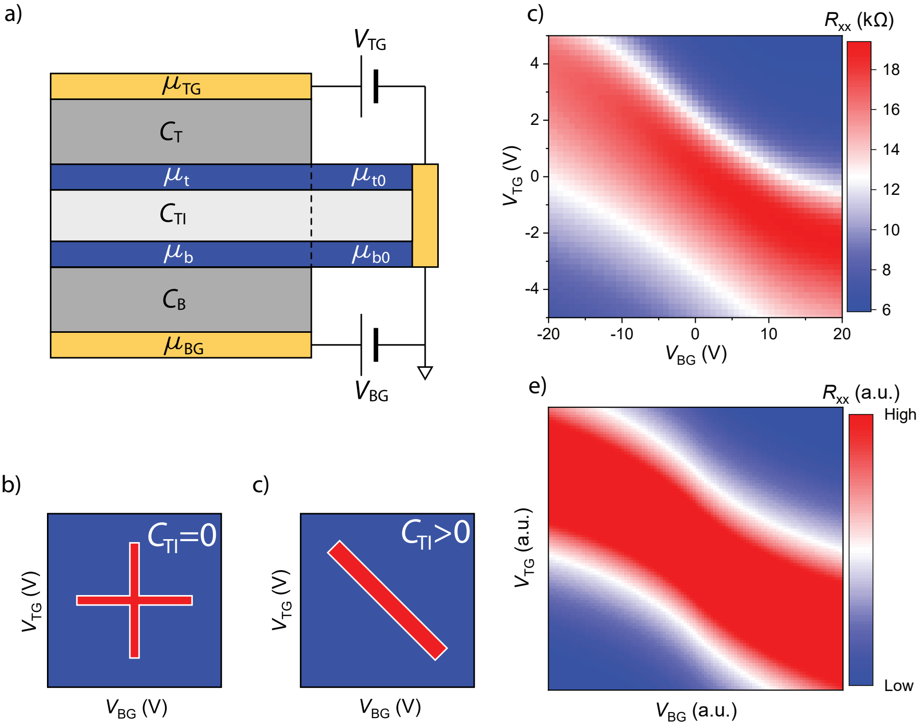

Figure 3.7: Dual gating BST thin films. **(a)** Schematic overview of the dual gate model. The TI film (two surfaces with a bulk dielectric in between) is partially covered by a gate, which resembles the situation of Fig. 3.5(b) **(b)** Schematic overview of a dual gate map of R_{xx} for a device with no interlayer coupling. The blue color corresponds to a low resistance, the red color to a high resistance (DP). Both gates only tune the surface closest to them and hence the shape of the DP is parallel to both axes. **(c)** Schematic overview for a device with a strong interlayer coupling. Both gates influence both surfaces, and as such the DP is a diagonal line. **(d)** Measured dual gate map for a 5 nm BST film. **(e)** Modeled gate map for a BST film on an $SrTiO_3$ substrate.

tunes the bottom surface as well. The same holds for the back gate. The bulk of the film effectively becomes a dielectric between the two surfaces, and hence $C_{TI} > 0$. If both gates influence each other strongly, the DP becomes a diagonal region in gate space, as indicated in Fig. 3.7(c).

We now turn to our measured device. We fabricated a dual gate device on a $SrTiO_3$ substrate. The thickness of the BST film is 5 nm. In Fig. 3.7(c) we show the resistance as a function of top and bottom gate voltages. The gate map reveals a strong diagonal DP, corresponding to a strong interlayer coupling. The qualitative shape of the DP shows that the interlayer coupling is stronger than for previously reported BST devices, which were thicker (exfoliated) films of 17 nm [101]. The curvature in the measured map is attributed to the dielectric function of SrTiO$_3$, since ϵ_r strongly depends on the applied gate voltage [102], leading to non-linear gate characteristics.

We have employed a charging model for the different capacitors in our sample (Fig. 3.7(a)) to show the similarities between data and simulations [36, 37, 101]. The model solves the following set of equations self-consistently:

$$\begin{aligned} n_{\mathrm{t}} - n_{\mathrm{t0}} &= \frac{C_{\mathrm{T}}}{e^2}\left(-\mu_{\mathrm{t}} + \mu_{\mathrm{t0}} + eV_{\mathrm{TG}}\right) - \frac{C_{\mathrm{TI}}}{e^2}\left(\mu_{\mathrm{t}} - \mu_{\mathrm{b}}\right), \\ n_{\mathrm{b}} - n_{\mathrm{b0}} &= \frac{C_{\mathrm{B}}}{e^2}\left(-\mu_{\mathrm{b}} + \mu_{\mathrm{b0}} + eV_{\mathrm{BG}}\right) - \frac{C_{\mathrm{TI}}}{e^2}\left(\mu_{\mathrm{b}} - \mu_{\mathrm{t}}\right), \end{aligned} \tag{3.1}$$

for a given set of gate voltages V_{TG}, V_{BG}, initial carrier densities n_{t0}, n_{b0} and geometric capacitances C_{T}, C_{B}. The chemical potentials are denoted by μ_{TG}, μ_{BG}, μ_{t}, μ_{b}, μ_{t0} and μ_{b0}, where the latter are the initial chemical potentials. After solving the system, the carrier densities and interlayer coupling strength can be determined. The former can be used to transform the data into resistivities by using the Drude model. Fig. 3.7(e) shows the results of our simulations. We incorporated the non-linear capacitance of SrTiO$_3$ and obtained a gate map that has a good qualitative resemblance to the original data. We note that the simulated data is symmetric with respect to positive and negative gate voltages. The measured data has a slight asymmetry, which can be caused due to different initial conditions, as well as trapped charges in the SrTiO$_3$ which alter the strength of the gate dependence for the back gate [103].

3.5.3 Electron-electron interactions at low temperature measurements

After the characterization of BST through standard Hall bar magnetotransport, we fabricated Josephson junctions (see Chapter 7) on the films. A gate tunable Josephson junction would be an ideal platform to explore the rich physics of (topological) Josephson junctions, and as such we first fabricated junctions on SrTiO$_3$ substrates. In fact, the Hall bar presented in Sec. 3.5.1 was fabricated on the same chip as the junctions presented here. Unfortunately, none of the fabricated devices turned superconducting. Instead, we observed an increase in the differential resistance dV/dI for low bias currents I_{bias}. As properties of superconductivity, such as the coherence length, depend on various properties of the BST film, we used the back gate to measure $dV/dI(I_{\text{bias}})$ over a wide range of gate voltages. While we did not find any signs of superconductivity, we found that the peak in dV/dI as a function of I_{bias} was most prominent when the gate voltage was near the DP. In this section, we explore this 'zero bias resistance peak' (ZBRP) in more detail.

In Fig. 3.8(a), we show the differential resistance, dV/dI, of the Josephson junction (blue curve) and the Hall bar (red curve). The differential resistance was measured by standard lock-in techniques where we used an ac excitation current of 1 nA, and for both devices, the resistance has been scaled according to the device geometry. The dimensions of the junction are $L = 40$ nm and $W = 350$ nm, while the Hall bar has $L = 400$ μm and $W = 40$ μm. For both devices, the measurements were performed at the gate voltage which corresponded to the DP. Note that even though the Hall bar[12] is the same device as presented in Sec. 3.5.1, it was measured in a separate session and hence gate characteristics differ between sessions. Strikingly, both devices show a peak in dV/dI near zero bias current, even though their geometries are very different. One could argue that the increase of resistance near zero bias current is simply due to the fact that the heat dissipation ($\sim I_{\text{bias}}^2$) is less, and hence the temperature would lower as a consequence, leading to a larger resistance. However, the fact that a junction (having $R \sim 450$ Ω) and a Hall bar (having $R \sim 40$ kΩ) both show a peak of a similar size means that the effect can not be caused by heat dissipation, because the heat dissipation in the Hall bar is orders of magnitude larger than for the junction.

The ZBRP is thus intrinsic to the film and as such, we consider quantum corrections to the conductivity. Quantum corrections such as WAL are typically observed in thin films (see Fig. 3.6(b)) of Bi-based compounds and have been investigated in detail in Ref. [104] and references therein. However, WAL leads to an increase of the conductivity since backscattering is prohibited for two time-reversed loops that intersect each other. As an applied magnetic field breaks time-reversal symmetry, the effect is destroyed upon applying a magnetic field [105]. This is in correspondence with our ob-

---

[12] Although the Hall bar was fabricated on the same chip as Josephson junctions, it does not have superconducting electrodes.

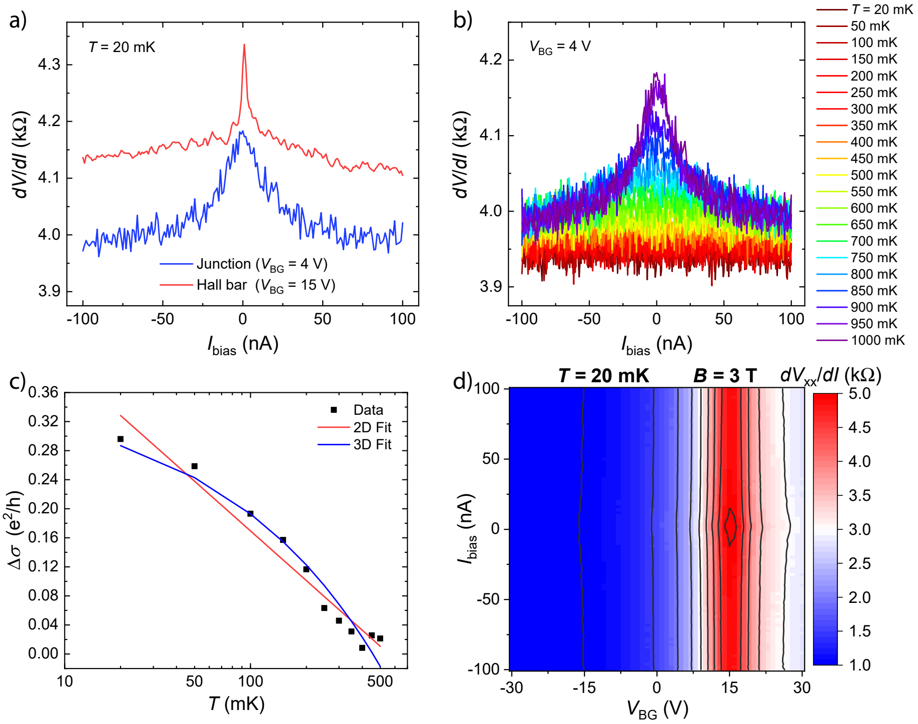

Figure 3.8: Low temperature measurements on BST thin films. **(a)** The differential resistance of a junction and Hall bar device on the same chip. The resistances have been scaled according to the device geometry of the respective devices. **(b)** The differential resistance of the junction device for different temperatures, at a back gate voltage corresponding to the DP. **(c)** The correction to the conductivity plotted as a function of temperature. **(d)** The differential resistance of the Hall bar device at a magnetic field of 3 T, as a function of the bias current and back gate voltage. A small peak near zero bias current is present at the DP.

servations in Fig. 3.6(b) where we see the effects of WAL for small magnetic fields. In the measurements presented in this section, we see an increase of the resistance (a decrease in the conductance), which can not be explained by WAL. While weak localization (WL), i.e. the quantum interference of two trajectories of the same electron traveling in a self-intersecting loop, leads to an increase of the resistance, this effect is also destroyed when a finite magnetic field is applied [106]. We will show that our ZBRP is robust in magnetic field and as such can not be attributed to WL either.

Another quantum correction comes in the form of electron-electron interactions (EEI), where interference between wave functions of two electrons that meet each other twice is considered. As a result of the EEI, the density of states near the Fermi level is reduced [104–106], leading to an increase in the resistance (decrease in the conductance).

For 2D and 3D conduction, the quantum correction due to EEI has a different temperature dependence [106–108],

$$\Delta\sigma_{\mathrm{EEI,2D}}(T) \propto \ln\frac{T}{T_0}, \qquad \Delta\sigma_{\mathrm{EEI,3D}}(T) \propto \sqrt{T}. \tag{3.2}$$

In Fig. 3.8(b) we plot the differential resistance of the junction device as a function of applied bias current. We see that the resistance is largest for small bias currents (or, if voltage biased, voltages). The ZBRP is the strongest for low temperatures and vanishes for temperatures above 400 mK. To see whether our ZBRP could be due to EEI, we convert our differential resistance (in fact, differential resistivity as we already took the geometry into account) into differential conductivity. We then take the difference between the conductivity at a bias current of 100 nA and 0 nA for each temperature and define this difference to be $\Delta\sigma$. Next, we fit the temperature dependencies of Eqn. 3.2 to the data, as shown in Fig. 3.8(c). While studies on $\mathrm{Bi_2Se_3}$ discussed the presence of 2D EEI [105, 107], we show a 3D nature here. While the mean free path l_{mfp} based on the transport data of Fig. 3.6(d) exceeds the film thickness and hence would lead to 2D EEI [106], our films, in contrast to the $\mathrm{Bi_2Se_3}$ samples, have additional bulk states and therefore additional scattering between bulk and/or surface could be an explanation for the 3D nature of the observed EEI.

We should note that WAL has the same temperature dependence as EEI [107], and as such the temperature dependence of Eqn. 3.2 is satisfactory to attribute our findings to EEI. However, EEI is robust in magnetic fields, in contrast to WAL [104, 106]. As such, we perform measurements both in the presence and absence of magnetic fields. Furthermore, we use our back gate simultaneously to tune the Fermi level over a wide range, and we measure dV/dI as a function of both I_{bias} and V_{BG} for different temperatures and different magnetic fields[13]. An example of such measurement is shown in

---

[13] We should note that although we measured the ZBRP as a function of bias current, a more natural energy scale would be to plot the differential resistance as a function of the (measured) voltage. This leads to a very similar figure and shows the energy scale on which the effect takes place. However, since effects such as EEI typically scale with the number of interactions throughout the entire device, it is difficult to convert the voltage into an energy scale that can be compared to temperature itself.

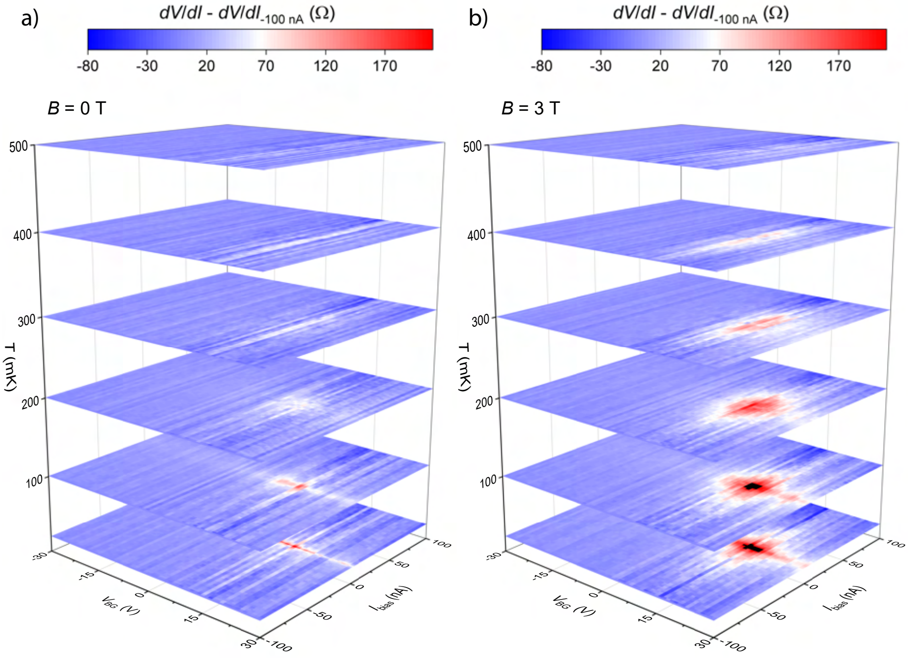

Figure 3.9: Residual differential resistance of the Hall bar devices. The different maps are obtained at different temperatures. The color scale bar is the same for every map. In both panels, the ZBRP is present and decreases with increasing temperature. **(a)** Differential resistance measurements at zero magnetic field. **(b)** Differential resistance measurements at a magnetic field of 3 T.

Fig. 3.8(d), where we show the differential resistance of the Hall bar device at 20 mK and at a magnetic field of 3 T. For all values of the applied bias current, the DP is located at $V_{\mathrm{BG}} = 15$ V. A closer inspection of the differential resistance in the vicinity of the DP and close to zero bias current shows a slight increase of dV/dI. While the size of the ZBRP is $\sim 200\ \Omega$, the changes in resistance due to the back gate are over an order of magnitude larger. To increase the visibility of the ZBRP, we use the following procedure. For a map of $dV/dI(V_{\mathrm{BG}}, I_{\mathrm{bias}})$, we consider each back gate sweep at a fixed bias current individually and subtract the back gate sweep performed at a bias current of -100 nA from it. As such, we essentially remove the influence of the back gate voltage on the overall resistance of the sample and thus can focus on the ZBRP. To verify that the ZBRP does not simply scale with the sample resistance, rendering our procedure to produce incorrect results, we also performed a normalization procedure where we would consider every bias current sweep individually and normalize every sweep by setting $dV/dI(I_{\text{bias}} = 0) = 1$. Both procedures confirm that the ZBRP is present only near the DP.

In Fig. 3.9 we show the maps of the processed data of the Hall bar device at different temperatures and for magnetic fields of 0 T (panel (a)) and 3 T (panel (b)). In both figures, we clearly see that the ZBRP is centered at a gate voltage of 15 V, corresponding to the DP in Fig. 3.8(d), and that it is most prominent near zero bias current. Upon increasing the temperature, the effect becomes weaker and ultimately vanishes around 400 mK, which is consistent with the observations in Fig. 3.8(b). From Fig. 3.9 we can deduce that the quantum correction does not vanish for applied magnetic fields, but rather broadens and increases slightly. The fact that the corrections remain present also strongly points towards EEI.

The quantum corrections are strongest close to the DP. As the density of states has a minimum at the DP, any correction to the density of states will have the strongest influence in the vicinity of the DP. Therefore, the EEI interactions are most prominent near the DP.

3.6 Conclusion

We have grown thin films of $(\mathrm{Bi}_{1-x}\mathrm{Sb}_x)_2\mathrm{Te}_3$ on InP, SrTiO_3 and $\mathrm{Al}_2\mathrm{O}_3$ substrates by MBE. Even though the substrates have their differences, all films exhibit the typical QL structure and have identical lattice parameters. By tuning the ratio between Bi and Sb fluxes, we were able to grow films with low carrier densities which have a Fermi level close to the DP. A fabrication process was established for etching TI films, depositing and structuring $\mathrm{Al}_2\mathrm{O}_3$ by ALD, and depositing normal metal or superconducting metal electrodes. With these tools, we were able to create top gated Hall bars and dual gated Hall bars. Furthermore, the fabrication processes form the basis of the axion devices (Chapter 6) and Josephson devices (Chapter 7).

Standard magnetotransport measurements have been conducted on thin films of BST. Back gating the film on SrTiO_3 shows a clear DP in the longitudinal resistance, which is further confirmed by the measurements in magnetic fields at different gate voltages. Here, we show excellent gate tunability of the devices and observe a transition from electron-mediated transport to hole-mediated transport upon decreasing the gate voltage. In addition, we fabricated a dual gate device on a thin film of BST where we show a strong interlayer coupling between the two surfaces of the TI. A capacitor charging model shows a similar trend compared to the obtained gate map, and can be investigated in more detail to deduce more quantitative results from the data. Finally, we show that a zero bias resistance peak is present for temperatures below 400 mK when the film is gate tuned to the DP. The observed feature is robust in magnetic field and has a square root dependency on temperature, and as such is attributed to 3D electron-electron interactions.

Chapter 4

Magnetic topological insulators

Doping topological insulators with transition metal elements such as vanadium and chromium has led to the observation of the quantum anomalous Hall effect. This electronic phase is characterized by a quantized Hall conductance at zero applied magnetic field. While the material can be used for metrology because of the perfect quantization, the quantum anomalous Hall effect plays an important role in the axion electrodynamics as well. We therefore incorporate vanadium into $(Bi_{1-x}Sb_x)_2Te_3$ *thin films and by using aforementioned fabrication processes and measurement techniques we then study the transport properties and magnetism of the deposited thin films.*

4.1 Introduction

After the discovery of the ordinary Hall effect [109], the anomalous Hall effect (AHE) [110] and the quantum Hall effect (QHE) [111] the question arose whether the quantum anomalous Hall effect (QAHE) could be realized as well. The QAHE exhibits a quantized Hall conductance of $\sigma_{xy} = e^2/h$, even at zero external magnetic field. After the discovery of the telluride topological insulators, such as BST, Yu *et al.* predicted in 2010 that ferromagnetic (FM) ordering in TI systems could be introduced by doping the TI with transition metal elements, such as Ti, V, Cr and Fe [19], leading to magnetic topological insulators (MTIs). In 2013, C. Z. Chang *et al.* experimentally discovered the QAHE in chromium-doped BST (C-BST) [20]. Two years later, the QAHE was also confirmed for vanadium-doped BST (V-BST), where the longitudinal and transverse resistances were even closer to their theoretically predicted values and where the coercive field was much larger [112]. For both dopants, the temperature needs to be extremely low ($\sim$25 mK) in order to measure full quantization of the resistances. Therefore, the search for the QAHE at higher temperatures continued and led to codoping of both vanadium and chromium into BST films (300 mK) [113], modulation doping by having alternating layers of C-BST and pristine BST (500 mK) [114] and recent advances in $\mathrm{MnBi_2Te_4}$ led to full quantization at 1.4 K [115]. Next to the quest for higher QAH temperatures, combining multiple layers of BST, C-BST and V-BST resulted in the realization of so-called axion insulators, with a zero σ_{xx} and σ_{xy} for intermediate fields, in between the coercive fields of the independent dopant layers [61].

In this chapter we present the growth study of the magnetic topological insulator $\mathrm{V}_y(\mathrm{Bi}_{1-x}\mathrm{Sb}_x)_{2-y}\mathrm{Te}_3$ (V-BST), which was performed in parallel to the growth studies of the ternary compound BST. We will first discuss the QAHE in more detail. Then, we discuss how vanadium can be incorporated into the MBE growth process. Finally, we present the structural and electronic characterization of the fabricated thin film devices.

4.2 The quantum anomalous Hall effect

To achieve the QAHE, the material must fulfill the criteria of being a FM insulator that breaks time-reversal symmetry (TRS) and it must have a band inversion. Yu *et al.* [19] found that the latter can be fulfilled by using sufficiently thin telluride topological insulators, and the former could be

realized by doping the material with transition metal elements. Their calculations show that the dopants Cr and Fe lead to an insulating FM state, while V and Ti lead to metallic states due to the nonzero density of states at the Fermi level.
Yu *et al.* [19] attributed the origin for ferromagnetism in the telluride TIs to the Van Vleck paramagnetism. Van Vleck showed that the magnetic exchange among local moments can also be mediated by band electrons [116]. In the dilute limit, the direct coupling among local moments can be neglected. Hence, a sizable susceptibility χ_e of the band electrons is required to get a ferromagnetic phase. While χ_e is negligible for the insulator phase of most dilute magnetic semiconductors, the spin-orbit coupling and band inversion in topological materials such as $\mathrm{Bi_2Se_3}$ lead to a finite χ_e. Therefore, the direct coupling between the Cr (or V) d-orbital and the host valence electrons can lead to a large magnetization, even in the absence of itinerant carriers [117]. The Van Vleck magnetism characterizes itself by being independent of the carrier density, such that the coercive field B_c (the magnetic field required to flip the magnetization of the film) and the Curie temperature T_C (the critical temperature for observing ferromagnetism) remain constant during gate tuning of the material [118].

Another candidate for magnetism in these materials is the Ruderman-Kittel-Kasuya-Yosida (RKKY) mechanism, where the FM coupling is mediated by itinerant electrons. This type of magnetism does depend on carrier density and is thereby distinguishable from the Van Vleck magnetism. While the QAH state requires a ferromagnetic insulator, and thus implies that FM ordering should survive even the absence of itinerant carriers as shown in Refs. [112, 118, 119], reports also show that the RKKY mechanism is found in MTIs [120–123]. Thus, while the QAHE has been measured in different MTI materials, the exact origin of the magnetism is still to be clarified with more experiments and theoretical calculations.

To investigate the interplay between the band inversion and FM ordering, typically a low-energy effective Hamiltonian is used [19]. The model considers the surface states of a 3D topological insulator (such as BST) since the bulk states are gapped [124] and includes hybridization between top and bottom surfaces, along with FM ordering in the form of a Zeeman term.

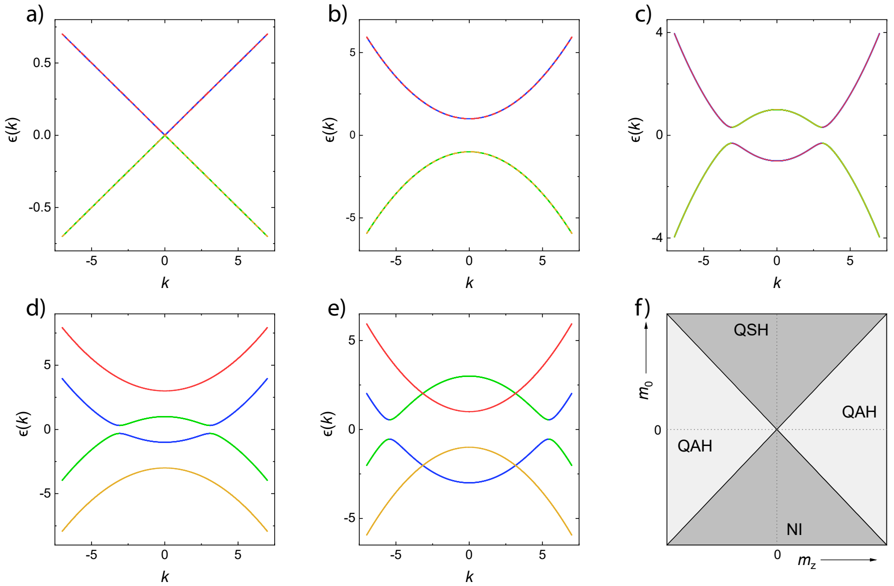

Figure 4.1: Dispersion relations obtained from Eqn. 4.1 for different m_0, m_1 and m_z. **(a)** Degenerate Dirac cones for $m_0 = m_1 = m_z = 0$. **(b)** Trivial insulator state for $m_0 m_1 > 0$ and $m_z = 0$. A gap opens, but the bands are not inverted. **(c)** Quantum spin Hall insulator state for $m_0 m_1 < 0$ and $m_z = 0$. Both bands are inverted, as indicated by the color change in the levels. **(d)** Quantum anomalous Hall state where $m_0 m_1 > 0$ and $m_z > m_0$. Only one band is inverted. **(e)** Quantum anomalous Hall state where $m_0 m_1 < 0$ and $m_z > m_0$. Once again, only one band is inverted. **(f)** Phase diagram for the different values of m_0 and m_z. For $m_z < m_0$ the system can be a trivial insulator (normal insulator, NI) or a quantum spin Hall insulator, depending on the sign of $m_0 m_1$. For $m_z > m_0$ the system is a quantum anomalous Hall insulator, regardless of the sign of m_0.

This Hamiltonian reads

$$\hat{H}(\mathbf{k}) = \begin{bmatrix} m_k + m_z & i v_F k_- & 0 & 0 \\ -i v_F k_+ & -m_k - m_z & 0 & 0 \\ 0 & 0 & m_k - m_z & -i v_F k_+ \\ 0 & 0 & i v_F k_- & -m_k + m_z \end{bmatrix}. \tag{4.1}$$

Here, v_F is the Fermi velocity, m_k is a mass term describing the tunneling effect between the top and bottom surfaces, m_z is the FM ordering (or Zeeman term) and $k_\pm = k_x \pm i k_y$. The basis $|+\uparrow\rangle$, $|-\downarrow\rangle$, $|+\downarrow\rangle$, $|-\uparrow\rangle$ is used, where $|\pm\uparrow\rangle = (|t\uparrow\rangle \pm |b\uparrow\rangle)/\sqrt{2}$, $|\pm\downarrow\rangle = (|t\downarrow\rangle \pm |b\downarrow\rangle)/\sqrt{2}$. $t(b)$

represent the top (bottom) surfaces and ↑ (↓) represent spin-up (spin-down) modes. The mass term m_k is typically expanded up to the second order as $m_k = m_0 + m_1(k_x^2 + k_y^2)$. Without any magnetization (i.e. $m_z = 0$) we distinguish three different cases. When $m_0 = 0$, the system is gapless and the typical linear dispersion relation for $\epsilon(\mathbf{k})$ is obtained, as shown in Fig. 4.1(a). When $m_0 m_1 > 0$, a gap opens and the material is a trivial insulator with no inverted band structure (Fig. 4.1(b)). Alternatively, for $m_0 m_1 < 0$ the bands do invert, leading to the quantum Spin Hall (QSH) insulator (Fig. 4.1(c)). When a Zeeman exchange interaction is introduced, the system can be driven from the (non-)inverted insulator state to the QAH state when the FM ordering is strong enough. More specifically, when $|m_z| > |m_0|$ only one of the bands will be inverted, regardless of whether the system initially had no inverted bands (trivial insulator, Fig. 4.1(d)) or two inverted bands (QSH insulator, Fig. 4.1(e)). Upon varying both m_0 and m_z, one can generate the phase diagram of Fig. 4.1(f) [124]. Here, we see the interplay between the hybridization energy and the Zeeman exchange energy. Whenever $|m_z| > |m_0|$ the system is in the QAH state, while otherwise it is a QSH insulator or trivial insulator (normal insulator, NI), depending on the sign of m_0.

If the system is in the QAH state, the surface states perpendicular to the magnetization vector are gapped. It was shown that the topological invariant for such system, called the Chern number C, depends on the sign of the mass gap [28, 125]. The conductivity of the system can be computed through the TKNN formula, $\sigma_{\mathrm{xy}} = (e^2/h)C$ and for the QAH system this leads to $\sigma_{\mathrm{xy}} = \pm e^2/h$ [10, 19].

4.3 Molecular beam epitaxy of V-BST thin films

In Chapter 3 we have discussed the thin film deposition of topological tellurides by molecular beam epitaxy (MBE). Here, we incorporate vanadium into our BST films in search for the QAH state. The crystal structure of V-BST is equal to BST, where the vanadium doping atoms simply reside at lattice sites of Bi/Sb in the unit cell (see Fig. 3.1(a)) [112]. Vanadium is typically evaporated from either an e-beam evaporator [112] or a (high-temperature) Knudsen cell [61, 126]. Our MBE system is equipped with both types of sources. We started the film growth with vanadium doping by e-beam evaporation and, after the first optimization steps of the film growth, noted that both the vanadium content as well as the film quality varied from sample to sample, even when using the exact same growth

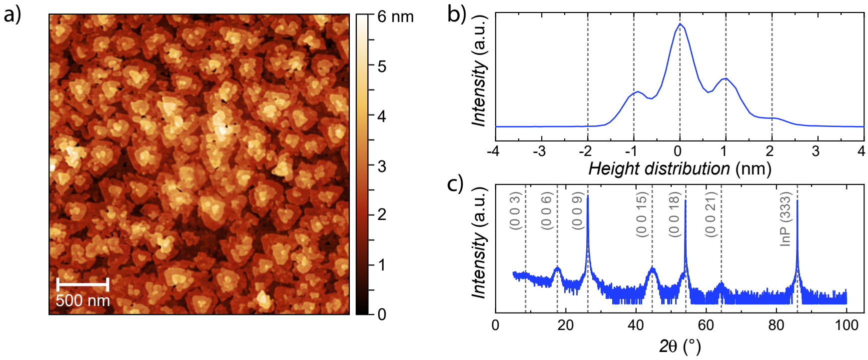

Figure 4.2: Structural characterization of a 10 nm V-BST thin film. **(a)** 3 μm×3 μm AFM image of the V-BST film. The film shows QLs and some triangular features. **(b)** Height distribution extracted from a 10 μm×10 μm AFM scan of the same thin film as shown in panel (a). The most intense peak is offset to zero. Three distinct QL levels are present. **(c)** Symmetric x-ray diffraction scan of a thin film. The family of (0 0 3n) peaks is visible. The (0 0 9) and (0 0 18) peaks of the film coincide with the (111) and (222) peaks of the substrate, respectively.

parameters. Possible reasons for this are discussed in the Appendix. The transition towards a high-temperature Knudsen cell led to improved reproducibility of the deposited films.

In this chapter, we focus on the deposition of V-BST on InP substrates. We use the substrate preparation and pre-anneal steps as outlined in Sec. 3.3. The film deposition itself is also similar to that of BST, with the addition that the shutter of the vanadium cell is opened simultaneously with those of Bi and Sb. We again use a flux ratio of (V+Bi+Sb):Te of 1:10 and use substrate temperatures ranging from 195-225 °C. The substrate temperature can thus be lowered with respect to the optimal temperature for the deposition of BST. The reason for this is the high temperature that is required to evaporate vanadium. Typically, for doping applications, the Knudsen cell is heated to 1650 °C. At such high temperatures, the cell also emits a considerable amount of heat via radiation, and as such the substrate is heated additionally. The lower deposition temperature for V-BST was also reported elsewhere [61].

In Fig. 4.2 we show the results of structural characterization of our 10 nm V-BST films. The 3 μm×3 μm AFM image in panel (a) shows the quintuple layer (QL) structure that was observed for the growth of BST as well (see

Fig. 3.3). While for BST triangular mounds are present, their occurrence in V-BST is less, with more randomly shaped spiraling structures. The random shape, which contains jagged features, is more commonly observed for magnetic topological insulators [112, 126, 127]. Fig. 4.2(b) shows the height distribution taken from a larger 10 μm×10 μm AFM image of the sample film of panel (a). The spectrum was shifted so that the largest peak corresponds to 0 nm on the height-axis. It is clear that the film mostly consists out of three different QL levels. We will comment on the importance of the height distribution later. In Fig. 4.2(c) we show the results of a symmetric XRD scan. We observe the family of out-of-plane (0 0 3n) peaks for the film and the (111) family for the InP substrate. The overlap between the (0 0 9) peak of the film and the (111) peak of the substrate, as well as the (0 0 18) and (222) peak, indicate the small lattice mismatch between the film and substrate. From the (0 0 15) peak, we deduce that the *c*-axis lattice parameter is 30.44 Å, which is in line with unit cell parameters reported elsewhere [128].

4.4 Transport measurements on V-BST thin films

We now turn to the transport results of the V-BST films. We first focus on a single device to discuss the basic magnetotransport measurements that are conducted on magnetic TI films. After introducing the relevant properties of magnetic (topological) materials, we show a more detailed analysis of the magnetism in our films.

4.4.1 Magnetotransport at low temperatures

The QAH state in homogeneously doped MTI samples such as our V-BST can only be observed for temperatures lower than $\sim$ 50 mK, due to the maximum of the bulk valence band (BVB) being higher in energy than the DP, as was shown in ARPES measurements in Ref. [129]. These impurity states, caused by the vanadium doping, need to be localized before one can observe the QAH effect. Anderson localization has been suggested as the responsible mechanism [129, 130]. To see if our films exhibit the QAH effect, we performed magnetotransport measurements on structured devices in an Oxford Triton 200 dilution refrigerator with a base temperature of 20 mK, equipped with an 8 T superconducting solenoid magnet. A current of 1 nA was sourced through the device and the longitudinal and transverse

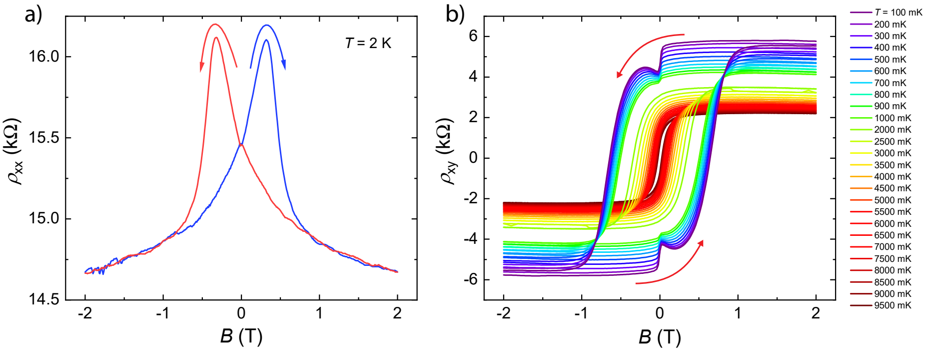

Figure 4.3: Magnetotransport for a 10 nm $V_{0.08}(Bi_{0.4}Sb_{0.6})_{1.92}Te_3$ film deposited on InP. **(a)** Longitudinal resistivity ρ_{xx} as a function of magnetic field at 2 K. The field is swept upwards and downwards. The sweep direction is indicated with red arrows. **(b)** Transverse resistivity ρ_{xy} as a function of magnetic field. The data is anti-symmetrized.

resistivities were measured in the same configuration as for the BST Hall bar (for a schematic drawing, see Fig. 3.6(a)). We magnetize the sample by applying an out-of-plane magnetic field larger than the coercive field B_c (i.e. the field required to flip the magnetization). Then, we measure the longitudinal and transverse resistivities as a function of field by sweeping the magnetic field up and down.

Fig. 4.3 shows the transport data of a 10 nm $V_{0.08}(Bi_{0.4}Sb_{0.6})_{1.92}Te_3$ Hall bar. The transverse resistivity ρ_{xy} contains a hysteresis loop, as shown in Fig. 4.3(b). The arrows indicate the sweep direction per curve. The magnetization of the film only flips when the direction of the field is opposite with respect to the magnetization of the film and when the applied field exceeds B_c. When the magnetization is flipped, ρ_{xx} increases and hence contains the peaks as observed in Fig. 4.3(a). The observed dips in the ρ_{xy} curves for low temperatures after passing through zero field are caused by heating effects. We observe that the size of the loop in ρ_{xy} decreases in field (i.e. B_c) and amplitude (i.e. the magnetization) for increasing temperatures, as typically observed for magnetic topological insulators [20, 112, 118, 120].

We can use the magnetotransport data to calculate the carrier density as well. The transverse resistivity of a sample exhibiting the anomalous Hall effect can be described by an empirical equation [131],

$$\rho_{\mathrm{xy}}(B) = \rho_{\mathrm{OH}}B + \rho_{\mathrm{AH}}M(B). \tag{4.2}$$

Here ρ_{OH} is the ordinary Hall effect, which typically depends on the Drude model, ρ_{AH} the prefactor for the anomalous Hall contribution, and M is the magnetization. The slope of ρ_{xy} outside of the magnetization loop is dictated by ρ_{OH}, and the inverse of this gives a good indication for the carrier density of the material. We measured ρ_{xy} over a wider range of magnetic field values than shown in Fig. 4.3(b) and found $n_s = 3.3 \cdot 10^{12}$ cm^2, which is low, but still an order of magnitude larger than reported for films exhibiting the QAH effect [132]. The large carrier density may be a reason why the measured film does not develop a QAH state, since the Fermi level will probably reside outside of the magnetization gap. Nevertheless, we can learn more about the magnetism in these films.

4.4.2 Magnetism in V-BST films

In Sec. 4.2 we discussed the Van Vleck and RKKY mechanisms that have been observed in magnetic topological insulator thin films. Here, we investigate the magnetism in our films by means of various transport measurements. We compare our results with reported values on Cr-doped BST or V-doped Sb_2Te_3 with small doping.

Determining the magnetic interaction

We start with a top gated Hall bar device (for fabrication details, see Sec. 3.4) of V-BST[1]. The RKKY and Van Vleck magnetism are typically distinguished by their dependence of the Curie temperature or the coercive field on temperature [28, 118]. The value of the coercive field is easily obtained from standard transport measurements, but changes in its value can not be accurately used to determine the type of magnetism, as we will show in the Appendix. The Curie temperature can be measured in various ways. Chang *et al.* [118] use the temperature dependence of ρ_{AH}, and define the Curie temperature as the temperature for which ρ_{AH} at zero field changes from zero to a finite value. A more accurate method to determine the Curie temperature is the use of Arrott plots. Arrott argued that a measurement method based on finite magnetic fields would be more desirable, since magnetic impurities with a larger Curie temperature than the bulk of

---

[1] In fact, low temperature data presented in the previous section is obtained from the same top gated Hall bar sample.

the material, or other inhomogeneities, can obscure the Curie point when it is determined at zero field [133].

Arrott plots are constructed as follows. The magnetic susceptibility χ can be modeled as $\chi \sim (T - T_C)^{-1}$, which diverges at the Curie temperature. The field dependence of the magnetization close to the Curie temperature can be modeled as $B = \chi/M + aM^3 + bM^5 + \ldots$ [133]. At the Curie temperature this reduces to $B = aM^3 + \mathcal{O}(M^5)$. If we plot M^2 as a function of B/M, this will be a straight line passing through the origin. This method was used for MTI samples to determine the Curie temperature, where ρ_{xy} was used instead of magnetization [112, 134]. When ρ_{xy} is measured as a function of magnetic field for different temperatures, there will be one temperature (the Curie temperature) for which ρ_{xy}^2 as a function of B/ρ_{xy} will intercept the origin.

We conducted Arrott measurements in a Quantum Design Dynacool Physical Properties Measurement System equipped with a 9 T solenoid magnet. Commercial SR830 lock-in amplifiers were used to source and measure the resistivities. The source voltage of 1 V was converted into a source current of 100 nA by means of a series resistor of 10 MΩ. The gate voltage was applied by a Keithley 2400 source-measure unit. In Fig. 4.4(a) we show the gate tuning of the longitudinal resistivity of the 10 nm $\mathrm{V_{0.08}(Bi_{0.4}Sb_{0.6})_{1.92}Te_3}$ film at a temperature close to the Curie temperature. No DP can be observed yet over the entire gate range. For the Arrott measurements, the ferromagnetic state must be approached from temperatures above T_C [112], and as such we first perform magnetotransport measurements over a large range of descending temperatures. After finding the appropriate Curie temperature, which was close to 43 K, we narrow down our region of interest and perform the temperature-dependent measurements for a wide range of gate voltages. Note that for every gate voltage, we first raise the temperature of the sample to 50 K. Then, we perform sweeps of the magnetic field for the different descending temperatures.

Fig. 4.4(b) shows the Arrott plot for a gate voltage of -10 V. We performed magnetotransport measurements to obtain ρ_{xy} for up and down sweeps of the magnetic field over a range of ± 2 T. The data is anti-symmetrized, and ρ_{xy}^2 is plotted against B/ρ_{xy} to obtain the shown figure. The dashed lines are linear extrapolations of the data at large field towards zero field. While the linear part of the data in the Arrott plots for these materials is not very large [112, 134, 135], a careful analysis still provides a reasonable analysis. It is evident from the figure that the intercept changes from being negative

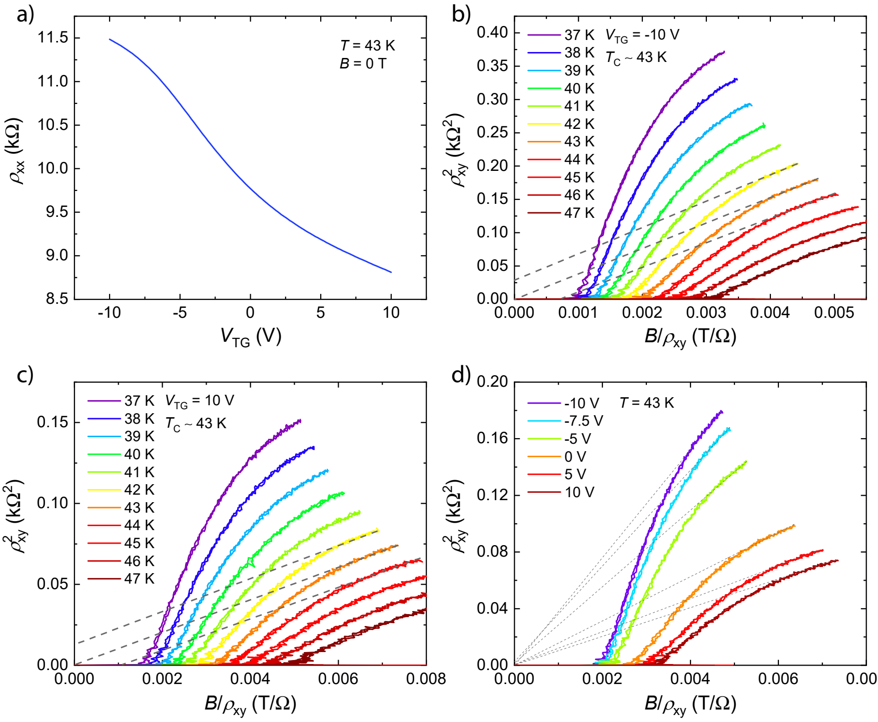

Figure 4.4: Arrott measurements on a top gated V-BST film. **(a)** Gate dependence of the longitudinal resistivity at elevated temperatures. **(b)** Arrott plot at a gate voltage of -10 V. The Curie temperature is determined by extrapolating the linear part of every curve. The curve that passes through the origin marks the Curie temperature, which for this gate voltage is determined to be 43 K. **(c)** Arrott plot at a gate voltage of 10 V. While the resistivities change significantly, the Curie temperature remains the same. **(d)** Arrott plot where the curves for all investigated gate voltages are plotted for the Curie temperature of 43 K. The curves of all gate voltages pass through the origin.

to positive at 43 K, so this temperature is marked as the Curie temperature. In Fig. 4.4(c) we show an Arrott plot for a gate voltage of +10 V. Although the resistivities are different at this gate voltage, it is immediately clear that the Curie temperature did not change. To further emphasize the independence of the Curie temperature on the gate voltage, we performed Arrott measurements for a range of intermediate gate voltages. The results of the curves obtained at 43 K are shown in Fig. 4.4(d). For every gate voltage the linear extrapolation passes through the origin.

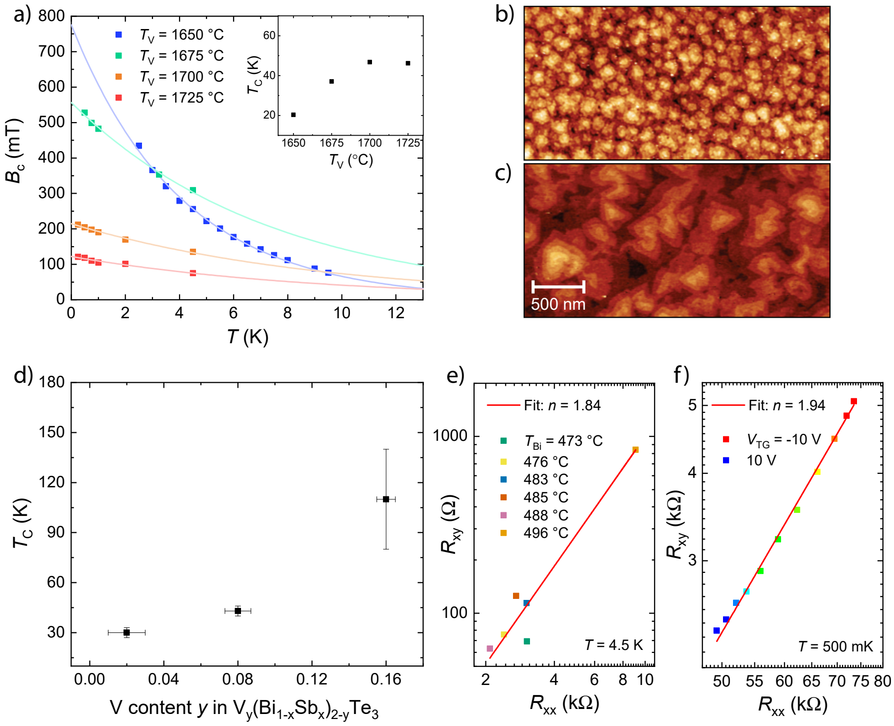

Figure 4.5: Magnetism in V-BST thin films. **(a)** The coercive field as a function of temperature for different doping levels. The inset shows an estimation of the Curie temperature. **(b)** AFM image of the sample for which the vanadium cell was at 1725 °C. **(c)** AFM image of the sample for which the vanadium cell was 1650 °C. **(d)** Curie temperature as a function of the vanadium doping as determined by XPS. **(e)** Anomalous Hall scaling for samples with a different Bi concentration. **(f)** Anomalous Hall scaling for the device of Fig. 4.4 for different gate voltages.

The independence of the Curie temperature on the gate voltage and thus on the carrier density suggests the Van Vleck magnetism to be the responsible mechanism for the magnetism in the deposited V-BST thin films. This is in agreement with measurements on films with a comparable vanadium doping [112, 119]. It should be noted that the RKKY magnetism in V-doped films is typically observed for films with a doping level that was less than our films [121, 136]. The observation of Van Vleck magnetism in our films will become important in Chapter 6.

Influence of the V concentration

Yu *et al.* [19] showed in their calculations that the exchange energy related to the van Vleck mechanism scales linearly with the amount of magnetic dopants. Hence, one expects the Curie temperature to have the same scaling behavior as well [118]. To study this, we varied the vanadium concentration by changing the temperature of the vanadium cell. We deposited four films with a different vanadium doping, where for each of the films, the temperatures of the Bi, Sb and Te cells were kept the same, as well as the substrate temperature and growth duration. The samples were structured into Hall bars and magnetotransport measurements were conducted in an Oxford Triton 200 dilution refrigerator. The coercive field of the films was extracted for different temperatures, see Fig. 4.5(a). The data can be fitted well with an exponentially decaying function. We extract a crude estimate of the Curie temperature by using the fits to the data[2]. Our data set reveals that the Curie temperature increases with increasing temperature of the vanadium cell. This is in line with the suggestion of van Vleck magnetism from our Arrott analysis. We furthermore note that the samples with a larger vanadium doping level have a smaller coercive field. The difference in coercive fields between V-doped and Cr-doped films has been attributed to having larger (magnetic) domains in the former material [112]. Here, we suggest that a similar scenario is true for different doping levels, i.e. different doping levels might provide a different size of the domains. To confirm this, we compare the AFM images of two films of the data set of Fig. 4.5(a). In Fig. 4.5(b) we show an AFM image of the film with a vanadium cell temperature of 1725 °C. In Fig. 4.5(c), at the same lateral scale, we show an AFM image of the film with a vanadium cell temperature of 1650 °C. It is evident that the domain sizes in the latter film are much larger than for the one with a higher vanadium cell temperature. While AFM images only give information on the morphology of the sample and not on the structure of magnetic domains, our data suggests that further investigation (such as magnetic force microscopy or a scanning SQUID microscope with a lateral resolution < 1 μm, see Ref. [137]) may give more insight into the correlation between structural and magnetic domains.

For a few samples we have performed x-ray photoelectron spectroscopy (XPS) experiments to determine the exact doping concentration. For two of these films, Arrott measurements have been performed to determine the

---

[2] For an electrical RC network, the (dis)charging can be fitted with $e^{-t/\tau}$. A capacitor is regarded to be fully (dis)charged at $t \approx 5\tau$. We performed the same methodology here to obtain our crude estimation of the Curie temperature. We fit our data with $B_c(T) \sim e^{-T/\tau}$ and then consider the coercive field to be zero ('discharged') at $T_C \approx 5\tau$.

Curie temperature. For another film, the Curie temperature was determined from the kink in $\rho_{\text{xx}}(T)$, which is more often observed when the resistance of the sample is recorded during the cooldown procedure [138]. The results are shown in Fig. 4.5(d). Note that the error margin in Curie temperature is much larger when it is determined from a kink in ρ_{xx}, and note that the error margin increases for smaller V doping levels as the signal-to-noise ratio for the XPS peaks becomes worse. However, it is clear that increasing the doping concentration leads to a larger Curie temperature. While the value of the Curie temperature is comparable to those found in Ref. [138], these values are larger than those reported in Ref. [112]. The difference between the referenced data may lie in the film thicknesses which differ over an order of magnitude. Furthermore, in our system we incorporated V dopants into BST rather than into Sb_2Te_3 and as such the spin-orbit coupling of the heavier Bi atoms may enhance the susceptibility of the Van Vleck magnetism. Most importantly, the increase in Curie temperature with doping concentration once more hints towards the Van Vleck magnetism in our films.

Anomalous Hall effect

We already discussed an empirical equation for the anomalous Hall effect in Eqn. 4.2. The prefactor ρ_{AH} typically depends on the longitudinal resistivity. One can extract information about the mechanism responsible for the AHE by determining the coefficient n in $\rho_{\text{xy}} \sim \rho_{\text{xx}}^n$. If skew scattering is the dominant process, the coefficient is 1, while intrinsic or side-jump mechanisms as cause for the AHE lead to a coefficient of 2. Here, intrinsic means that the contribution depends on the band structure and that it is largely independent of scattering [131].

We compare two sets of data to analyze the mechanism responsible for the AHE. Firstly, we change the carrier concentration by changing the ratio of Bi and Sb. We should note that this study was performed on an early set of films where vanadium was still incorporated with an e-beam evaporator. Nevertheless, the data, shown in Fig. 4.5(e) reveals a clear trend between ρ_{xx} and ρ_{xy}. We note that for these films $\rho_{\text{xy}} \approx \rho_{\text{AH}}$ outside of the loop. We fit our expression to the data and find $n = 1.84$. In addition to this data set, we also consider the top gated sample that we discussed before, as shown in Fig. 4.5(f). Here, we change the carrier concentration by means of a gate voltage. We perform the same data analysis and retrieve $n = 1.94$. From this, we deduce that the skew scattering mechanism can not be responsible for the AHE in our samples. The side-jump mechanism is proportional to

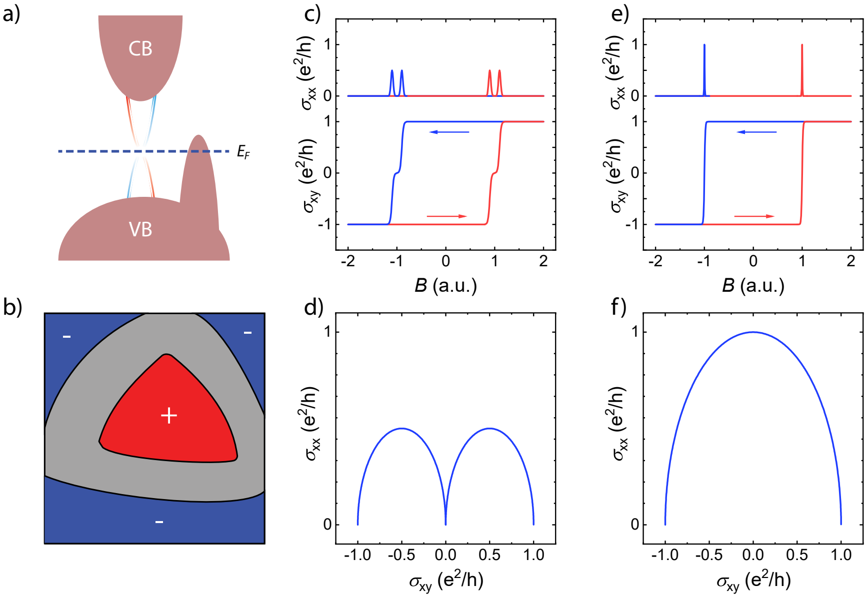

Figure 4.6: Schematic figures concerning quantum anomalous Hall materials. **(a)** Schematic band structure of V-BST. **(b)** Variations in V-BST can lead to an insulating state during the reversal of the magnetization. The variation can either be related to thickness or due to different magnetic domain sizes. **(c)** Schematic representation of conductivities for thin QAH films. **(d)** Tensor flow diagram belonging to panel (c). **(e)** Schematic representation conductivities for thick QAH films. **(f)** Tensor flow diagram belonging to panel (e).

the carrier density [118] and was thus discarded for the Cr-doped samples, as the QAH effect (and its magnetism) are robust even in the absence of itinerant carriers. Here, we thus find the intrinsic mechanism to be likely responsible for the AHE in V-doped TI films.

4.5 Discussion

Despite the structural, magnetic and morphological quality of our MTI films, no quantum anomalous Hall effect has been observed so far. It is essential to understand why the effect has not been observed yet, so that future depositions of the material may eventually lead to films exhibiting the effect.

The first and foremost reason for the absence of the QAH effect is the position of the Fermi level. In various studies on the QAH system it has been shown that the ratio between Bi and Sb should be tuned carefully [20, 112, 118]. Similarly to BST, the tuning changes both the position of the Fermi level, as well as the position of the DP itself (see the band structure in Fig. 4.6(a)). Our attempts of varying the Bi temperature in Fig. 4.5(e) have led to the change of carrier type (based on the Hall resistance), but these films were 30 nm in thickness and hence were too thick (and too metallic) for the QAH effect to appear. We will discuss the thickness in more detail later. While vanadium was incorporated in these films by an e-beam evaporator, the doping in the latest films was incorporated through the high-temperature Knudsen cell. Here, the primary focus has been to first tune the V dopant level and get reproducible films for the transport measurements. With a good control of the vanadium concentration and an understanding of the influence of the doping level, this knowledge should be combined to carry out a systematic growth study where the ratio of Bi and Sb must be further tuned.

A different reason is variation of film thickness observed in the samples. From the AFM analysis in Fig. 4.2 we deduced that the typical height variation in a sample was 3 QLs. For samples of which AFM images were available (see the Refs. mentioned in Sec. 4.3) the height variation seems to be very similar. The thickness of the sample is of importance because of the requirements to observe the QAH effect. Recall the conditions that were set in Sec. 4.2: the QAH effect will only occur when $|m_z| > |m_0|$, i.e. when the magnetization energy is larger than the hybridization between the two surfaces. The hybridization term is strongly dependent on the film thickness and oscillates between positive and negative values [139]. One can imagine that if our ‘nominal’ layer is 5 nm thick, there will be thicker layers (less hybridization) and thinner layers (more hybridization). Hence, different layer thicknesses may be either NI, QAH or QSH, in the framework of Fig. 4.1. The system then becomes a percolation system where a path should be found that connects the QAH layers together. Ideally, the films should thus have as less height variation as possible. We should note that the scenario investigated here could theoretically also happen for a film that is uniform in height. The different regions in Fig. 4.6(b) are then simply magnetic domains with different domain sizes, so that they flip their magnetization at different coercive fields. If the uniform film is thin so that the hybridization term is large, the system will also be in the NI / QSH state upon reversal of the magnetization. While (V-)BST films always have a finite height distribution due to the presence of rotational twins [63], magnetic domains may have a different size than structural domains and therefore in principle both the thickness variation as well as domain size variation can lead to an intermediate state.

In different studies the height of the Cr-doped and V-doped samples were varied to study the thickness dependence of the QAH effect [31, 132, 140]. We should note that the method of extracting the film thickness is not specified, or is difficult to interpret[3]. However, a distinction can be made between 'thin' and 'thick' (or 2D and 3D) films. The 2D films would be characterized by the existence of a hybridization term that competes with the magnetization. When the magnetization is reversed, the magnetic moment of the film is minimized and the hybridization can dominate in thin parts of the film [140]. Consider the schematic picture of Fig. 4.6(b). The blue and red parts of the film are thick enough so that they retain their magnetization, i.e. $|m_z| > |m_0|$. However, the region in between is thinner and thus has $|m_0| > |m_z|$. The grey region now has the properties of a normal insulator and thus no current path exists throughout the piece of material shown in the figure. For such thin films, during the reversal of the magnetization both σ_{xx} and σ_{xy} (obtained from the resistivities through tensor inversion) go to zero. This corresponds to the trend depicted in Fig. 4.6(c) and (d), where the latter shows a different representation of the data. For 3D films, the hybridization term is so small that there is no point during the reversal of the magnetization where parts of the film will become insulating. Hence, the transition happens at once and corresponds to the schematic trend shown in Fig. 4.6(e) and (f). Note that while the plateau at $\sigma_{\mathrm{xx}} = \sigma_{\mathrm{xy}} = 0$ in 2D films is attributed to differences in m_z [140, 141], the thick samples are also seen as candidates for axion electrodynamics [31, 125], which was discussed in detail in Chapter 2. We end our discussion by noting that the crossover between 2D and 3D was reported to be 6 nm [31, 140]. An upper limit to the thickness of QAH samples was proposed to originate from bulk carriers being more present in thicker films [63], due to conducting side surfaces and the asymmetry in band bending of both surfaces due to the substrate [132].

---

[3] X-ray reflectometry measurements have been performed in Ref. [31] to obtain thicknesses that are fractional numbers. If AFM images of the films would be present, it would still be a difficult task to pinpoint which layer corresponds to what thickness.

4.6 Conclusion

In this chapter we explored the incorporation of vanadium into our BST thin films. While the QAH effect has not yet been observed, we have gained good control over the growth parameters and report the deposition of high-quality films. Hall bar devices, including top gated Hall bars, have been fabricated to investigate the magnetic properties of the devices. We find strong evidence from multiple experiments that the magnetism is of the Van Vleck type. This is an important observation regarding further experiments on the thin films that will be discussed in Chapter 6. While the topological magnetoelectric response in the experiment in Chapter 6 may be strongest for a film that shows the quantum anomalous Hall effect (or a film that has minimal conducting states which might diminish the effect), we can still use the current films to search for a topological response in the measurement setup that we will introduce later. We note that in addition to the optimization of the stoichiometry, the thickness (variation) of the films plays an important role in the physics of the quantum anomalous Hall effect and the intermediate plateau observed in thin films.

Appendix A: Coercive field in anomalous Hall devices

In the main text, we discussed how the anomalous Hall effect can modeled by the empirical relation of Eqn. 4.2. Furthermore, we claimed that the coercive field of the material can not be used reliably to argue whether the magnetization of a sample is Van Vleck or RKKY. Such (partial) claim was made in Ref. [28], where the constant coercive field was considered to be an indication of Van Vleck mechanism, along with the observation of a constant Curie temperature over the gate dependence.

Here, we show with a simple model that one should be cautious in considering coercive fields as a sole indication of magnetic properties of the film. Let us consider a material that is characterized by a single carrier type. We employ the Drude model and use a fictitious gate dependence of the carrier density as shown in Fig. A.1(a). The carrier density enters Eqn. 4.2 through $n_s = [e \cdot d\rho_{\mathrm{xy}}/dB]^{-1}$. We now add magnetism to the model. The typical shape of the magnetization M can be approximated by a hyperbolic tangent [142], and the prefactor ρ_{AH} is proportional to ρ_{xx}^2 (see Sec. 4.4.2). We obtain

$$\rho_{\mathrm{xy}} = \frac{1}{n_s e} B + \alpha \rho_{\mathrm{xx}}^2 \tanh\left(\frac{B \pm B_c}{B_s}\right). \tag{A.1}$$

Here α is a proportionality factor, B_c the coercive field and B_s the saturation field. We plot the obtained transverse resistivities for the gate dependence in Fig. A.1(b), where we chose $B_c = 1$. It is clear that a lower carrier density, leading to an increase in ρ_{xx}, leads to a larger loop. It seems that the 'measured' coercive field is constant with gate voltage. However, if we zoom in (see panel (c)), we observe that the coercive field, defined as $B(\rho_{\mathrm{xy}} = 0)$ changes significantly. All curves collapse at the model's B_c, but at a finite ρ_{xy}. If we now extract the 'measured' coercive field and plot it as a function of gate voltage, we see that the value changed by 10 percent. This change is quite substantial and is solely due to the dependence of the anomalous Hall effect on ρ_{xx}^2. Thus, while the model's coercive field was kept constant, the 'measured' value changed nevertheless. This signifies why one can not use the coercive field to discuss gate dependencies of magnetic properties of materials.

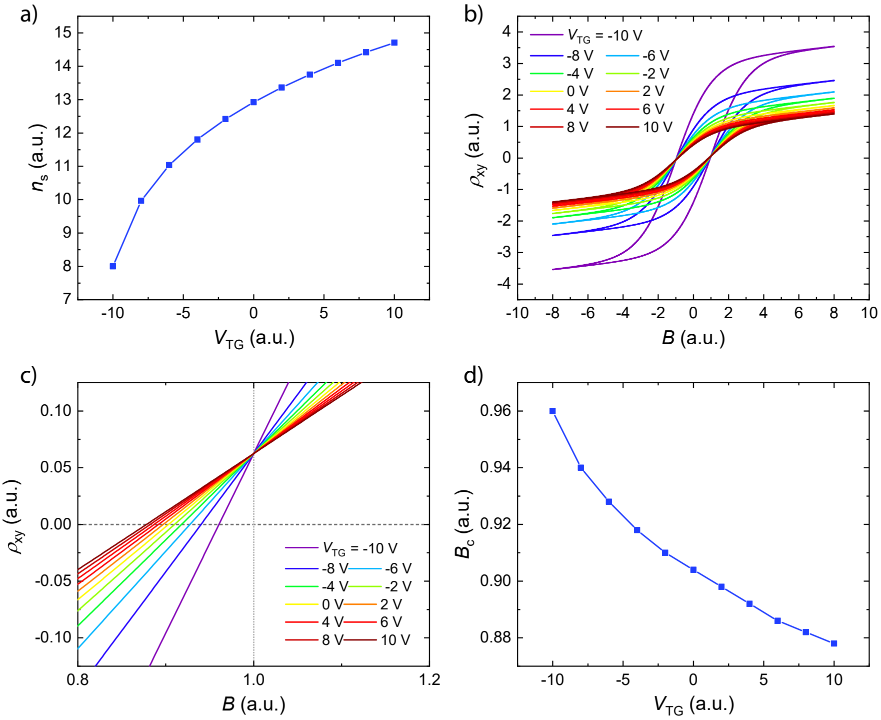

Figure A.1: Simulations of the anomalous Hall effect. **(a)** Fictitious gate dependence of the carrier density which is used as input for the model. **(b)** Magnetization loops generated by Eqn. A.1. **(c)** Zoomed in version of panel (b). **(d)** Extracted coercive field from panel (c) along the horizontal dashed line.

Appendix B: Vanadium doping with e-beam and Knudsen cell evaporators

We have evaporated vanadium from two different sources in our MBE system. We started with an e-beam evaporator, for which we noted after the first maintenance session (i.e. refill of the crucible) that the reproducibility of the samples was poor. While the high-temperature Knudsen cell has been used later and yielded more reproducible results, it remains interesting to gain understanding on why the evaporators have such different characteristics for our setup.

The vanadium used for the deposition consists of 3×3×3 mm size cubes of 99.99% vanadium, as shown in Fig. A.2(g). For e-beam evaporation,

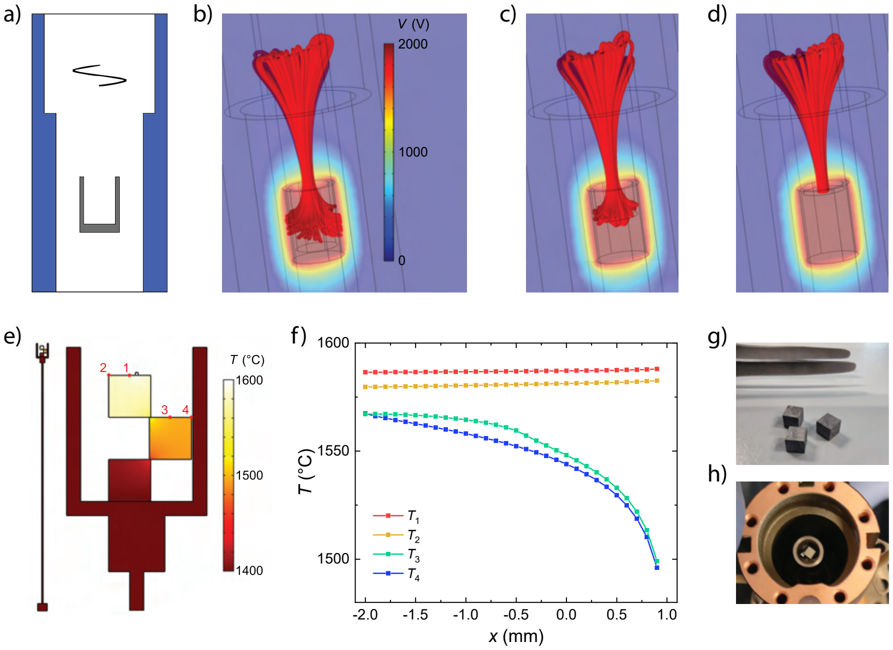

Figure A.2: COMSOL simulations of an e-beam evaporator. **(a)** Schematic overview of the crucible (gray), filament (black) and cooling shroud (blue) in an EFM 3 evaporator. **(b)** Simulated electric field (color overlay) and electric streamlines (red) for an empty crucible. **(b)** Results for a half-filled crucible. **(d)** Results for a full crucible. **(e)** Schematic overview of the temperature distribution in the crucible. **(f)** Temperature profile for the four probes in panel (e) when the middle cube is moved horizontally. **(g)** Photograph of vanadium cubes. **(h)** Photograph of a new vanadium cube in the crucible during maintenance.

we use an EFM 3 evaporator manufactured by Focus, for Knudsen cell evaporation we use a custom-built high-temperature Knudsen cell of MBE Komponenten. While a Knudsen cell heats the crucible equally, an e-beam evaporator is based on a heating mechanism where heat is generated very locally through the interactions of electrons which are accelerated towards the target material.

To get an understanding of the dynamics of a typical e-beam evaporator, we created a COMSOL simulation. The geometry of interest is shown in Fig. A.2(a). The crucible (gray) and filament (black) are surrounded by a cooling shroud (blue) which is connected to ground. The filament is heated and through thermionic emission electrons are generated. By applying a positive voltage of 2000 V to the crucible[4], the electrons will accelerate towards the material and thus generate heat in the evaporant. In our simulations, we have applied a positive voltage on the crucible and calculated the streamlines of the electric field (i.e. electron trajectories). We show the results of the simulations for cases where the crucible is empty (Fig. A.2(b)), half-filled (panel (c)) and full (panel (d)). It can be seen that the electron beam diverges within an empty crucible due to the large potential on the crucible walls, while it remains focused for an empty crucible. As such, the interaction volume within the evaporant is significantly different.

The used e-beam evaporator is equipped with a flux monitor and is thus able to regulate the supplied flux. The importance of the interaction volume remains an important topic, since the heat radiation to the substrate (already discussed briefly in Sec. 4.3) is significant for evaporation with crucibles at such high temperatures. The flux of a typical cell depends on the vapor pressure and temperature. By combining the equations for the evaporation rate of a Knudsen cell [143] and the Clausius-Clapeyron equation for the vapor pressure of vanadium [144] we find that the dependence of the evaporation rate can be approximated by $\Phi_{\mathrm{evap}} = \alpha \cdot e^{T/\beta}$ where Φ_{evap} is the flux (i.e., amount of atoms per unit area) and α and β are material-specific parameters. However, the heat radiation per unit area is given by the Stefan-Boltzmann law, $\Phi_{\mathrm{heat}} = \sigma T^4$. Since both evaporation rate and heat radiation influence the film deposition while having different dependencies on temperature, a different interaction volume (such as shown in the simulation figures) will result in a different balance between the evaporation rate and heating power. The fact that the e-beam power changes from sample to sample is an indication for this.

Another difficulty with e-beam evaporators and materials that come in large pieces is illustrated in a different situation. We note that our vanadium cubes are so large that typically only a few fit in the crucible (see Fig. A.2(h). Upon inserting new cubes we noted that the cubes typically have a small contact area with the residual vanadium in the crucible, and as such we believe that thermal gradients will appear in the evaporant. We replicated the crucible geometry in Fig. A.2(e), where the left picture shows the full crucible including the attached rod and the right image is a magnified version of the crucible only. We placed three cubes of vanadium in the crucible and placed a fictitious heat source on the top cube (small white cube) which has a fixed temperature. The crucible is connected to

---

[4] Note that the absolute value of the voltage can be chosen arbitrarily in this simulation.

the outside world at the bottom of the rod, and as such the bottom part of the rod is fixed at room temperature. We use COMSOL to calculate the heat distribution throughout the cube and monitor the temperature at four locations as indicated in the figure. Then, we move the middle cube from left to right within the image. $x = -2$ mm corresponds to the middle cube being in line with the other cubes; $x = 0.9$ mm is the other extreme case where the contact area is the smallest. The $x = 0.9$ mm situation is depicted in Fig. 4.3(e). We clearly see that the temperature of the middle cube decreases substantially when the contact area becomes less. This means that also the surface radiation, as well as evaporation, from the cube's surface will decrease. Hence, the geometry of the cubes within the crucible is also of great importance for the evaporation and radiation physics. It is important to realize that in reality the cubes are randomly oriented and thus the geometry becomes rather complex and changes after maintenance.

To summarize this section, we have performed simulations to understand why vanadium doping with an e-beam evaporator with a small crucible volume and with large cubes of vanadium was difficult in terms of reproducibility. We noted that the interaction volume influences the heat distribution, and we discussed that the temperature dependence of the heat radiation and evaporation rate is different for both cases. Furthermore, we noted that the temperature within the crucible and evaporant is not homogeneous when using solid cubes, and that this furthermore influences the cell dynamics. Of course, e-beam evaporation is widely used for a large range of materials in all kinds of shapes (cubes, powder, rod). It is therefore important to realize what is different in our case. We attribute the difficulties observed mainly to the large cube size of the vanadium. If the material was to be supplied in smaller pieces, or powder, the crucible would be filled more evenly and heat conduction will be more homogeneous too. Also, since our source does not have a scanning beam, we constantly evaporate the same part of the evaporant, rather than evenly depleting the source.

Chapter 5

The chiral magnetic effect

The field of topological materials science has recently been focusing on three-dimensional Dirac semimetals, which exhibit robust Dirac phases in the bulk. However, the absence of characteristic surface states in accidental Dirac semimetals (DSM) makes it difficult to experimentally verify claims about the topological nature using commonly used surface-sensitive techniques. The chiral magnetic effect (CME), which originates from the Weyl nodes, causes an $\boldsymbol{E}\cdot\boldsymbol{B}$*-dependent chiral charge polarization, which manifests itself as negative magnetoresistance. We exploit the extended lifetime of the chirally polarized charge and study the CME through both local and nonlocal measurements in Hall bar structures fabricated from single crystalline flakes of the DSM* $Bi_{0.97}Sb_{0.03}$*. From the nonlocal measurement results we find a chiral charge relaxation time which is over one order of magnitude larger than the Drude transport lifetime, underlining the topological nature of* $Bi_{0.97}Sb_{0.03}$*.*

The results of this chapter have been published as: de Boer & Wielens *et al.*, Nonlocal signatures of the chiral magnetic effect in the Dirac semimetal $\mathrm{Bi_{0.97}Sb_{0.03}}$, *Physical Review B* **99**, 085124 (2019).

5.1 Introduction

The electronic structure of bismuth-antimony alloys has been thoroughly studied in the 1960s and 70s and later regained attention when $\mathrm{Bi}_{1-x}\mathrm{Sb}_x$ was one of the first topological materials to be discovered [68]. It was proposed that at the topological transition point, which is at $x \sim 0.03$, an accidental band touching in the bulk of $\mathrm{Bi}_{1-x}\mathrm{Sb}_x$ makes this material a Dirac semimetal (DSM) [145–147]. A popular method to measure the topological nature of DSMs is through the detection of the chiral magnetic effect (CME) in electronic transport measurements. However, these signals are often obscured by the presence of parallel, non-topological conduction channels and are, more importantly, difficult to distinguish from other effects that may cause negative magnetoresistance, such as current jetting [53]. Parameswaran *et al.* [148] proposed to measure the CME nonlocally, using the extended lifetime of chirally polarized charge. For the Dirac semimetal $\mathrm{Cd}_3\mathrm{As}_2$, where two sets of Dirac cones with opposite chirality are separated in momentum space and protected by inversion symmetry, this measurement technique has been successfully used to measure the CME [54]. In this chapter, we present evidence for the presence of the chiral magnetic effect in the accidental Dirac semimetal $\mathrm{Bi}_{0.97}\mathrm{Sb}_{0.03}$, based on local and nonlocal magnetotransport results on crystalline, exfoliated flakes.

5.2 Dirac semimetal $\mathrm{Bi}_{1-x}\mathrm{Sb}_x$

5.2.1 The chiral magnetic effect in $\mathrm{Bi}_{1-x}\mathrm{Sb}_x$

In a general Dirac semimetal, 2 Weyl cones of opposite chirality (often labeled as isospin degree of freedom [148]) are superposed in momentum space as depicted in Fig. 5.1(a). Their chiralities are defined through an integral of the Berry connection, $A_{\mathbf{k}\pm} = i\langle\psi_\pm|\nabla_{\mathbf{k}}\psi_\pm\rangle$, over the Fermi surface (FS):

$$\chi_\pm = \frac{1}{2\pi}\oint_{FS}(\nabla_{\mathbf{k}} \times A_{\mathbf{k}\pm}) \cdot dS_{\mathbf{k}}, \tag{5.1}$$

where $\mathbf{k}$ is the wave vector. Using a basic representation of the Weyl nodes, $\psi_\pm = (e^{-i\theta}\sin(\phi/2), -\cos(\phi/2))^T$ (where θ is the in-plane angle in momentum space, with $\theta = 0$ along the k_x-axis, and ϕ is the polar angle with respect to k_z), one finds $\chi_\pm = \pm 1$. These nodes with opposite chiralities always come in pairs and, when the degeneracy of the Weyl cones is lifted, they are connected in momentum space by a surface state known as a Fermi

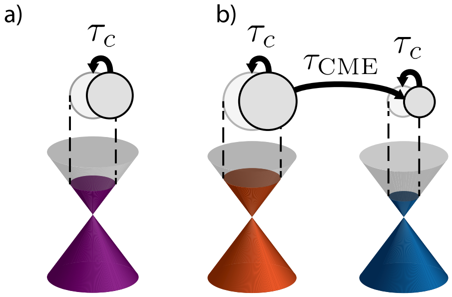

Figure 5.1: Dirac semimetals and the chiral magnetic effect. **(a)** Two superposed Weyl cones in a Dirac semimetal. In an external electric field, the electrons on a shifted Fermi surface relax to their equilibrium state with characteristic time τ_c. (**b**) In parallel external electric and magnetic fields, the two Weyl cones are separated in momentum space and exhibit different chemical potentials. Inter-cone relaxation of chirally polarized electrons occurs with characteristic time τ_{CME}.

arc. In mirror symmetry-protected Dirac systems, such as Cd_3As_2, different pairs of Weyl nodes can also be connected by Fermi arcs, which has been experimentally observed [149]. $Bi_{0.97}Sb_{0.03}$ contains accidental Dirac points at the 3 L-points [145]. A schematic overview of the Brillouin zone (BZ) of $Bi_{0.97}Sb_{0.03}$ is shown in Fig. 5.2(a) [146]. In addition to the electron pockets at the L-points (blue), a hole pocket is present at the T point (red). Furthermore, the ARPES map of the Fermi surface of the (111) surface (shown as projection above the BZ) reveals electron and hole surface states. We will use this information in fitting the magnetotransport data which we will discuss later. The crossings at these Dirac points are not protected by any symmetry, and should not be connected by Fermi arcs. However, upon breaking time reversal symmetry with an external magnetic field, the Dirac cones split into two Weyl cones of opposite chirality, in which case $Bi_{0.97}Sb_{0.03}$ behaves very similar to Cd_3As_2.

The different chiral nodes correspond to a source and drain of Berry curvature ($\Omega_{\mathbf{k}\pm} = \nabla_{\mathbf{k}} \times A_{\mathbf{k}\pm}$), which in turn behaves as a magnetic field in momentum space. Taking this momentum space analogue of the magnetic field into account in the equations of motion, one ends up with an expression for chiral charge pumping $\partial\rho_\pm/\partial t$ in external parallel electric and magnetic fields [48, 52]:

$$\frac{\partial \rho_\pm}{\partial t} = f(\Omega_{\mathbf{k}}) \frac{e^3}{4\pi^2\hbar^2} \mathbf{E} \cdot \mathbf{B}, \tag{5.2}$$

where $\mathbf{E}$ and $\mathbf{B}$ are the electric and magnetic fields respectively, and $f(\Omega_{\mathbf{k}})$

represents the chirality-dependence. The result from this semi-classical argument can also been obtained in the quantum limit [150], as was previously discussed in Sec. 2.5. This chiral charge pumping creates a difference in chemical potential in the two Weyl cones, causing a net imbalance in chirality, which eventually relaxes by means of impurity scattering. However, the orthogonality of the two degenerate Weyl cones with different isospin and the large momentum difference between different valleys suppress these relaxation processes. As a consequence, chiral charge has an increased lifetime compared to the Drude transport lifetime, which is shortened by many low-energy scattering events. Through the continuity equations, this chiral charge imbalance contributes to the longitudinal conductivity and can be observed in magnetotransport measurements [51, 145].

In $\mathrm{Cd}_3\mathrm{As}_2$, there are 2 scattering events that relax the chiral charge polarization: scattering between degenerate cones of different isospin, and intervalley scattering. Of these two, intervalley scattering should be expected to be the dominant factor as the momentum difference between the valleys is relatively small [54]. In $\mathrm{Bi}_{0.97}\mathrm{Sb}_{0.03}$, where the Dirac points reside at the 3 L-points, intervalley scattering requires a momentum transfer of the order $2\pi/a$, with a being the lattice constant. Because of this required large momentum transfer, we argue that isospin-flip scattering through multiple scattering events is the likely dominant chiral relaxation process in $\mathrm{Bi}_{0.97}\mathrm{Sb}_{0.03}$.

5.2.2 Normal transport measurements

To characterize the $\mathrm{Bi}_{0.97}\mathrm{Sb}_{0.03}$ crystals (which are grown as described by Li *et al.* [146]), several devices with contacts in a Hall bar configuration were fabricated. For all devices in this work, flakes of $\mathrm{Bi}_{0.97}\mathrm{Sb}_{0.03}$ were exfoliated from single crystals onto $\mathrm{SiO}_2/\mathrm{Si}^{++}$ substrates. Contact leads were defined using standard e-beam lithography, followed by sputter deposition of 120 nm Nb with a few nm of Pd as capping layer, and lift-off. Then, the flakes themselves were structured using another e-beam lithography step, now followed by Ar^+ milling. Magnetotransport measurements were conducted at 10 K in He-4 cryostats.

The inset of Fig. 5.2(b) shows a schematic overview of the measurement setup as used for local magnetotransport measurements. A current is sourced through the outer contacts and voltages are measured at the contacts in between. As observed earlier by Kim *et al.* [145], the magnetoresistance of $\mathrm{Bi}_{0.97}\mathrm{Sb}_{0.03}$, shown in Fig. 5.2(b), exhibits negative magne-

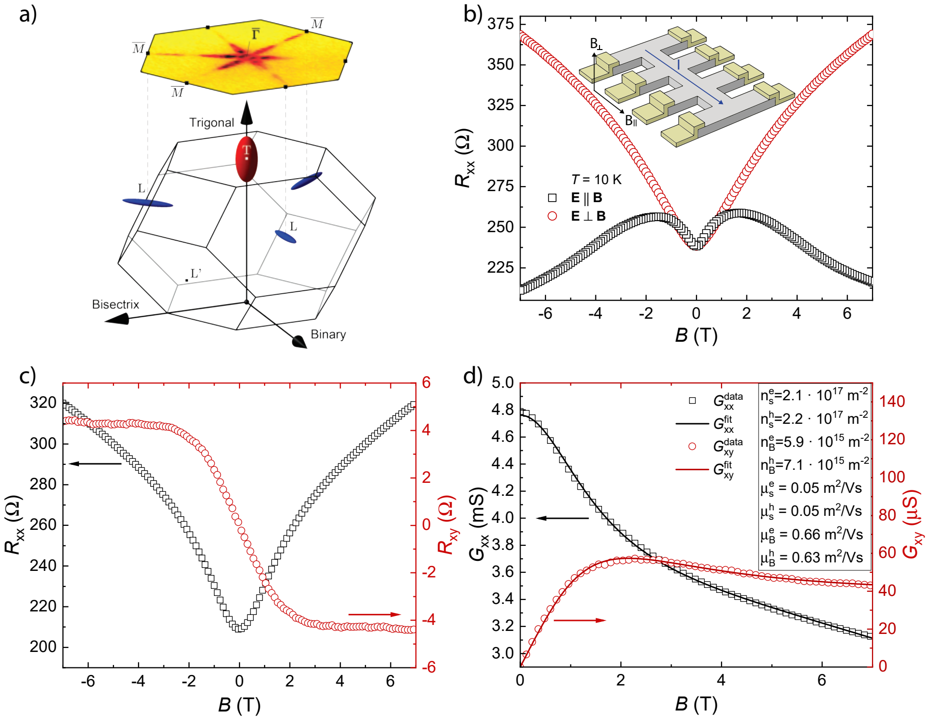

Figure 5.2: Normal transport in $\mathrm{Bi}_{0.97}\mathrm{Sb}_{0.03}$. **(a)** Schematic of the bulk Fermi surfaces of $\mathrm{Bi}_{1-x}\mathrm{Sb}_x$. Three electron pockets (blue) and a hole pocket (red) are located at the L-points and T-point, respectively. The projection onto the surface Brillouin zone is also shown, including an angle-resolved photoemission spectroscopy (ARPES) map of the Fermi surface recorded from the (111) surface for $x = 0.04$. Image taken from [146]. **(b)** Local longitudinal magnetoresistance for perpendicular and parallel electric and magnetic fields. For parallel fields, the MR is strongly negative due to the chiral magnetic effect. Inset: schematic illustration of the device used for local transport. Current is sourced through 2 of the the 4 outer leads, while the inner 4 are used as probes for the longitudinal and Hall resistances, as is typical for Hall measurements. **(c)** Results of the Hall measurement for perpendicular electric and magnetic fields. **(d)** Drude multi-band fit on the conductance. The conductances have been obtained from the measured resistances R_{xx} and R_{xy} through tensor inversion. The low mobility, high carrier density surface state contributions are based on literature [146].

toresistance for parallel electric and magnetic fields. This negative magnetoresistance is considered to be an indication of the CME [51, 145, 151, 152]. While the CME in $Bi_{0.97}Sb_{0.03}$ originates from the bulk electrons, the magnetoresistance data shows no Shubnikov-de Haas (SdH) oscillations corresponding to the bulk electron pockets, despite the low effective mass and high mobility of these electrons [153].

Fig. 5.2(c) shows the results of a Hall-type measurement. By tensor inversion of the measured longitudinal and Hall resistances, the longitudinal and transverse conductances were obtained. In Fig. 5.2(d), the conductances are fitted using a multi-band model, which takes two surface and two bulk conduction channels into account [146]. For the bulk electrons, we obtain a bulk electron density of $n_B^e = 3.0 \cdot 10^{22}$ m^{-3}, where we have used a flake thickness of 200 nm. For anisotropic Fermi velocities of $v_1 = 0.8{\cdot}10^5$ m/s and $v_2 = 10{\cdot}10^5$ m/s [68], this would indicate that the Fermi energy lies only $E_F = \hbar(\pi^2 n_B^e e v_1 v_2/3)^{1/3} = 13$ meV above the Dirac point. The bulk charge carrier mobilities as obtained from the multi-band fit are lower than those found in unstructured devices [146]. This is in line with the absence of SdH oscillations in this measurement, which can be attributed to the device dimensions being of the same order as the cyclotron radius, and to disorder due to etching at the device edges. The consequential broadening of the Landau levels does not hamper the presence of the CME [54]. For a conservative effective mass of $m_{e,h} = 0.05\, m_0$ [146], the bulk electron and hole mobilities of μ =0.65 m^2/Vs give us an estimate of the momentum relaxation time: $\tau_c = \mu m/e \approx 1.8 \cdot 10^{-13}$ s.

5.3 Nonlocal detection of the chiral magnetic effect

5.3.1 Experimental methods

The nonlocal measurement setup is designed such that we can measure the coupling between the polarization of chirality and an external magnetic field at different distances from the polarization source, and is shown in Fig. 5.3(a). A current is sourced from contact 8 to 1, as indicated by the blue arrow. By applying a magnetic field parallel to the current, a chiral charge imbalance is induced. As the charge diffuses away from the polarizing source, the polarization becomes weaker and so does the measurable voltage of the polarized charge in the external magnetic field. We measure the voltages locally ($V_L \equiv V_{81} = V_8 - V_1$) and nonlocally ($V_1 \equiv V_{72}$, $V_2 \equiv V_{63}$

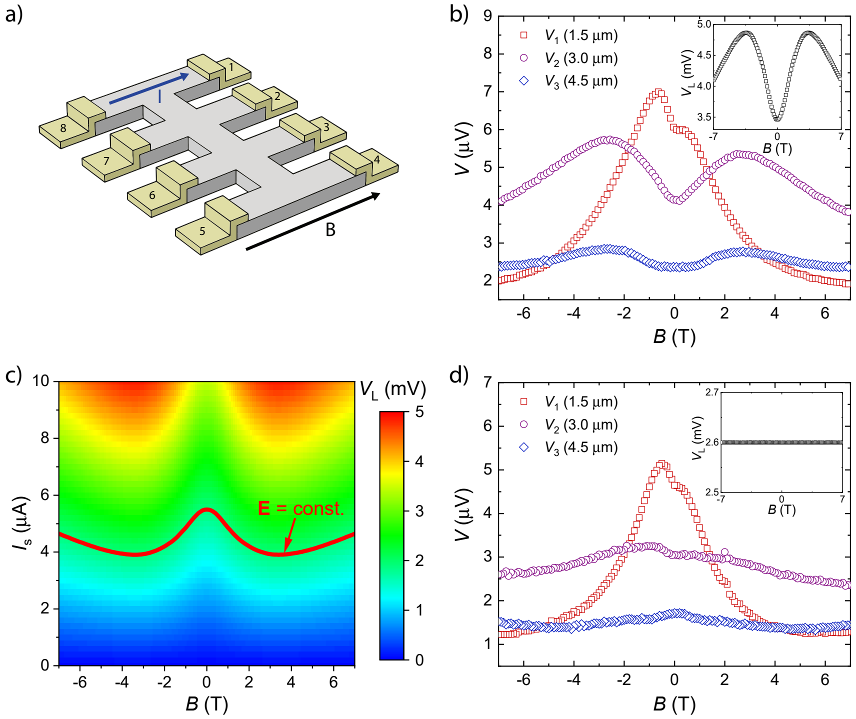

Figure 5.3: Nonlocal transport in $\mathrm{Bi_{0.97}Sb_{0.03}}$. **(a)** A schematic illustration of the device used for non-local transport measurements (gray represents the $\mathrm{Bi_{0.97}Sb_{0.03}}$ flake and yellow the metallic contacts). Current is sourced parallel to the external magnetic field, through 2 contacts on the side, and the chiral polarization that diffuses into the central channel, is measured at the contacts further along this channel. **(b)** Measured voltages at distances 1.5, 3 and 4.5 μm. A constant source current is supplied. The inset shows the local voltage, measured at the source contacts. **(c)** Local voltage measured as a function of applied current and magnetic field. The red line corresponds to a constant local voltage for varying applied magnetic fields. **(d)** Same as in panel (b), but for a varying source current $I_s(B)$ such that $V_{\mathrm{L}} = \text{const.}$ (inset)

and $V_3 \equiv V_{54}$). To be able to distinguish the Ohmic (i.e. normal diffusion) and CME signals, the voltage terminals are located at distances similar to both the expected Ohmic and chiral relaxation lengths.

When studying the CME, in the ideal case one measures the nonlocal response of the chiral anomaly as a function of the applied magnetic field only, i.e. keeping the applied electric field at the source contacts constant. However, due to the low resistance of these samples, we cannot voltage bias our sample and must resort to a current source, thereby causing the current to be constant as a function of the applied magnetic field. When measuring the local electric field, we find that this field is dependent on the magnetic field as well.

In order to obtain a data set with a constant electric field at the source contacts, measurements were performed by sweeping the source current from 0 to 10 μA for every magnetic field point, resulting in local and nonlocal magnetoresistance curves for a range of source currents $V_{\mathrm{L},1,2,3}(I_s, B)$. An example of such a set of magnetoresistance curves for a fixed source current is shown in Fig. 5.3(b). From the inset it is clear that the local voltage is not constant in magnetic field. The dependence of the local voltage on both the magnetic field and source current can be seen in figure 5.3(c). From this map, we can find a line for which $V_{\mathrm{L}}(I_s, B)$ is constant. This line is plotted on top of the map. By retracing the same line on the nonlocal voltage maps, we can extract the non-local voltages that correspond to the same constant local electric field and study the magnetic field dependence. To increase the accuracy of the maps - we measured the field dependent data for 51 different values of the excitation current - we linearly interpolated our data as a function of I_s. Although recent work on $\mathrm{Bi}_{1-x}\mathrm{Sb}_x$ suggests that Ohm's law is violated in this system [154], our generated electric field is well above the non-linear regime. In Fig. 5.3(d), we present the resulting voltages $V_{\mathrm{NL}}(I_s(B), B)$, when the local electric field is kept constant in this way. Note that the local voltage, shown in the inset of figure 5.3(d), is now constant. Using this method, the magnetic field dependence of the nonlocal signals can be studied without side effects from the local magnetoresistance.

5.3.2 Results

The measured local voltage V_{L}, presented in the inset of fig. 5.3(b), is in good agreement with the expected resistance based on the 4-point resistance, taking the size of the channels into account. This indicates that the effects of contact resistances are negligible. Fig. 5.3(d) shows the nonlocal voltages measured at different distances as a function of the applied magnetic field.

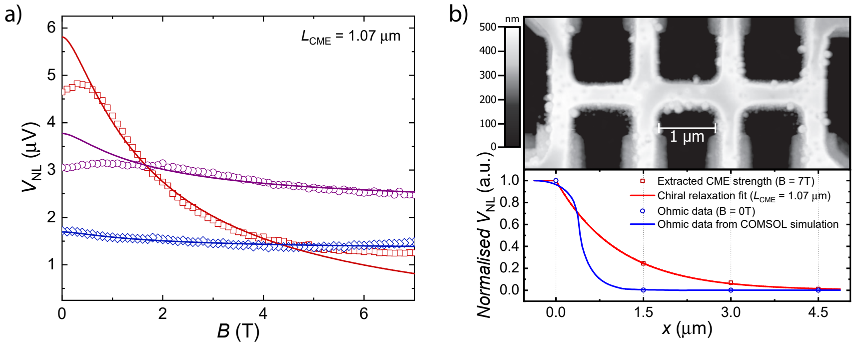

Figure 5.4: Chiral magnetic effect in $\mathrm{Bi}_{0.97}\mathrm{Sb}_{0.03}$. **(a)** Symmetrized nonlocal voltages of Fig. 5.3(d), measured at 1.5, 3 and 4.5 μm. The dark, solid lines are fits with Eqn. 5.3. **(b)** Upper panel: Atomic force microscopy image of a $\mathrm{Bi}_{0.97}\mathrm{Sb}_{0.03}$ single crystal flake, structured into a device for non-local measurements and contacted with Nb leads. Lower panel: Normalized strength of the Ohmic (zero field) and CME (from fit) contributions to the signals measured at the voltage probes. The CME strength persists over longer distances than the Ohmic signal.

Here, the electric field at the source side is kept constant. At zero magnetic field, the measured voltages drop with increasing distance from the source. Furthermore, at all distances we observe a decreasing voltage with increasing magnetic field, which we attribute to the CME. The CME is not dominant for the entire magnetic field range as both at low and high fields, the voltage increases slightly with magnetic field. Kim *et al.* attribute the low field MR to weak anti-localization [145]. High field deviations from the CME signal may originate from higher order terms, which are not taken into account in this work.

We have identified three possible causes of the small asymmetry of the data. First and foremost is the device asymmetry with respect to the source channel, but variations in sample thickness and imperfections in the structuring process may also be contributing factors. Fig. 5.4(a) shows the symmetrized nonlocal voltages. We fitted the intermediate field data between 2 T and 5.5 T with a model that subtracts the constant Ohmic contribution, and extracts the diffusion of the chiral charge as given by Parameswaran *et al.* [148]:

$$V_{\mathrm{NL}}(x) = -\left(\frac{B}{\gamma + B}\right)^2 e^{-|x|/L_{\mathrm{CME}}} + V_{\mathrm{Ohmic}}. \tag{5.3}$$

Here x is the distance between the source and the nonlocal probes, γ is pro-

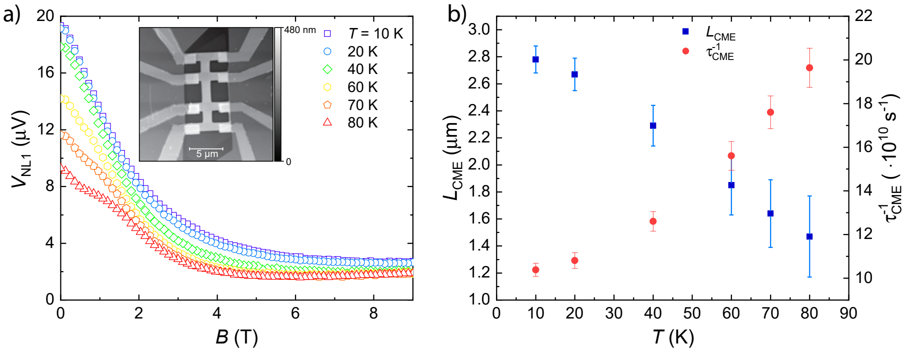

Figure 5.5: Temperature dependence of the chiral magnetic effect. **(a)** Temperature dependence of a different device. We plot the voltage at the non-local contact closest to the source. The inset shows the AFM image of the device used for these measurements. **(b)** Temperature dependence of the chiral charge diffusion length L_{CME} and the chiral polarization lifetime τ_{CME} as extracted through Eqn. 5.3.

portional to the conductance at the metal contact and L_{CME} is the diffusion length of the chiral charge polarization. The fit agrees well with the data for intermediate magnetic fields and it gives a diffusion length of 1.07 μm. Using $L_{\mathrm{CME}} = \sqrt{D\,\tau_{\mathrm{CME}}}$ and $D = (1/3)\,v_F\,l_m$, with $l_m = v_F\,\tau_{\mathrm{CME}}$, we find a chiral polarization lifetime of $\tau_{\mathrm{CME}} \approx 3.7 \cdot 10^{-12}$ s, which is over one order of magnitude longer than the Drude transport lifetime $\tau_c \approx 1.4 \cdot 10^{-13}$ s.

The dependence of the normalized Ohmic and CME contributions to the measured voltages is presented in Fig. 5.4(b), along with an atomic force microscopy (AFM) image of the device. Here, the amplitudes of the best fits are used to represent the CME strength. The measured Ohmic (zero-field) contribution at all voltage terminals is shown for comparison. The Ohmic contribution of the device is also modeled numerically, where the shown solid curve is a line cut along the horizontal part of the device (see Appendix). The simulated Ohmic contributions fit very well to the measured data, emphasizing the good homogeneity of the flake. The most notable feature of Fig. 5.4(b) is that the chiral polarization of the charge carriers has a significantly longer relaxation length than the Drude transport lifetime.

To study the temperature dependence of the CME in $\mathrm{Bi}_{0.97}\mathrm{Sb}_{0.03}$, another device was measured at higher temperatures. This device has larger channel widths and spacing as can be seen in the AFM image of the device in the inset of Fig. 5.5(a). We should note that all voltages were measured only at one value for the source current, in contrast to the voltages measured of both source current and magnetic field that were used for the other device. However, because of the linearity of the voltage as a function of source current, we justify our method of interpolating the a linear fit between the voltage at a given current and the origin (zero voltage at zero current), which generates the $V_L(I_s, B)$ map which then can be used to extract a constant local voltage and accordingly trace the nonlocal voltage maps. Fig. 5.5(a) itself shows the measured voltages at the nonlocal contacts closest to the source, which present the most striking features. It is apparent that for all temperatures displayed in this figure, the magnetoresistance is strongly negative and that this nonlocal voltage decreases as temperature increases. Through the same fitting procedure described above, the chiral charge polarization diffusion length is extracted for each temperature and shown in Fig. 5.5(b). In contrast to what has been found for $\mathrm{Cd_3As_2}$ [54], the chiral diffusion length in $\mathrm{Bi_{0.97}Sb_{0.03}}$ does not seem to be constant with increasing temperature, but rather decreases linearly. The increasing relaxation rate τ_{CME}^{-1} with increasing temperature, indicates that inelastic processes are responsible for the relaxation of the chiral polarization in $\mathrm{Bi_{0.97}Sb_{0.03}}$.

5.4 Conclusions

In this chapter, we studied the chiral magnetic effect in $\mathrm{Bi_{0.97}Sb_{0.03}}$ through transport measurements in local and nonlocal configurations. First, we characterized the exfoliated crystalline $\mathrm{Bi_{0.97}Sb_{0.03}}$ flakes using a Hall-type measurement. Here, we identified contributions from two bulk bands, one of them corresponding to the electron pockets with a linear dispersion and a Fermi level close to the Dirac point. When subjected to parallel electric and magnetic fields, local measurements on our $\mathrm{Bi_{0.97}Sb_{0.03}}$ devices show a pronounced negative magnetoresistance, an indication of the chiral magnetic effect.

In a nonlocal configuration, we measured voltages that strongly decrease with increasing magnetic field, which we attribute to the chiral magnetic effect. As voltage contacts are located further away from the polarization source, the measured chiral magnetic effect weakens. This weakening occurs at a much lower rate than the decay of the Ohmic signal, which is a consequence of the long lifetime of the chiral polarization τ_{CME}. Furthermore, measurements at different temperatures show that the chiral charge diffusion length decreases with increasing temperature, emphasizing the role of inelastic scattering in the chiral charge relaxation process in $\mathrm{Bi_{0.97}Sb_{0.03}}$.

Both local and nonlocal measurements provide strong evidence of the presence of the chiral magnetic effect in the three-dimensional Dirac semimetal $Bi_{0.97}Sb_{0.03}$.

Appendix: Modeling the Ohmic contribution

The measured data comprises a combination of a chiral signal and a normal, i.e. Ohmic, contribution. To gain better insight in the Ohmic contribution, we modeled this contribution in COMSOL Multiphysics. The device geometry used for the measurements was replicated in COMSOL. One of the source leads was defined as a current source, sourcing 1 μA, while the other current lead was set as ground. The other terminals were voltage probes.

For simulations with perpendicular electric and magnetic fields (i.e. B in the z-direction and I in the x-direction), the three-dimensional conductivity tensor for a single band can be obtained from the Drude model;

$$\hat{\sigma_\perp} = \sigma_0 \begin{pmatrix} \frac{1}{1+(\mu B)^2} & \frac{\mu B}{1+(\mu B)^2} & 0 \\ -\frac{\mu B}{1+(\mu B)^2} & \frac{1}{1+(\mu B)^2} & 0 \\ 0 & 0 & 1 \end{pmatrix}, \tag{A.4}$$

where $\sigma_0 = ne\mu$. For parallel electric and magnetic fields (i.e. B in the x-direction), one can show that the conductivity tensor is given by

$$\hat{\sigma_\parallel} = \sigma_0 \begin{pmatrix} 1 & 0 & 0 \\ 0 & \frac{1}{1+(\mu B)^2} & \frac{\mu B}{1+(\mu B)^2} \\ 0 & -\frac{\mu B}{1+(\mu B)^2} & \frac{1}{1+(\mu B)^2} \end{pmatrix}. \tag{A.5}$$

Upon changing the tensor in COMSOL we effectively rotate the magnetic field with respect to the sample. We have investigated different structures (depicted as insets within the figures) and different orientations of the magnetic field with respect to the electric field. For every simulation we used a carrier density of $n = 4 \cdot 10^{17}$ m^{-2} and mobility $\mu = 2$ m^2/Vs.

Fig. A.1(a) shows the simulation results for a magnetic field perpendicular to the plane (and thus to the current). The sample is shaped into a non-local structure with a geometry as used in the experiments. We observe decreasing non-local voltages at the nearest contact with increasing perpendicular magnetic field. As the used model only captures the Drude conductivity, the observed decrease cannot be explained by a chiral component. The contacts further away from the source all returned negligibly small voltages. Fig. A.1(b) shows the experimentally measured data of the sample of Fig. 5.4 in perpendicular electric and magnetic fields. The first nonlocal voltage, V_1, decreases for larger magnetic fields, while the chiral magnetic effect is not present. To further investigate the nature of this decrease, simulations were performed on a rectangular, unstructured flake

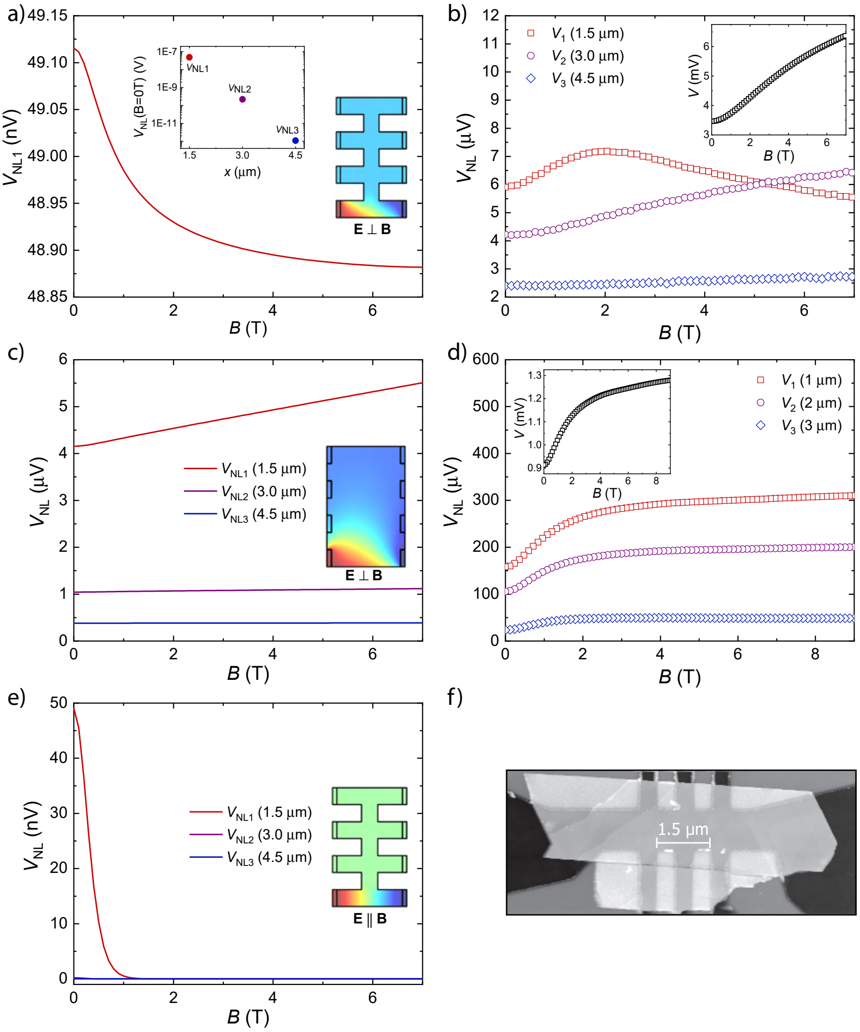

Figure A.1: Modeling the Ohmic contribution. For the simulations in panels (a,c,e), the device schematics show a contour plot of the voltage distribution for $B = 1$ T. The experimental data of panels (b,d) are measured at a constant source current. **(a)** Simulation results for a structured device in perpendicular magnetic fields. **(b)** Magnetoresistance data measured for the nonlocal device of Fig. 5.4(b), in perpendicular magnetic fields. Inset: voltage at the source contacts. **(c)** Same simulation as in panel (a), but for a non-structured device in perpendicular magnetic fields. **(d)** Magnetoresistance measured for the nonlocal device of panel (f) in perpendicular magnetic fields. **(e)** Same as panel (a), but for magnetic fields parallel to the source voltage. **(f)** AFM image of the unstructured device used for the simulations and measurements.

with 8 contacts, as shown in figure. A.1(c), in order to see whether the device geometry influences the nonlocal voltages for perpendicular fields. The nonlocal voltages now show an upturn with increasing parallel magnetic field. By comparing panels (a) and (c), which make use of the same conductivity tensor and only differ in terms of geometry, we conclude that the decreasing non-local voltage in panel (a) is caused by the geometry of the device. The simulations are much more distinctive on the two different geometries, because the simulations take only a single band into account for the conductivity, while in reality the conductivity is mediated by four channels. Furthermore, as can be seen from panel (f), the flakes are not always uniform in thickness and are not as well defined as the geometries in our simulations.

Figure A.1(e) shows the nonlocal voltages for magnetic fields parallel to the electric source field. The strongly decreasing magnetoresistance can be explained by an effect called current jetting. Current jetting, as follows from the conductivity tensor for parallel fields, is an effect where the magnetic field suppresses current flow in the transverse direction [155, 156]. This reduces the amount of current that spreads out towards the non-local voltage probes, resulting in a decrease in the voltages that are measured. The fact that current jetting can also introduce negative magnetoresistance, is (among other effects) one of the main reasons that observing negative magnetoresistance itself is not a proof of observing the chiral anomaly. However, the simulated nonlocal voltages decrease (even vanish) much faster than observed in experiments. From this, we conclude that the negative magnetoresistance in our samples is not caused by current jetting.

Chapter 6

Flux detection of gate tunable magnetic topological insulator devices in a dilution refrigerator

The observation of the 'image magnetic monopole' arising from topological surface states when an electric charge is placed above the surface of the topological insulator requires extremely sensitive magnetic sensors in combination with extremely low temperatures. In this chapter, we report our findings of experiments where a superconducting quantum interference device (SQUID) was integrated in a dilution refrigerator in a flip-chip configuration. We use devices with top gates to explore the magnetization of magnetic topological insulator thin films as a function of the gate voltage. We find that the excellent sensitivity of the SQUID and the temperature dependence of the magnetization of the magnetic topological insulator thin film require a thorough analysis to reveal the intricate interplay between heat dissipation and observed SQUID signals.

6.1 Introduction

In Chapter 2 we have discussed the different experiments that could probe axion electrodynamics in topological matter. Here, we focus on the experiment that was originally proposed by Qi *et al.* [24] where a magnetic topological insulator (MTI) would generate a magnetic field in response to an electric field. When the electric field is generated by a single point charge, the magnetic fieldlines emerging from the MTI surface will look like a magnetic monopole that resides in the MTI film. We have seen in Sec. 2.3 that the concept of placing an electric charge above the MTI, experimentally difficult to realize, can be extended to using a top gate to induce charges over a larger area, which still leads to an in plane electric field at the surface of the MTI, ultimately leading to a circulating current which generates the magnetic response.

The realization of the magnetoelectric effect in MTIs requires an experimental setup capable of magnetizing the films, which can have substantial coercive fields at low temperature. Furthermore, it should be able to provide a temperature that is low enough for films to develop the QAH state or axion insulator state. The combination of high magnetic fields and low temperatures can be realized by performing measurements in a dilution refrigerator. Because of the large amount of measurement lines, SQUID measurements and transport measurements can be combined, leading to a unique combination of measurement techniques at extreme conditions.

In this chapter, we combine the MTI films of Chapter 4 and the experimental proposal of Chapter 2 to fabricate top gate devices for the SQUID experiments. We perform measurements in a dilution refrigerator equipped with a ‘flip-chip’ SQUID chip on devices with circular top gates, as well as on top gated Hall bar devices. We use the SQUID to measure the response of the sample upon changing the gate voltage and changing the source current, and we perform magnetotransport data on the same devices at elevated temperatures. We combine the data gathered of both the circular top gate devices and Hall bar devices to discuss the nature of the observed features.

6.2 Experimental aspects

We use the MTI films of Chapter 4 and the fabrication process of Chapter 3 to fabricate top gated MTI films. Here, we distinguish two types of samples. Firstly, we use devices with a circular top gate electrode. We will refer to this device type as the ‘axion device’. An optical photo of such a device

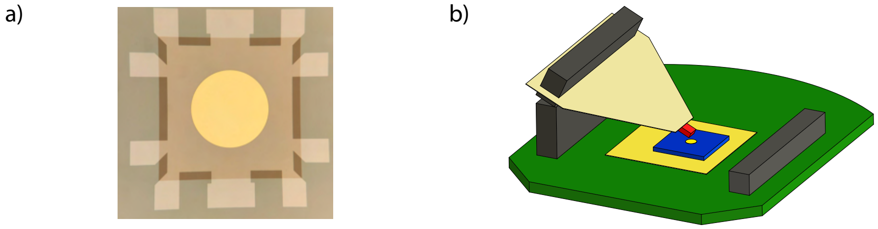

Figure 6.1: Experimental aspects. **(a)** Optical image of the axion device. The MTI (light beige) is structured into a square with current leads and voltage probes. The top gate consists of a square Al_2O_3 layer (brown) followed by a circular Au electrode (yellow). The circular electrode has a radius of 500 μm. **(b)** Flip-chip configuration. The sample (blue chip with yellow gate electrode) is placed on a standard PCB. The SQUID (red) is glued and bonded on a separate PCB (beige) which is mounted upside down to the sample PCB through the header connections (dark grey) at the left side.

is shown in Fig. 6.1(a). The film (light beige) is structured such that it has several terminals, so that transport measurements can be performed. We should note however that this geometry is far from ideal for accurate magnetotransport measurements. The film is covered with a square patch of a 30 nm thick Al_2O_3 dielectric (brown), deposited by atomic layer deposition (ALD). Finally, a circular Au gate electrode (yellow) is deposited on top of the gate oxide. The circular shape is chosen to minimize distortions in the generated electric field, and, if present by the magnetoelectric effect, the resulting magnetic field. The electrode has a radius of 500 μm (for a discussion on the size, see Appendix A). The sample is wirebonded by hand by using Au wires and silver paste. By placing the wire on top of the gate, we ensure that the edge of the gate is not disturbed by any leads, which could hamper the generated magnetic field from the circulating surface current.

Secondly, a top gated Hall bar (referred to as ‘Hall bar device’) is fabricated with the same process steps as for the axion device. Here, the film is shaped into a standard Hall bar and care is taken to make sure that the gate affects the entire area between the voltage probes to ensure proper magnetotransport measurements. However, this geometry is less suited for magnetoelectric measurements as the edge of the Au electrode is outside of the current channel and hence does not lead to an in-plane electric field at the edge of the MTI film.

The sample is bonded to a custom printed circuit board (PCB) which allows for a second PCB to be connected upside down (‘flip-chip’ configuration) to the sample board. A schematic overview of the PCBs is shown in Fig. 6.1(b). The sample (blue chip) is glued to the sample board's (green) contact area (yellow), which is an Au plated square patch with thermal vias to the backside of the sample holder to allow for good thermal contact between the sample and mixing chamber of the refrigerator. The flip-chip PCB (beige) is a thin but rigid PCB that holds the SQUID sensor (red). The SQUID sensor used here is a low temperature Nb/SiO$_x$/Nb SQUID[1], fabricated externally, per custom design, by 'ez SQUID'. It features an extended pickup loop with an area of $\sim$ 10 μm^2 [38]. The pickup loop is separated from the SQUID loop by 800 μm by lines which are magnetically shielded. Additionally, a modulation loop is included on the chip which allows the SQUID to be used in a flux-locked loop. More details on the flux-locked loop operation can be found in Ref. [38, 158]. The SQUID connections are transferred to the sample PCB through the headers (dark gray). The ground plane on both surfaces of the SQUID PCB is connected through the remaining headers to the sample PCB ground which allows for (extra) cooling of the SQUID PCB.

The sample PCB is loaded in an Oxford Triton 200 dilution refrigerator with a base temperature of 20 mK, equipped with an 8 T superconducting solenoid magnet. A dilution refrigerator is chosen because of several practical reasons. Firstly, the QAH / axion insulator samples require ultra-low temperatures which are only reachable in a dilution refrigerator. Secondly, the films should be magnetized by magnetic fields above 1 T. Lastly, the wiring inside the Triton system allows for simultaneous transport and gate tuning during SQUID measurements.

The SQUID wiring in the dilution refrigerator has been modified by thermally anchoring the modulation signal lines (semi-rigid lines) to the cold plate first, which reduces the heat load[2] on the mixing chamber plate significantly. Outside of the Triton, the SQUID wires are separated from the rest of the dc wiring and are used to connect the SQUID to the commercially available PFL-100 programmable feedback loop controller and PCS100 control interface of STAR Cryoelectronics. The radiation shield of the puck has been replaced by a custom aluminium shield, which, when superconducting, acts as a shield for external magnetic fields. While the SQUID and aluminium shield are installed in the system, magnetotransport measurements are only conducted above the critical temperature of Nb to prevent flux trapping in the SQUID.

---

[1] Note that the T_c of Nb is $\sim$ 9 K.

[2] The modulation signal typically used during SQUID operation is 85 μA.

The sample is biased with a combination of dc and ac currents and the responses are measured by standard multimeters and lock-in amplifiers. The SQUID voltage is monitored continuously and when flux jumps are detected a custom Arduino setup will immediately reset the SQUID, which allows us to measure for days without interruptions. Flux jumps present in the SQUID voltage data set span only a single data point per jump, which we remove afterwards by replacing the data point by the average of the nearest data points in time.

6.3 Proof of principle: test wire

To verify the successful integration of the SQUID within the Triton dilution refrigerator, test experiments were performed. The test sample consisted of an Al_2O_3 substrate over which an Au bond wire ($d = 25\ \mu$m) was stretched. The substrate makes sure that the wire does not make contact to the ground plane of the PCB, while it also brings the wire up to the height similar to a device on a chip.

Prior to the measurements, the SQUID sensor was tuned by means of the programmable feedback loop of the SQUID electronics. Tuning the SQUID also sets the output voltage to zero. It is therefore important to remember that the SQUID output is always relative to the conditions in which the sensor was tuned. The experiment was performed twice: once with the standard radiation shield and once with the aluminium shield. The noise level of the SQUID was found to be 70 $\mu\Phi_0/\sqrt{\text{Hz}}$ for both cases, indicating that it is mainly caused by the dilution refrigerator itself. Bringing strong magnets in the vicinity of the cryostat led to noticeable changes in the SQUID voltage when the standard shield was used, but did not change the SQUID voltage at all when the aluminium shield was used, hence verifying that the aluminium shield is acting as a magnetic shield.

We now return to the Au wire. Magnetostatics tells us that the magnetic field at a distance s of a wire carrying a current I is given by

$$B = \frac{\mu_0 I}{2\pi s}. \tag{6.1}$$

Since our SQUID is operating at a fixed position, the flux passing through the sensor is directly proportional to the magnetic field and thus also directly proportional to the applied current I. To measure the response of the SQUID to the magnetic field of the wire, the current was swept many times from positive to negative values. By averaging the sweeps we were able to

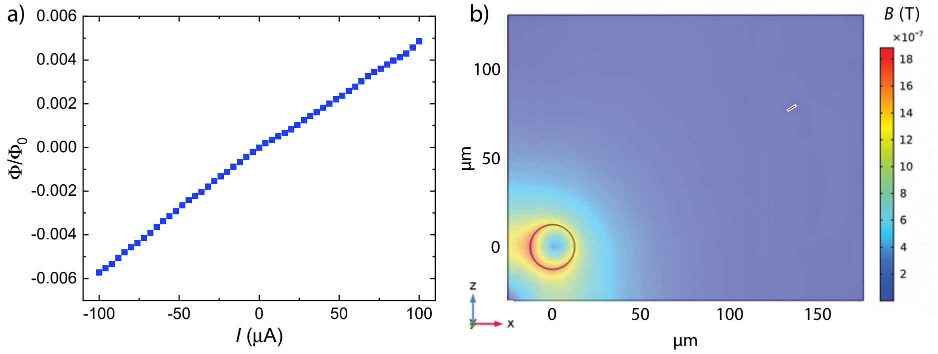

Figure 6.2: Proof of principle results. **(a)** SQUID response as a function of the applied current through the test wire. **(b)** Side view results of the COMSOL simulation. The SQUID pickup loop (top right feature, outlined in white) is displaced horizontally and vertically by values obtained from pictures acquired moments before closing and loading the Triton puck. The wire (bottom left) generates a circulating field around it. Distortions of the field near the bottom left corner are due to the finite size of the simulated volume.

improve the signal-to-noise ratio (SNR) significantly. We then convert the voltage into flux by using the voltage to flux ratio, and we choose a suitable offset. For our test wire, we chose $\Phi/\Phi_0 = 0$ when $I_{\text{wire}} = 0$.

Fig. 6.2(a) shows the measurement results of our test wire. For a current of 100 μA, the resulting flux through the SQUID sensor is $\sim 5 \cdot 10^{-3}$ Φ/Φ_0. Here, the bias current was swept up and down over 50 times to improve the SNR. During the measurements the temperature of the mixing chamber increased from base temperature to 70 mK, but this had no effect on the individual measurement sweeps. To compare the acquired data with a simulation of the setup, photographs were taken of the sample and SQUID PCB before loading them into the Triton system. COMSOL simulations were built, in which we used estimations of the distance from SQUID to sample (both horizontally and vertically) based on the photographs. We used a horizontal shift of $\sim$ 135 μm and a vertical distance of $\sim$ 65 μm. By using the effective area of the pickup loop and the sourced current of 100 μA, we were then able to model the amount of flux passing through the pickup loop. A side view of the simulated geometry is shown in Fig. 6.2(b). The flux passing through the pickup loop was found to be $1.6 \cdot 10^{-4}$ Φ/Φ_0; 50 times smaller than the measured value. The measured value can be larger because of several reasons. Firstly, the SQUID consists of a pickup loop which ultimately is connected to the larger SQUID loop. Because the magnetic field of the wire decays with $1/r$, a non-zero contribution can also be measured through the large loop itself. A rough estimate shows that the large loop can capture a similar amount of flux compared to the pickup loop[3]. However, this does not explain a difference of a factor 50. Another possible, and more likely cause, is that thermal stress upon cooling down the PCBs can alter the distance of between SQUID and sample. While in general the SQUID PCB could bend towards or away from the sample, it is most likely that the effective measurement distance is decreased.

6.4 SQUID measurements on MTI samples

We now turn to the measurement data of the MTI samples. Two samples will be discussed: one of the axion device type, and one top gated Hall bar device[4]. The extensive data sets of both samples show very similar trends, and we therefore choose to present the data of both samples at once. We divide our data sets in three different sets. After cooling down the sample, initial experiments are performed prior to magnetizing the film by the external magnetic field. This first set of measurements is referred to as zero-field-cooled (ZFC). We then heat the sample to 9.5 K, ramp the magnetic field to a value for which the magnetization is fully saturated, then ramp back the field to zero (leaving the sample at its remnant magnetization) and then cool down the sample to base temperature. We should note that a temperature of 9.5 K is too high for the film to remain fully magnetized, but because of limitations of both SQUID (T_c of Nb ~ 9 K) and aluminium shield we have to use such a high temperature. For more details on the magnetization process, see Appendix B. When the external magnetic field during this procedure was positive, we refer to the sample as being magnetized positively, while a negative external field results in a negatively magnetized sample. The data sets for positive and negative magnetization form the second and third data set, next to the non-magnetized state.

---

[3] Of course, this only holds for the magnetic field of a wire which decays as $1/r$. For typical SQUID measurements, concerning dipoles, the field decays as $1/r^3$ [38]. Hence, the measured flux is dominated by the pickup loop.

[4] The device shown in the optical image in Fig. 3.4 is in fact the particular device that we discuss in this chapter.

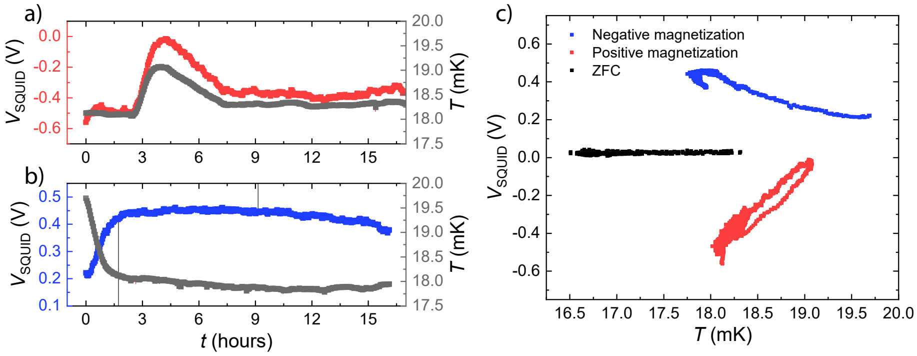

Figure 6.3: SQUID voltages for changing mixing chamber temperatures. **(a)** SQUID voltage and mixing chamber temperature as a function of time for a positively magnetized axion device. **(b)** Same as panel (a), but for a negatively magnetized film. The spikes correspond to flux jumps. Their absence in panel (a) and few occurrences in panel (b) show that they hardly occur, which justifies our procedure of removing them without altering the overall measurements. **(c)** The SQUID voltages of panels (a-b) are plotted as a function of temperature. In addition, the ZFC data set is also included.

6.4.1 Measurement procedure: background trend

To measure the response of the devices to changes in top gate voltage, we sweep the gate voltage up and down many times (typically over 50 times) while constantly recording the SQUID voltage, mixing chamber temperature and (for the Hall bar sample) ac and dc transport data. In Fig. 6.3(a-b) we show the SQUID voltage and mixing chamber temperature as a function of time, recorded while sweeping the gate up and down many times, measured on the axion device. Panel (a) corresponds to the film being positively magnetized, while panel (b) corresponds to the negative magnetization. The data is processed similarly to the test data. After taking care of the flux jumps (see Sec. 6.2) we average the gate sweeps into a single sweep. As we sweep and record both up and down sweeps of the gate voltage, we then combine the two sweep directions into a single graph. Finally, we convert the SQUID voltage into flux.

Before we discuss the processed data, it is important to understand the observed trends in the data of Fig. 6.3(a-b). For positive magnetization (panel (a)) we see that the SQUID voltage directly follows the temperature of the mixing chamber. The small ripple observed on top of the SQUID voltage is due to sweeping the top gate. In panel (b), we plot the SQUID

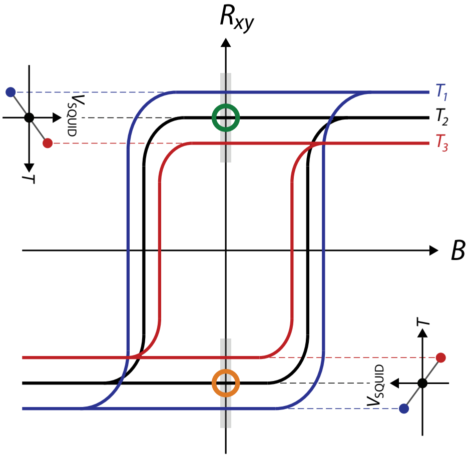

Figure 6.4: Schematic overview of the model to explain the measured temperature dependence in the SQUID measurements. We consider the case where the system has been polarized by the external magnetic field, after which the system is cooled to temperature T_2. At this temperature, the SQUID is tuned, so that for positive magnetization, $V_{\mathrm{SQUID}} = 0$ at the green circle, while for negative magnetization the SQUID voltage is zero at the orange circle. When the temperature is increased, the SQUID voltage increases for a positive magnetization, while the voltage decreases for a negative magnetization, as shown in the inset graphs. Within the hysteresis loop, the SQUID can only operate within one of the two grey boxes, since temperature can be varied, but the external field can not be varied because of the aluminium radiation shield of the puck.

voltage and mixing chamber temperature for the case where the sample is magnetized negatively. Here, an increasing temperature leads to a decreasing SQUID voltage. In Fig. 6.3(c), we plot the same data sets, but now as a function of temperature instead of time. In addition, we also show the ZFC data set, which does not show any dependence on temperature. It is clear that a relation between SQUID voltage and magnetization is present. We consider a simple model to discuss this relationship in more detail.

We base our model on the schematic overview of Fig. 6.4. Magnetotransport measurements (such as presented in Chapter 4) and SQUID magnetometer measurements [112] have shown that the saturation magnetization M_s and remnant magnetization M_r (both to be measured indirectly through the transverse resistance R_{xy}) decrease when the temperature is increased. After magnetizing the film to a positive (negative) magnetization, the SQUID is tuned, such that its voltage is zero. Within the depicted hysteresis loop, we are now at the green (orange) circle. When the temperature is increased, the decreasing magnetization will lead to a positive (negative) voltage, compared to its initial state[5]. This is in direct correspondence with the data shown in Fig. 6.3. Note that it also captures the flat line for the case of no magnetization, since the absence of magnetization means that the SQUID voltage will not change with temperature[6].

6.4.2 Dependence on top gate voltage and bias current

We now turn our attention to the processed data. Top gate sweeps were performed both without applied bias current (i.e. no transport through the sample) and with applied bias current. Surprisingly, a clear distinction between the two was found. While for applied bias currents a clear trend in $\Phi(V_{\mathrm{TG}})$ was observed, this trend was absent for no applied bias current. If the change in flux would be induced by the topological magnetoelectric effect, we would expect it to be present irrespective of the applied bias current. On the other hand, the absence of a change in flux is expected for the Van Vleck magnetism that was observed in this film (as discussed in Chapter 4), since this type of magnetism is independent of the carrier density, but this would also be independent of the applied bias current. To investigate the difference between biased and unbiased top gate sweeps in more detail, we repeated the measurements for a range of bias current values. In Fig. 6.5(a), we plot the flux as a function of gate voltage for the positively magnetized axion device. We have set $\Phi(V_{\mathrm{TG}} = 8\ \mathrm{V}) = 0$ for every curve. While for low bias currents there is no visible trend, for larger bias currents we see that the flux decreases when the gate voltage is increased. In Fig. 6.5(b), we plot the results of the negatively magnetized top gated Hall bar device for different bias currents. Here, we observe an increasing flux when the gate voltage is increased, opposite to the positively magnetized film of Fig. 6.5(a). The strength of the SQUID response of panel (b) is smaller than the one of panel (a). Possible explanations for the difference in signal strength are the film area (i.e. the amount of magnetic

---

[5] Remember that the output of the SQUID is a relative quantity with respect to its initial conditions, which were set to zero at T_2.

[6] We only consider data < 30 mK here, for which the SQUID characteristics do not change as a function of temperature. When operated at temperatures closer to the T_c of the SQUID, the critical current will be temperature dependent and the SQUID output will change. In fact, this temperature dependence is used in thermal SQUID-on-tip (SOT) devices [157].

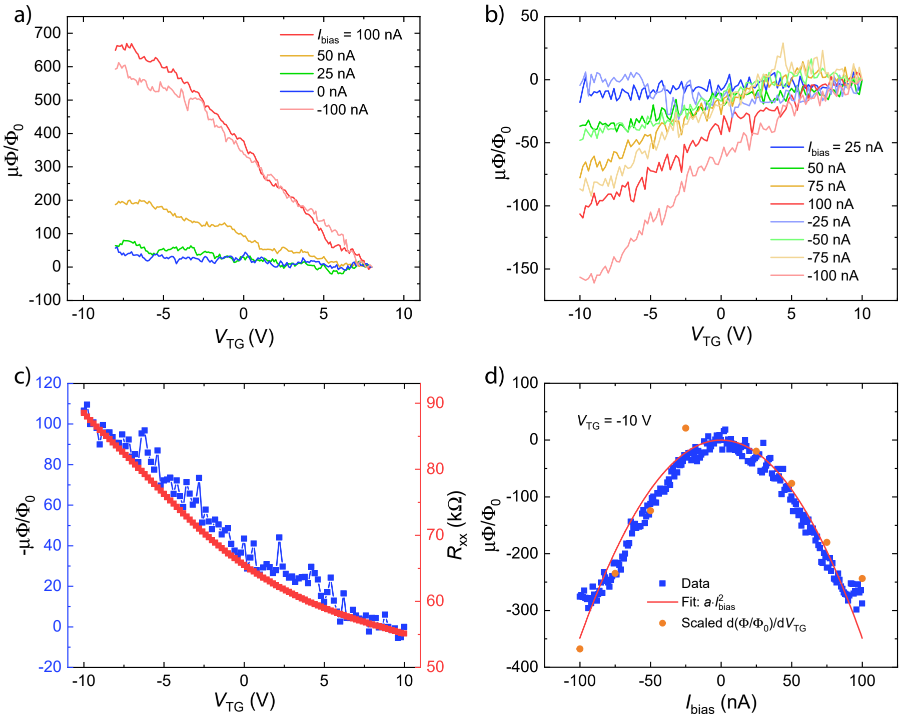

Figure 6.5: Processed data of top gate sweeps on MTI devices. **(a)** The measured flux for different values of the bias current for the positively magnetized axion device. The flux at V_{TG}= 8 V is set to zero for all curves. The strength (i.e. slope) of the signal increases with increasing bias current. **(b)** The measured flux for the negatively magnetized Hall bar device. The flux at V_{TG}= 10 V is set to zero. **(c)** Comparison between the measured flux at a bias current of 100 nA (blue) and the longitudinal resistance measured in the same data set (red). A minus sign was added to the flux to match the slope of the voltage data. **(d)** Processed data of bias current sweeps on the top gated Hall bar device being magnetized negatively. The data (blue) is fitted by the current squared (red line). In addition, the strength of each sweep of panel (b), i.e. $d(\Phi/\Phi_0)/dV_{\mathrm{TG}}$, is shown on top of the data (orange dots) after scaling the strength accordingly. Its shape is in agreement with the direct measurements presented in blue.

material), as the axion device is much larger than the Hall bar device, and variations in SQUID to sample distance, which varies from sample to sample. The data in panel (b) shows more clearly that the strength of the SQUID signal, i.e. $d(\Phi/\Phi_0)/dV_{\mathrm{TG}}$, becomes larger when the magnitude of the bias current is increased. Note that if the bias current would generate a magnetic field which would either be directly measurable or would influence the magnetization of the film, it would imply that upon reversal of the bias current, the strength of the SQUID signal also changes sign. However, we observe a symmetric trend in bias current. Data has also been acquired for a negatively magnetized axion device and for a positively magnetized Hall bar device, but their results are very similar to the ones presented here, with the appropriate increase/decrease of the SQUID signal as a function of gate voltage.

We furthermore observe in both panels (a) and (b) of Fig. 6.5 that the flux is not linear as a function of the gate voltage. We will focus our discussion here on panel (b) only, since the Hall bar has more accurate magnetotransport results. The slope of the SQUID signal seems to be steeper for negative voltages. The longitudinal resistance, R_{xx}, which was measured along with the SQUID signal by means of a small ac excitation current of 1 nA, shows the same trend. We plot the measured flux and the longitudinal resistance in Fig. 6.5(c), where both show a steeper trend for negative gate voltages. The SQUID signal was multiplied by -1 to have a more clear visual overlap of the similarity of both curve. This observed similarity will be discussed in Sec. 6.4.3.

To investigate the influence of the bias current on the measured SQUID signal in more detail, we also performed sweeps where the bias current was swept up and down many times while keeping the gate voltage constant. Data is processed similarly to the top gate sweeps. Fig. 6.5(d) shows the flux as a function of bias current for the negatively magnetized top gated Hall bar. The SQUID voltages scale as $\Phi \sim I_{\mathrm{bias}}^2$, which is confirmed by the fit (red line). To compare the data with the top gate sweeps for different bias currents, we also extract the strength of the SQUID signal, $d(\Phi/\Phi_0)/dV_{\mathrm{TG}}$, of Fig. 6.5(b), which is then scaled accordingly. The two different types of measurements are thus in good agreement with each other. For a positively magnetized device we observe a sign change in the SQUID signal, similarly to the observation for the top gate sweeps. For the axion device, similar trends were observed.

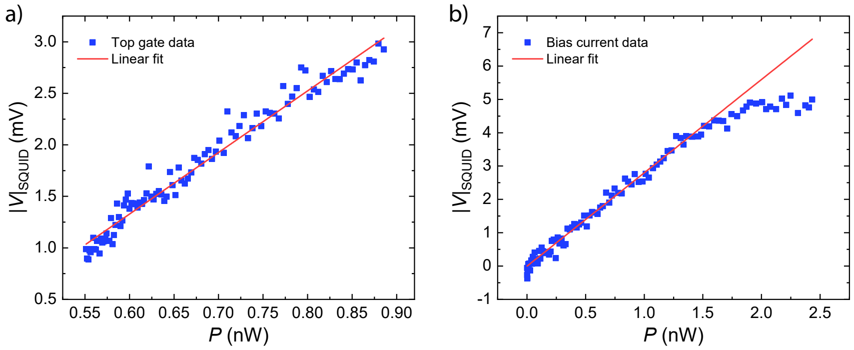

Figure 6.6: Measurement data plotted as a function of the dissipated power. **(a)** The data of Fig. 6.5(b) is shown as a function of power after computing the power based on the sample resistance and the applied bias current of 100 nA. A linear fit was performed over the entire data range. **(b)** The data of Fig. 6.5(d) is shown as a function of power based on the bias current and the sample resistance at a top gate voltage of -10 V. A linear fit was performed over the power up to 1.5 nW.

6.4.3 SQUID signal and power dissipation

We have discussed two different types of experiments. Firstly, based on Fig. 6.5(c) we noted that the SQUID signal depends on the resistance of the sample, $\Phi \propto R_{\text{xx}}$. Furthermore, during the bias current sweeps, we noticed that the SQUID signal depends on the current squared, $\Phi \propto I_{\text{bias}}^2$. A quantity that unifies both relations is power,

$$P = I^2 R \tag{6.2}$$

To see if our data can be explained by a change in power dissipated of the MTI film, we plot both the magnitude of the SQUID voltages (without the voltage to flux conversion) for the top gate sweeps and for the bias current sweeps as a function of power. Data of Fig. 6.5(c) is used for Fig. 6.6(a) and data of Fig. 6.5(d) is used for Fig. 6.6(b). We should note that IV-sweeps of the devices yielded a non-linear current-voltage relation, but using dV/dI to compute the dissipated power as a function of bias current resulted nevertheless in a quadratic dependence in current. More details on the non-linear IV-sweeps can be found in Appendix C.

Both data sets can be fitted well by a linear fit. We did not force the fit intercept to pass through zero voltage at zero power, as the SQUID voltage is a relative number only. The SQUID voltage deviates for higher power, which can only be observed for the bias current data as it extends over a larger power range. We believe that the deviation comes from the fact that the cooling power of the dilution refrigerator increases when temperature increases.

The fact that the SQUID voltage changes with power agrees well with the schematic model that we developed in Sec. 6.4.1 when we discussed the SQUID signal as a function of temperature. When the power dissipation through the sample increases, its temperature will increase as well. As we have seen, increasing temperatures lead to a decreasing magnetization, which is then sensed by the SQUID sensor. Depending on the initial magnetization, the voltage will either increase or decrease. For our data sets containing data of the negatively magnetized film, Fig. 6.5(b) and Fig. 6.5(d), have shown that the SQUID voltage decreases with increasing temperature.

6.5 Conclusions and outlook

In this chapter we have investigated an experimental setup to measure the magnetoelectric response of a topological insulator. We have implemented a SQUID sensor in a flip-chip configuration in a dilution refrigerator, which allows us to perform SQUID measurements, transport measurements and magnetotransport measurements on the same, structured, devices.

We have performed SQUID measurements as a function of different parameters and we have carefully studied and combined the data sets to understand the physics of the experiment, both from a material point of view (i.e. magnetization changing with temperature) and from the experimental setup point of view (i.e. power dissipation). By combining the data sets we were able to verify that power dissipation is a prominent factor in the measurements, which needs to be considered before claims can be made about any magnetoelectric origin of observed features.

Measurements dedicated to finding the magnetoelectric response should be conducted at zero bias current to make sure that no heat is generated during the process. Our measurements at zero bias current show that for the current MTI films the magnetoelectric effect has not been observed. There are two possible reasons for this. Either the fact that the MTI has not fully developed a QAH / axion state can mask the effect, or the measurement setup does not provide the required sensitivity. A combination of both is possible as well.

If the MTI is not fully quantized, it remains a magnetic material with no particular quantized surface currents. It is suggested that θ can be arbitrary in such system [12]. This could lead to a much weaker response. In addition to this, a time-dependent study was carried out by Pesin and MacDonald [159] where they discussed that the finite longitudinal conductivity σ_{xx} in current QAH samples [20, 112] leads to screening of the charge placed above the MTI. Their calculations show that when screening is fully developed and $T = 0$, the signal is only of measurable size when μ/Δ, i.e. the chemical potential with respect to the magnetization gap, is 0. However, for non-zero temperatures, the signal for $\mu/\Delta = 0$ decreases for increasing temperature, while for $\mu/\Delta > 0$ the signal is no longer non-zero (but still small). Even though these findings show that the TME might be present for a finite longitudinal conductivity, it also suggests that a fully developed QAH is required for a sizable effect, and that efforts should be made to minimize the value of σ_{xx}.

Regarding the measurement setup, we should note that the sensitivity of our SQUID, which is $\sim 10^{-5}\ \Phi_0$, is already extremely low. As noted in Sec. 6.3, the measured noise was not magnetic but from the dilution refrigerator itself. As such, to improve the sensitivity to the sample's magnetism, a key improvement would be the minimization of the distance between sample and sensor. Having the possibility to translate the sample would also enhance the measured signal strength, but may experimentally be difficult due to heat dissipation of the required electronics. Calibrating the height (or being able to extract the height) would furthermore allow for the conversion of flux and magnetization, leading to a more direct comparison of the measured data and the material's properties.

Following up on our discussion on both the QAH state and the axion insulator state in Sec. 2.6, we note that, from a measurement setup point of view, only the former can be used for the experiment as proposed here. The axion insulator state requires a finite magnetic field of considerable size. We note that the power supply that was used to drive the superconducting magnet of our dilution refrigerator has a resolution and stability of 0.1 mA and 3 mA/12 hours, respectively. The stability itself would lead to fluctuations of $\sim 10^{-2}\ \Phi_0$, which deteriorates our excellent measurement sensitivity. Furthermore, in the insulating state, $\sigma_{\mathrm{xx}} = \sigma_{\mathrm{xy}} = 0$, so that the sample resistance is very high. At extreme resistances, even the leakage current of the top gate might become significant and can introduce heating effects[7]. The QAH platform would be more suitable for magnetoelectric measurements: the measurements can be performed with the magnet power

---

[7] For the presented measurements in this chapter, the leakage current was < 60 pA over the entire top gate range and the generated power is therefore negligible.

supply turned off, and the longitudinal resistance is very low, so that possibly even transport measurements can be conducted simultaneously with the SQUID measurements. This would allow for direct verification of the gate tuning not changing the magnetization, as ideally the gate should then only be tuned within the QAH region. Of course, the low resistance of the QAH state is observed in a four-terminal configuration which does not yield information about current dissipation at the source contacts, which may still heat the sample.

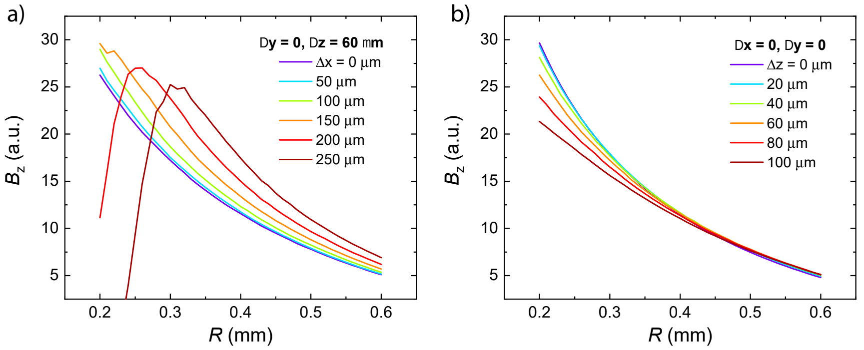

Figure A.1: Simulation results for top gates of different radii. **(a)** The detected magnetic field when the sensor is displaced along an in-plane axis, Δx (parallel to the sample's surface). When the gate radius is smaller or comparable to the displacement of the sensor, the measured signal will be weak. **(b)** The detected magnetic field when the sensor is centered above the gate. The distance Δz between the sensor and sample surface is increased.

Appendix A: Considerations for top gate dimensions

In the original proposal of Qi *et al.* [24], the magnetic flux of a point charge is calculated through Eqn. 2.25. In our experiment, we consider a circular gate along whose edge this current must flow. For a large gate, the image charge method is not applicable anymore and therefore we resort to a simple model where we consider the circulating current that is generated due to the $\nabla\theta \times \mathbf{E}$ term. If we consider this current to form a loop, we can compute the magnetic field at the center of a loop, which is given by

$$B = \frac{\mu_0 I}{2R}, \tag{A.3}$$

where I is the current through the loop and R is the radius of the loop. From this equation, one could argue to make the gate as small as possible[8]. However, practical issues arise due to the manual alignment of the flip chip SQUID sensor on top of the sample. In Sec. 6.3 we have seen that a typical misalignment may be 100-200 μm in-plane and that the distance from SQUID to sample may be 60 μm. Note that the thermal stress on the

---

[8] Note that the electric field at the edge of the loop does not change, since $E_z = V/d_{\text{gate}}$ is not changed when the radius of the gate is changed.

flexible PCB can alter the distance from sensor to sample, as discussed in Sec. 6.3. The sensor is mounted under an angle, so any movement pivots around that point and automatically changes the in-plane alignment as well.

We carried out COMSOL simulations where we considered a loop through which a fixed current is passed. The loop size is then varied and the magnetic field is probed at different positions in space. We define the loop to be in the xy-plane, centered at (0,0) with $z = 0$ as well. In Fig A.1(a) we plot the measured magnetic field perpendicular to the loop $B_z(x, y, z)$ as a function of the radius of the gate. We set our probe height to 60 μm to match the expected position of the SQUID and vary the in-plane offset Δx in one of two in-plane directions. We immediately see that if the $\Delta x > R$, the SQUID signal drops significantly. Hence, for our flip-chip approach we might choose a gate size $R > 200$ μm. In Fig. A.1(b) we vary the height of the sensor while being above the center of the loop. While for small gates ($\Delta z \sim R$) the magnetic field strength depends a lot on the sensor height, for relatively large gates ($R > 200$ μm) the sensor height is of less importance as the signal strength only varies a factor 2 over a Δz of 100 μm. We choose our circular gate to be 500 μm to make sure that the optical alignment requirements (during loading the sample) and thermal stress misalignments are relaxed.

Appendix B: Film magnetization for SQUID measurements

After performing the SQUID measurements on the top gated Hall bar device, we unloaded the sample from the cryostat, removed the SQUID and replaced the aluminium radiation shield by the standard shield. We then loaded the sample again to perform magnetotransport measurements at temperatures down to base temperature. To investigate the process of magnetizing the films (as discussed in Sec. 6.4), we repeated the sequence and also recorded the data during the process of ramping the magnet to zero and cooling the sample back to base temperature. Furthermore, we repeated the sequence by only going to 2 K instead of 9.5 K. Performing the sequence at 2 K would do no harm for the radiation shield (no Lorentz forces on the induced screening currents by the Meissner effect as the shield is not superconducting at this temperature), but it would possibly trap flux in the SQUID, or even destroy the sensor.

In Fig. A.2, we show the results of the two magnetization processes performed at 9.5 K (blue line) and 2 K (red line). In both cases, we first

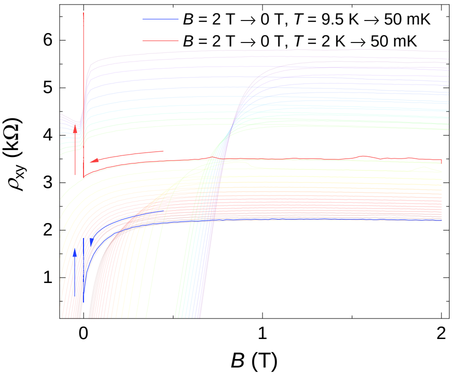

Figure A.2: Magnetotransport measurements on the top gated Hall bar device for a variety of temperatures. The thick lines represent the data of magnetization processes. The sample is heated to the desired temperature (2 K or 9.5 K), after which the magnetic field is ramped to 2 T. At this point, we start the measurements and ramp the field back to zero, after which the sample is cooled back to base temperature. The background data shows the magnetotransport of Fig. 4.3, which was measured at the exact same device.

heat the sample to 9.5 K or 2 K and subsequently ramp the magnet to 2 T. We then start the measurement and ramp the magnet to zero field while keeping the temperature constant. Then, at zero field, we cool down the sample to 50 mK while we keep measuring the transverse resistance. The magnetization loops visible in the background of the figure are the data of Fig. 4.3(b), where we measured magnetotransport from 100 mK (purple loop) to 9.5 K (red loop).

For the sequence performed at 2 K, we see that ramping the field back to zero leaves the film almost fully magnetized. Upon lowering the temperature, the resistance increases beyond the measurement data of 100 mK, indicating that at low temperatures the film remains (almost) fully magnetized. However, for the sequence performed at 9.5 K, we observe that ramping down the field reduces the overall magnetization of the film significantly. Furthermore, cooling down the film leads to a final resistance (magnetization) which is only $\sim 1/3$ of the value observed when magnetizing the film at 100 mK.

While the fact that the sample's magnetization is less then fully developed our SQUID measurements does not hamper the analysis as presented in the preceding text, it does signify the need to magnetize films at low

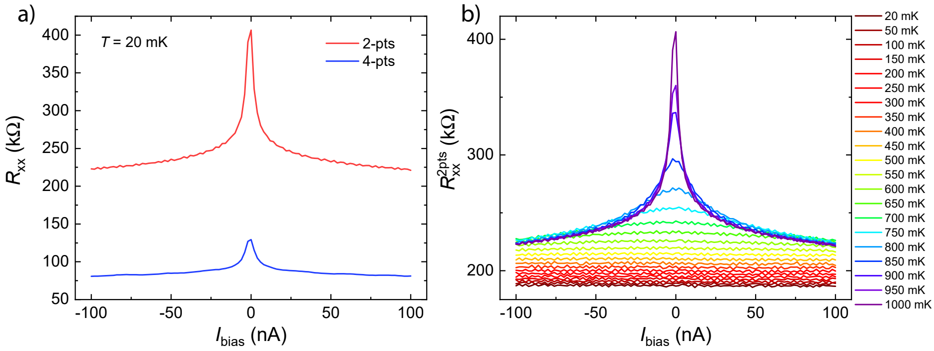

Figure A.3: Non-linear current/voltage characteristics as a function of bias current. **(a)** Comparison between the two terminal and four terminal resistance of the Hall bar device at base temperature. **(b)** Two terminal resistance of the Hall bar device for different temperatures. Above 500 mK the resistance remains constant as a function of bias current.

enough temperature to fully magnetize them. Especially for QAH films this is something that should be investigated in detail before performing the experiments with the SQUID on such films. We however also have to note that after magnetizing the sample (and SQUID) at 2 K, it was impossible to tune the SQUID when the system was at base temperature again. Flux was trapped in the sensor, and hence heating the system to 9.5 K and afterwards cooling back to base temperature was enough for the SQUID to work properly again.

Appendix C: Non-linear IV curves

During the measurements we observed that the IV-curves showed a nonlinearity, where the resistance of the sample increases close to zero applied current. We measure both $V(I)$ and $dV/dI(I)$ by means of dc and ac signals, and focus here on the ac results. Fig. A.3(a) shows that the increase of resistance (or strictly speaking, dV/dI) is originating from the material itself, as it is apparent in both two and four terminal measurements. Furthermore, Fig. A.3(b) shows that the increase in resistance is only observed at low temperatures. While this is in agreement with the measurements on BST in Sec. 3.5.3, the size of $\Delta\sigma$ is much smaller. Furthermore, the EEI was present most strongly at the DP. The samples presented here could not be tuned to the DP, but have a magnetic gap. A more elaborate study should be carried out to find the origin of the peak for the MTI.

For the study presented in this chapter it is important to note that the longitudinal resistance is not constant as a function of bias current, which means that we should consider a varying R in Eqn. 6.2. To do so, we use the values of dV/dI and compute the power accordingly. While R_{xx} at zero bias current increases to almost twice its value for high currents, the resulting power - computed as $(dV/dI) \cdot I_{\mathrm{bias}}^2$ - still scales perfectly with current squared. In the main text, plots concerning power have used the power as calculated here.

Chapter 7

Josephson junctions and arrays on topological materials for phase interference measurements

Fractional charges can be induced by magnetic fluxes at the interface between a topological insulator and a type-II superconductor due to axion electrodynamics. In a Josephson junction array with a hole in the middle, these electronic states can have a phase interference in an applied magnetic field. Here, we experimentally realized a Josephson junction array on a mechanically exfoliated flake of $BiSbTeSe_2$ *and compare its results to a Josephson junction array on an Au layer. We performed numerical simulations which are in good agreement with the results. No axion charge-related effect was observed in the sample, possibly because of the limited array size. In order to increase the number of islands we switched to thin films, where we first fabricate Josephson junctions on BST films to investigate the junction properties so that we obtain new requirements for a Josephson junction array on this material.*

7.1 Introduction

We have discussed the experimental proposal to measure the topological magnetoelectric effect through a Josephson junction array (JJA) in detail in Chapter 2. When a magnetic flux pierces the interface of a topological insulator, axion electrodynamics dictates that a fractional charge will be bound to this magnetic flux. More specifically, it was shown that when one considers a quantized amount of magnetic flux, such as the magnetic flux quantum $\Phi_0 = h/2e$, that the electric charge will be quantized as well in units of $e/4$ [41]. To detect this bound charge one then makes use of a JJA, where the Josephson vortices are the magnetic fluxes that bind the fractional charges. When the Josephson vortices are depinned and move through the array, they interfere, and the oscillation period of the interference differs for the trivial and fractional charges [40].

In this chapter, we perform a series of experiments. We start with JJA devices on mechanically exfoliated flakes of $BiSbTeSe_2$ (BSTS) and on an Au film as non-topological reference sample. Here, we study the response of the array upon varying the magnetic field. Numerical simulations of JJA are performed to verify the experimental results. We then make the transition from exfoliated flakes of BSTS to the thin films of BST (see Chapter 3). The thin films have different properties (regarding superconductivity) with respect to the readily explored flakes of BSTS [160] and therefore we first fabricate and characterize single Josephson junctions on the thin films.

7.2 Interference measurements on Josephson junction arrays

7.2.1 Device fabrication

The Josephson junction arrays on the reference and BSTS devices were fabricated in similar ways[1]. BSTS is a topological insulator with a crystal structure that is identical to BST (see Fig. 3.1(a)). The Te lattice sites are shared between Te and Se, similar to the Bi and Sb lattice sites. The Dirac point of the surface states lies within the bulk band gap.

---

[1] The results of Sec. 7.2 have been published as: Brevoord *et al.*, Phase interference for probing topological fractional charge in a $BiSbTeSe_2$-based Josephson Junction Array, *Nanotechnology* **32**, 435001 (2021). I have been primarily involved in device fabrication, measurements and writing.

For the BSTS device, high quality BSTS single crystals were grown using a modified Bridgman method [160]. BSTS crystal flakes were mechanically exfoliated on SiO_2/Si^{++} substrates. The JJA and electrodes were defined by standard e-beam lithography (EBL). We deposited a layer of 60 nm Nb by DC-sputtering, which is followed by a 2 nm capping layer of Pd. A subsequent EBL step is used to define the hole, which is then etched by Ar^+ milling. The individual islands of the JJA are 150 nm in diameter and are spaced 250 nm apart. A scanning electron microscopy (SEM) image of the device is shown in Fig. 7.2(a).

For the fabrication of the reference device, a rectangle of 6 μm×5 μm with a square hole of 2.5 μm×2.5 μm is patterned using EBL. We deposited a layer of 2 nm Ti and 40 nm Au by sputter deposition. Before lift-off, the device is etched by an Ar^+ milling under a small angle while rotating the sample. This is to remove Au walls at the edges which are formed due to the lift-off process. A subsequent EBL step patterns the electrodes and the JJA islands, which again are 150 nm in diameter and are spaced 250 nm apart. We sputter deposit 60 nm Nb and 2 nm Pb on this device as well. A SEM image of the device is shown in Fig. 7.1(a).

7.2.2 Measurements on the reference device

Fig 7.1(b) shows the results of measurements on the reference device. The device was measured in an Oxford Triton 300 dilution refrigerator with a base temperature of 10 mK. The system is equipped with a superconducting vector magnet. Measurements at small magnetic fields (i.e. < 500 Gauss) were performed by using a Keithley 2400 source-measure unit (SMU) to drive the magnet current to ensure a high resolution and stability of the applied magnetic field. In addition to measuring the dc bias current and voltage, we source a small ac excitation current and measure the differential resistance by means of standard lock-in techniques. The differential resistance, dV/dI, as a function of the bias current was measured at different magnetic fields. The bias current was swept from negative to positive. As a result of the large critical current at base temperature of the dilution refrigerator, these measurements were performed at 1 K. The oscillation of the critical current, I_c, is clearly visible, which is extracted and plotted as the blue line in Fig. 7.1(d). This oscillation is due to the Cooper pairs moving around the hole, after which they interfere. Simulations were performed on a JJA with the same device geometry, as shown in Fig. 7.1(c). Here, the color of the dots represent the phase of each island. The blue arrows indicate the direction and magnitude (normalized to the I_c of each junction) of

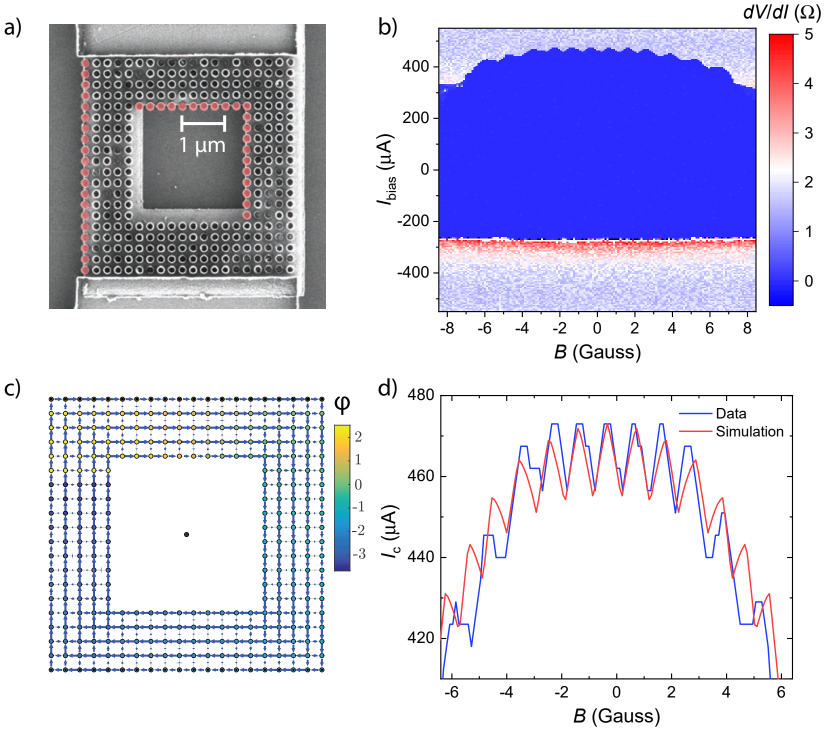

Figure 7.1: Results of the reference device. **(a)** SEM image of the reference device of 20×20 Nb islands with a hole of 10×10 islands. The islands are 150 nm in diameter and there is 250 nm in between the centers of the islands. Due to the misalignment of the EBL process, 3 lines are removed from the simulation model (marked in red). **(b)** The differential resistance as a function of the magnetic field, applied perpendicular to the array, at $T = 1$ K. The bias current is swept from negative to positive bias current. The scale has been adjusted to clarify the features; gray indicates data points above the scale. **(c)** The geometry used to simulate the $I_c(B)$ of the device shown in panel (a). **(d)** $I_c(B)$ deduced from the measurement depicted in panel (b) and the simulated $I_c(B)$ of the geometry shown in panel (c), where the marked islands of panel (a) have been removed.

the current. Details of the numerical model can be found in the Appendix. Note that due to misalignment of the array with respect to the Au film, we removed the marked islands in Fig. 7.1(a) from the final geometry that was used for the simulation. The results of the simulated $I_c(B)$ are shown in red in Fig. 7.1(d). The simulations yield results in dimensionless units. The maximum critical current of the central lobe in the measurements is used as normalization value for the current. To convert the dimensionless field to physical values, we use $B = \eta f \cdot \phi_0 / A_{\text{hole}}$ for the external field, where f is the frustration factor, A_{hole} is the area of the hole and η is an additional prefactor which is required for fitting the experimental results. For the arrays on the reference device, $\eta = 0.456$. This prefactor is an indication of non-perfect geometry or defects in the samples. Therefore to maintain one quantized fluxoid, a large effective area is needed at low field. The effective area of one Josephson vortex is defined as $A^* = A_{\text{hole}}/\eta$. We will discuss this later in the discussion section. Measurements over a larger range of magnetic fields, showing clear modulations of $I_c(B)$ by the plaquettes[2], verify the good quality of the JJA. We will show an example of such measurement later.

7.2.3 Measurements on the BSTS device

The results of the BSTS device are shown in Fig. 7.2(b). Here, measurements were conducted at base temperature. For the interference measurements, the bias current was applied from the bottom to the top of the device. Clear oscillations were observed over a range of ±8 Gauss. The extracted $I_c(B)$ is shown as the blue line in Fig. 7.2(d). For the simulations, we reproduced the exact geometry of the device, as shown in Fig. 7.2(c). The resulting $I_c(B)$ of the simulations is shown as the red line in Fig. 7.2(d), where the scaling factor $\eta = 0.50$. The results of the measurements and the simulations are in great correspondence as the asymmetry and the shape of the envelope match. However, the simulations do not take topological effects into account.

In addition to the measurements of dV/dI as a function of bias current and small magnetic fields, we also performed the same set of measurements for large magnetic fields. While we use a Keithley 2400 SMU to drive the small magnetic fields, we use an Oxford Instruments MercuryiPS vector magnet power supply to drive larger magnetic fields (up to 1 T or 6 T, de-

---

[2] A plaquette is square area with four Josephson islands on its corners and thus encloses the area of four Josephson junctions.

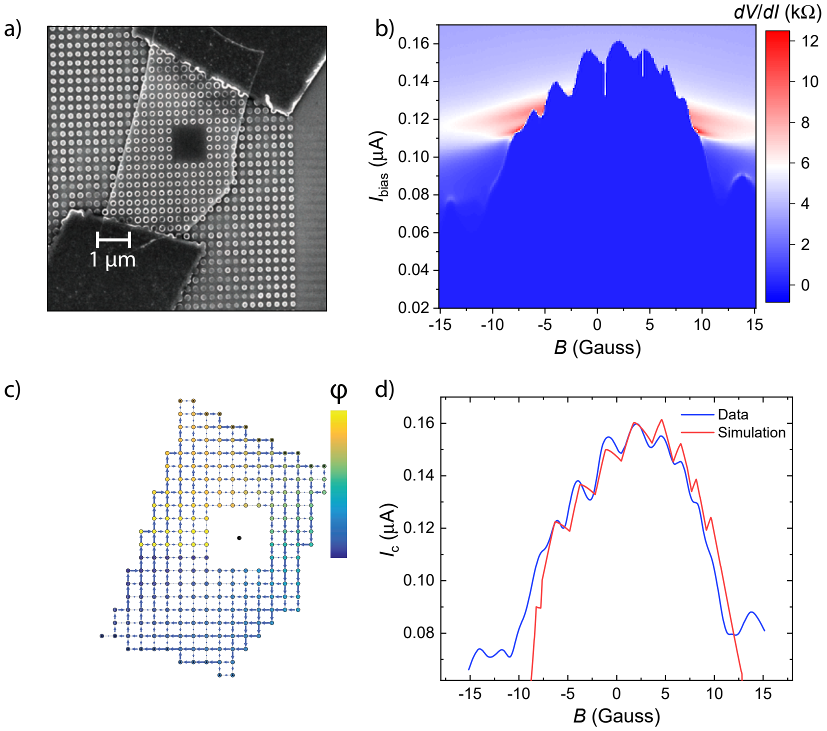

Figure 7.2: Results of the BSTS device **(a)** SEM image of the BSTS device with a hole of 4×4 islands. The islands are 150 nm in diameter and there is 250 nm in between the centers of the islands. **(b)** The differential resistance of the device as a function of the magnetic field, applied perpendicular to the array, at base temperature. **(c)** The geometry used to simulate the $I_c(B)$ of the device shown in panel (a). **(d)** $I_c(B)$ deduced from the measurement depicted in panel (b) and the simulated $I_c(B)$ of the geometry shown in panel (c).

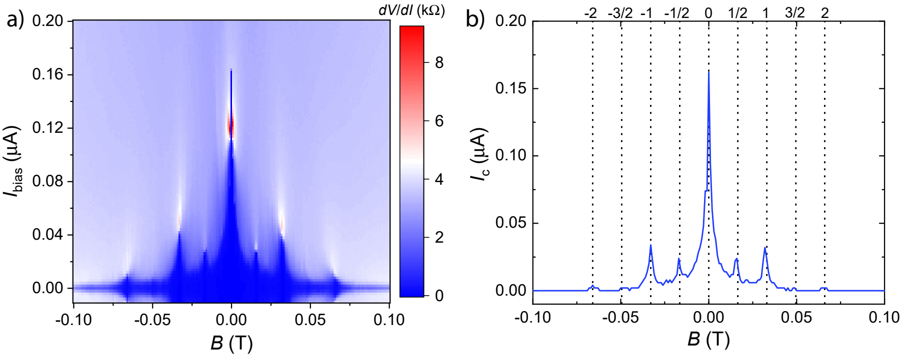

Figure 7.3: Measurements of frustration factors of the BSTS device. **(a)** Differential resistance of the device as a function of bias current and magnetic field. The critical current is increased for certain values of the magnetic field, corresponding to (fractional) filling factors. **(b)** The extracted $I_c(B)$ of the device, where the frustration factors are indicated by the dashed lines.

pending on the direction). In Fig. 7.3(a) we show the measurement results for the BSTS device, where we swept the magnetic field up to 0.1 T. We see that I_c is larger for certain amounts of applied magnetic field. These maxima in I_c correspond to certain frustration factors $f = B/\Delta B_{\mathrm{plaquette}}$ for which periodic vortex patterns can be formed, which lower the ground state energy of the system [161]. Here, $\Delta B_{\mathrm{plaquette}} = \Phi_0/A_{\mathrm{plaquette}}$, where $A_{\mathrm{plaquette}}$ =(250 nm)^2 so that $\Delta B = 33.1$ mT. In Fig. 7.3(b) we show the extracted $I_c(B)$ and indicate the expected positions of certain frustration factors by the dashed lines. We see that our measurements are in great correspondence with the expected values, hence indicating a high quality JJA.

7.2.4 Discussion

Both the reference and BSTS devices show an oscillation of the $I_c(B)$ as a result of the Cooper pairs moving around the perpendicular magnetic field inside the hole. This is also verified by the performed simulations. The expected oscillation period in magnetic field ($\Delta B = \Phi_0/A$) is related to both the area of the hole (A_{hole}) and the total area of the arrays (A_{total}) and therefore lies between $\Phi_0/A_{\mathrm{total}}$ and Φ_0/A_{hole}. For the reference sample, having a lattice constant $a = 250$ nm and being a 20×20 array with a 10×10 hole, we find $\Delta B_{\mathrm{total}} = 0.83$ Gauss and $\Delta B_{\mathrm{hole}} = 2.30$ Gauss, where for the latter we take the area of the hole spanned by the first ring of islands, being a 12×12 ring. The measured effective area, A^*, of approximately 1 Gauss is then exactly A_{hole}/η. Note that the value of η is computed by finding an optimal scaling factor between the measurement data and simulation data by means of a fit procedure, and hence does not take any explicit area into account.

Prefactor and effective area

The discrepancy between the experimental results and the simulation lie in the fabrication-induced artificial defects which can be described by the prefactor η or an effective area $A^* = A_{\text{hole}}/\eta$. These defects can be induced due to bad lift-off process or misalignment of the EBL patterning. For example, in the reference sample (shown in Fig. 7.1(a)), the misalignment possibly resulted in missing lines of islands or a reduced I_c in certain lines. Therefore, the effective area of the hole can be larger than that of the design. A comparison of the simulations with and without the geometry corrections (i.e. with or without removing the marked islands of Fig. 7.1(a) from the simulation model) has been carried out, where it was found that the prefactor of the corrected simulation (i.e. with the marked islands removed) yielded a larger prefactor (0.54) which is closer to 1 than the prefactor for the uncorrected simulations, being 0.46. Additionally, the patterns were written without proximity effect correction. Therefore, islands in the middle of the array may be slightly overexposed, making them wider and hence increasing their I_c. A similar situation can be found in the TI-based device (Fig. 7.2(a)), in which the simulation captured every single junction according to the SEM image, but the irregular shape of the flake and the inhomogeneity in the critical current distribution (partially sitting on the edge, bad lift-off close to the leads) resulted in a larger effective area than the simulation. To further improve the signal, highly efficient and high-yielding patterning of the arrays is desired.

Topological effect

No clear effects of the topological fractional charge in the BSTS device was observed. A reason for this may be that the charge density induced by the magnetic vortices is small compared to the I_c. Secondly, the effect of the other interface of the BSTS flake may cancel the effect. If the flake is too thin the effect of focused flux will be present at both interfaces. As $\boldsymbol{\nabla}\theta$ has opposite signs at both interfaces of the BSTS flake, the effect may be canceled (see Chapter 2). However, the cancellation of the effect may still depend on the thickness of the flake. The BSTS flakes are typically in the

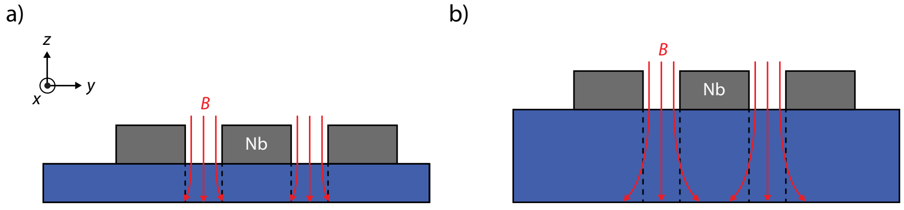

Figure 7.4: Magnetic field through flakes of different thicknesses. **(a)** Schematic side view of a JJA on a relatively thin TI flake. Here, the flux does not spread homogeneously at the bottom surface. **(b)** Schematic side view for a thick TI flake. The flux becomes (more) homogeneous at the bottom surface and hence the bottom surface does no longer bind fractional charges locally.

order of 100 nm. The flux may spread out and overlap on each other at the bottom surface. If this is the case, effects of the fractional charge will be present. This can be seen in Fig. 7.4. In addition, the oscillation of the $I_c(B)$ due to the topological fractional charge is 8π-periodic, while only 7 clear peaks of the $I_c(B)$ are measured. By increasing the island density and reducing the distance between the islands, the I_c is expected to increase, while the $I_c(B)$ is expected to decrease at a smaller rate. This is expected to increase the number of measured peaks of $I_c(B)$ in order to measure signatures of the fractional charge as a result of topological effects. A larger number of islands is also expected to increase the visibility of different oscillations.

7.3 Josephson junctions on BST thin films

Since the size of the exfoliated flakes is limited to a few micron, a more suitable platform for an increased number of islands is to use TI thin films. While Josephson junctions of topological materials such as the previously mentioned BSTS have been investigated previously [160], our topological thin films of Chapter 3 have not. Therefore, we first resort to single Josephson junctions before we fabricate arrays on these thin films. To have maximum control of the devices, a gate tunable topological film would be of most interest. Because of the lift-off process for the Nb electrodes, realizing a top gated Josephson junction becomes difficult because of the side walls of the electrodes, which are visible as the bright edges of every Nb island in Figs. 7.1(a) and 7.2(a). Hence, it would be best to fabricate junctions on

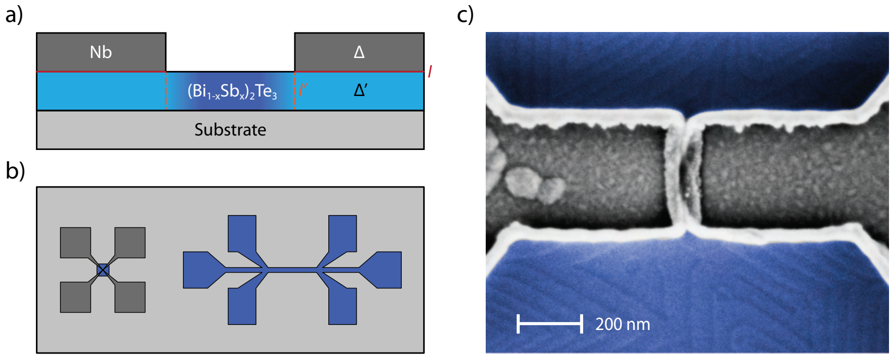

Figure 7.5: Schematic overview of Josephson junction devices on thin films. **(a)** Side view of the Josephson device. The Nb leads (with gap Δ) proximize the topological insulator underneath (with gap Δ'). The interface in between the Nb and the TI is denoted by I. A second interface, denoted by I', exists between the proximized TI and the non-proximized TI. The latter forms the weak link of the junction. **(b)** Top view of the devices. On top of the grey substrate there are square patches of TI (blue) with Nb electrodes (dark grey) on top, which form the Josephson junction devices. Each chip contains 6 devices along with a Hall bar for magnetotransport. **(c)** False color SEM image of a 40 nm long junction on a 50 nm thick BST film grown on InP. The film is shown in blue, the Nb electrodes in gray. The side walls of both leads touch each other, but (magneto)transport measurements on the junction show that it is not shorted. The QL steps of the film are visible in the background.

$SrTiO_3$, so that the substrate can be used as a gate dielectric for back gating experiments. Unfortunately, as already discussed in Sec. 3.5.3, all junctions on $SrTiO_3$ remained resistive and hence we focus here on junctions that were fabricated on BST films grown on InP substrates, albeit without gate.

While the focus of the experiments in Sec. 7.2 was mainly on the collective behavior of Josephson junctions, we will now investigate the properties of a single Josephson junction. We present a schematic overview of our junction in Fig. 7.5(a). A thin film of BST is deposited on the substrate, on top of which two Nb electrodes are deposited. At sufficiently low temperatures the Nb will turn superconducting with a corresponding critical temperature T_c, to which its superconducting gap is related through the Bardeen-Cooper-Schrieffer (BCS) theory; $\Delta = 1.76 k_B T_c$ [162]. Due to the proximity effect the topological insulator underneath the Nb will be proximized, which means that it will become superconducting too, with its own gap, Δ', where $\Delta' < \Delta$. We denote the interface between the Nb and the proximized TI by I. The part of the BST film in the middle of the device is not proximized from above and thereby forms the weak link of the Josephson junction. The barrier between the proximized (light blue color in the figure) and non-proximized (dark blue) TI is denoted by I'.

7.3.1 Device fabrication

While we already discussed most of the fabrication processes used throughout this thesis in Sec. 3.4, the junction devices discussed here follow a hybrid UV and EBL recipe which we therefore discuss in more detail. We start by depositing the thin film of BST as outlined in Chapter 3. After MBE growth, we use standard UV lithography and Ar ion milling to define 6 square patches of film (each 100 μm × 100 μm in size), along with an optical Hall bar and alignment markers. The Hall bar and one of the 6 square patches are shown in blue in Fig. 7.5(b). Then, we use standard e-beam lithography to define the superconducting electrodes, followed by the sputter deposition of 75 nm of Nb and a 2 nm Pd capping layer. Finally, the devices are wirebonded by hand with silver paste and Au wires. We should note that the Hall bar does not contain Nb contact pads.

7.3.2 Measurement results

We measured our devices fabricated on a 10 nm $(\mathrm{Bi}_{0.4}\mathrm{Sb}_{0.6})_2\mathrm{Te}_3$ thin film in an Oxford Triton 200 dilution refrigerator with a base temperature of 20 mK. IV-curve measurements were performed by sweeping the bias current while recording the voltage. In addition to the dc bias current, a small ac excitation current of 1 nA was used to measure the differential resistance of the device by means of standard lock-in techniques.

The IV-curves of the junction, measured by sweeping the bias current up and down, as shown in Fig. 7.6(a), reveal that the junction is hysteretic. A critical current I_c, of 238 nA is extracted, along with a retrapping current I_r of 213 nA. To investigate whether the hysteresis is originating from a capacitance in the system, we first consider the RCSJ model. Because of the non-trivial geometry of the junction - the superconducting electrodes have a quite substantial overlap with the BST film since the latter is not patterned but is a rather large square patch, which means that there might be extra contributions to the capacitance originating from the planar leads - COMSOL simulations were performed to estimate the capacitance of the lateral junction. We found a capacitance of $\sim 10^{-14}$ F. After extracting

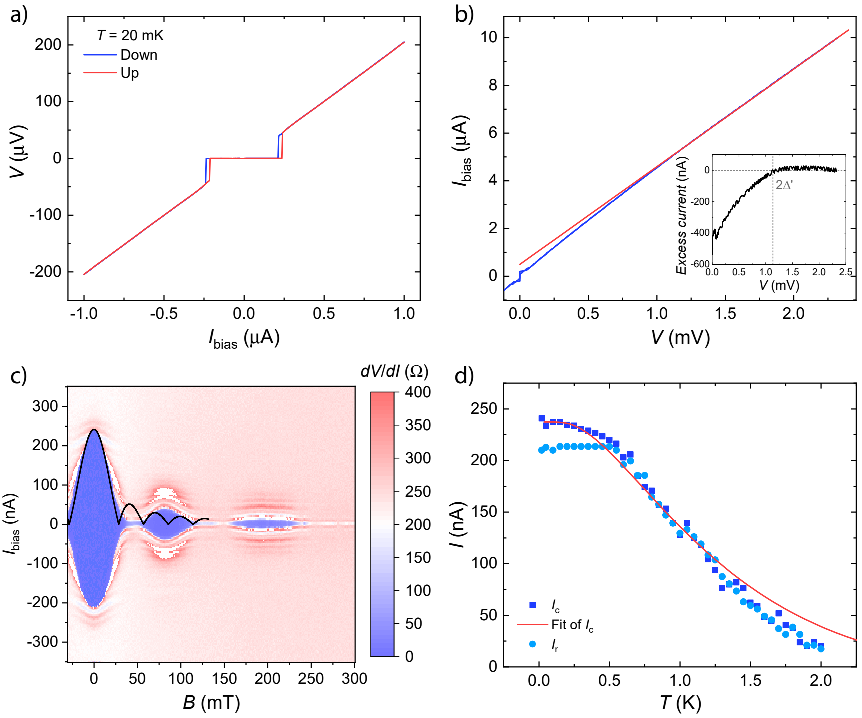

Figure 7.6: Transport data of BST devices on an InP substrate. **(a)** IV-curve of the junction at base temperature. **(b)** Excess current analysis. The inset shows the fit residual, which indicates the position of the gap Δ'. **(c)** Magnetic field dependence of I_c. The black line is a fit to the data. **(d)** Critical current extracted at different temperatures.

the normal state resistance R_n, which we will discuss later, we used the RCSJ model to simulate our junction, for which we varied the Stewart-McCumber parameter, β_C [163], until the value of the retrapping current matched our experimental data. The found $\beta_C = 1.6$ leads to a capacitance of $\sim 5 \cdot 10^{-12}$ F, which is two orders of magnitude larger than the expected capacitance, ruling out capacitance as the reason for hysteresis. The work of Courtois *et al.* [164] shows that junctions can have hysteretic IV-curves despite their small capacitance because of the increase of the electron temperature in the normal metal (in a SNS-junction) when the junction switches to the resistive state. As our junction is of the same kind and shows very similar behavior, we also attribute our hysteresis to this heating effect.

The IV-curve was also measured for larger bias currents, as shown in

Fig. 7.6(b). We can extract the size of the proximity gap Δ', along with the excess current I_{exc}. For analysis purposes, we plot the bias current as a function of measured voltage. To extract the value of the proximity gap, we fit a linear line through the data, where we fit only the data for larger voltages. The fit is shown in the figure as the red line. We plot the fit residual (i.e. the excess current) in the inset [165]. The fit starts to deviate from the data when the voltage becomes lower than $2\Delta'$. From this, we deduce that our proximity gap $\Delta' = 0.57$ meV. The excess current itself is $I_{\mathrm{exc}} = 0.5\ \mu$A, from which we can deduce the transparency τ of the barrier I', which is found to be $\tau = 0.47$ [166]. This value is lower than values found for junctions where leads were deposited *in-situ* [167]. The interface transparency of the junction can be lower due to the fabrication process, which involves etching the (partially oxidized) top surface of the TI film, possibly leading to defects, and the deposition of Nb electrodes, which can dope the material, so that the proximized and non-proximized TI have a large v_F mismatch.

The differential resistance of the junction was measured as a function of bias current and applied magnetic field to obtain the $I_c(B)$ pattern. This pattern was extracted from the data of Fig. 7.6(c). Because of our junction geometry, we resorted to fitting our data with the model introduced by Barzykin and Zagoskin [168], where an ‘open’ junction is considered (i.e. a junction where leads are deposited on top of a much larger film, such as is the case for our devices). We consider the diffusive limit and use $L = 40$ nm, $W = 350$ nm and $\xi_N = 10$ nm as model parameters, where the L and W are the junction length and width, and ξ_N is the diffusive coherence length. We will discuss the value of the coherence length in detail later. The model calculates the critical current as a function of Φ/Φ_0, where Φ is the flux through the junction and $\Phi_0 = h/2e$ is the magnetic flux quantum, with $2e$ the charge of a Cooper pair. To convert the flux into a magnetic field we use an effective area, which not only considers the junction area $L \cdot W$, but also takes flux focusing into account [169]. Here, we considered a London penetration depth λ_L of 39 nm for bulk Nb [170]. The modeled critical current is shown in Fig. 7.6(c) as the black line. The first lobe is in good agreement with the data, but for the other lobes the data is highly irregular. Because of the relationship between $I_c(B)$ and $j_c(x)$, the latter being the supercurrent density distribution through the weak link, we deduce that the supercurrent is not homogeneously distributed along the junction, as a homogeneous $j_c(x)$ would lead to a regular Fraunhofer pattern, or, for geometries such as for our device, to the pattern as described by Barzykin and Zagoskin.

In addition to the measurements at base temperature, IV-curve measurements were performed at a series of temperatures ranging from 20 mK to 9.5 K. As the junction is hysteretic, the bias current was swept both from positive to negative values as well as from negative to positive values. In Fig. 7.6(d) we extracted the critical current as a function of temperature from every IV-curve where the bias current was swept from a negative to a positive current. The junction is hysteretic up to 500 mK, above which the critical current and retrapping current, I_r, overlap. Below 500 mK, the retrapping current (blue) is constant in temperature, while the critical current (red) is not. This has been observed in more lateral junctions on topological films [171, 172]. In order to model the diffusive supercurrent we use the Usadel equations [173] with effective boundary conditions [174]. Numerical code was used for the fitting[3], for which we introduce the parameters $\gamma = \rho_S\xi_S/\rho_N\xi_N$ and $\gamma_B = R_B/\rho_N\xi_N$. Here, $\rho_{S,N}$ is the resistivity of the superconductor and normal metal, respectively, and R_B is the interface resistance. While γ is a measure for the mismatch between the proximized and non-proximized TI, γ_B is a measure of the interface transparency of interface I'. Because of the inhomogeneous current distribution (as was described in the previous section), we scale the current axis freely and therefore should note that the interface transparency γ_B can then be any arbitrary number, since it does not alter the shape of the temperature dependence of the normalized current. The parameter γ was set to 1. The last input parameter is T_c, which we chose to be 3.7 K, which matches the extracted gap size that was extracted from the excess current analysis. We find that the model agrees well to the data when the parameter $d/\xi_N = 4$. The parameter d/ξ_N describes the ratio between the thickness d of the normal layer (i.e. the 40 nm wide long junction) and the superconducting coherence length. From this we deduce that $\xi_N = 10$ nm.

In addition to the data that is presented above, magnetotransport measurements have been conducted on a standard Hall bar device that was fabricated on the same sample. We find a magnetoresistance with a shape that is very similar to the BST sample on $SrTiO_3$ in Sec. 3.5.1, but have no gate to tune the electronic properties. From the slope of the Hall signal we deduce that our carrier type is holes, and assuming a single transport channel we find a carrier density $n_s = 7.3 \cdot 10^{12}$ cm^{-2}. If these would be surface states, their Fermi wave vector can be estimated via $|n_{\mathrm{SS}}| = k_F^2/4\pi$ [72], where we note that $n_{\mathrm{SS}} = n_s/2$. The resulting Fermi energy $E_F = \hbar v_F k_F$ is

---

[3] We thank A.A. Golubov for the numerical code.

then 0.17 eV below the DP when a Fermi velocity $v_F = 3.7 \cdot 10^5$ m/s is considered [72]. Such Fermi energy, in combination with the band structure of BST and recently acquired ARPES measurements of our films on InP [99], suggests that the Fermi level crosses both the bottom of the surface states and states in the bulk valence band. As such, the junction transport becomes an admixture of both transport channels. For a crude approximation of the coherence length we can consider an effective mass of $0.15m_e$ for the surface states [175], for which we obtain $l_{\mathrm{mfp}} \sim 10$ nm. For a diffusive junction, we then find a coherence length $\xi_{\mathrm{diff}} = \sqrt{\hbar D/2\pi k_B T_c} \sim 25$ nm, which is longer than the extracted ξ_N from the fitting of the $I_c(T)$. The interplay between the surface and bulk states could be a possible reason for a lower measured ξ. For the bulk transport channel, the (Fermi) velocity will differ and as such a quantitative value for the coherence length remains difficult to obtain.

7.4 Conclusion and outlook

We have realized Josephson junction arrays on Au films and exfoliated TI flakes to search for the interference of fractional charges. In both devices we observe clear oscillations of the critical current with respect to the applied magnetic field. By replicating the device geometry in a simulation model, we were able to reproduce the $I_c(B)$ patterns for both the reference and the TI device. The asymmetry in the measured data is captured well within the numerical simulations and hence the origin of the asymmetry lies within the device geometry. A scaling factor was introduced to compensate for fabrication-induced artifacts such as misalignment on the reference sample, the absence of proximity effect correction and inhomogeneities in the shape of the flake. No clear effects of the topological fraction charge have been observed in the BSTS device. We attribute this to the fact that for the current device there is a small number of oscillations observed, and the possible cancellation of the effect when two surfaces induce opposite fractional charges. It is unclear at this moment whether the interference itself is affected by opposite charges and thus whether the effects can be measured in thin flakes or thin films.

We also have shown that Josephson junction devices can be fabricated on thin films of BST when the film is deposited on an InP substrate. The modulation of the critical current with respect to magnetic field shows that the junction has an inhomogeneous current distribution. The Usadel equations

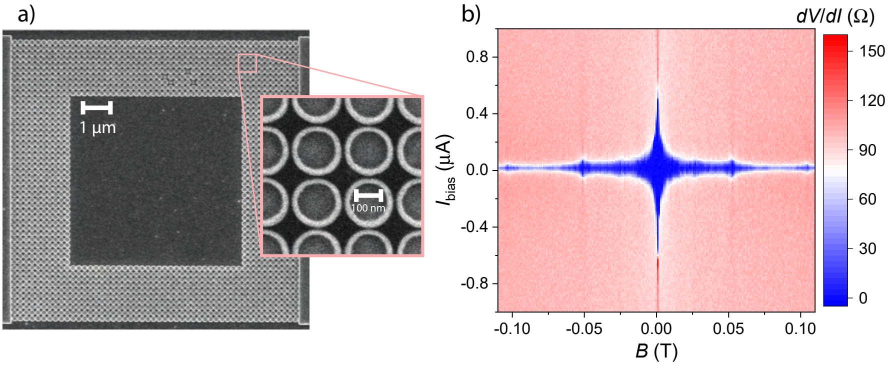

Figure 7.7: Josephson junction array fabricated on a BST thin film. **(a)** SEM images of the array. The islands have a diameter of 150 nm and the distance between the edges of two islands is 50 nm, so that the lattice constant $a = 200$ nm for the JJA. **(b)** Frustration factor measurements. The increase in $I_c(B)$ for specific values of the magnetic field are visible, but much weaker compared to the data of Figs. 7.1 and 7.2.

are used to extract a coherence length of only 10 nm, which is an order of magnitude smaller than the (ballistic) coherence length found for BSTS devices [160]. Magnetotransport measurements indicate that transport is likely mediated through bulk and surface states.

The small coherence length observed in the BST thin films puts a limit to the distance between the junctions and thus requires an improved fabrication process, but the use of thin films allows us to create larger arrays, which can lead to a larger critical current and to the observation of more oscillation periods before $I_c(B)$ decreases significantly, as discussed in Sec. 7.2. Furthermore, the use of proximity effect correction for the latest devices has improved the overall quality and homogeneity of the array, as shown in Fig. 7.7(a). Here, we fabricated a JJA with 50×50 islands that contains a hole of 30×30. The islands have a diameter of 150 nm and the distance between the edges of two islands is 50 nm (comparable to the single junction of Sec. 7.3) so that the lattice constant $a = 200$ nm. In Fig. 7.7(b) we show the measurement results of the device when subjected to large magnetic fields. The increase of the critical current for specific frustration factors (such as $f = 1$ for which $\Delta B = 52$ mT) can be observed, but is much weaker than previous observations in the reference and BSTS devices of Sec. 7.2. The fact that the SEM images suggest that we have fabricated a high quality array with homogeneous islands throughout the entire array, means that the poor response of the frustration factor measurement lies within the BST film. We expect that the inhomogeneous current distribution of the film, as was confirmed by the $I_c(B)$ and $I_c(T)$ measurements of the single junction, diminish the collective effects of the entire Josephson junction array. In addition, measurements on a small range of magnetic fields show no clear oscillations with well-defined periods. This work suggests that the film quality needs to be improved for a suitable detection of interference effects in these type of Josephson junction arrays.

Appendix: Numerical simulations

To verify the measurements, simulations on JJA were performed by the simulation package *JJAsim* developed by Lankhorst [176]. These simulations are based on the Resistively Capacitance Shunted Junction (RSCJ) model. The array is modeled by j single junctions, for which

$$I_j = I_{c_j} \sin(\varphi_j) + \frac{\hbar}{2eR_j} \frac{\partial \varphi_j}{\partial t} + \frac{\hbar C_j}{2e} \frac{\partial^2 \varphi_j}{\partial^2 t} + \eta_j(T), \tag{A.1}$$

$$V_j = \frac{\hbar}{2e} \frac{\partial \varphi_j}{\partial t} + \sum_{j' \in J} L_{j,j'} \frac{\partial I_{j'}}{\partial t}. \tag{A.2}$$

Here, I_j is the current through junction j, I_{c_j} the critical current of junction j, φ_j the phase difference of the junction, R_j the resistance of the junction, C_j represents the capacitance of junction j and $\eta_j(T)$ is the temperature dependent noise realization. In Eqn. A.2, $L_{j,j'}$ is the inductance matrix with self-inductance on the diagonal and mutual inductance off the diagonal. The dynamics of a JJA of j junctions, are described by the Kirchhoff's current law, Eqn. A.3, and a Kirchhoff's law of voltage Eqn. A.4. The voltage is rewritten as gauge-invariant phase differences, where the integration constant of the time-integral does not necessary vanish.

$$\sum_{\substack{n \in N \\ j \in J}} M_{n,j} I_j + I_n^{\text{ext}} = 0, \tag{A.3}$$

$$\sum_{j \in P} A_{P,j} \varphi_j = 2\pi \left(z_P - \frac{\Phi_P}{\Phi_0} \right). \tag{A.4}$$

Here we denote J as the set of junctions in the array and N as the set of superconducting islands in the array. $M_{n,j}$ describes the current law through every island, such that $M_{n,j} I_j$ describes the current through island n from junction j. I_n^{ext} represents the external bias current applied to island n. Eqn. A.4 describes the phase winding rule, as it sums over the gauge invariant phase differences along a closed path, P. Here, $A_{P,j} = 1$, if junction j is traversed by path P and 0 otherwise. As a phase change of 2π to any junction does not change the physical solution, the Kirchhoff's law of current and voltage must be invariant. The Kirchhoff's law of current is 2π-periodic. The phase zone, z_P, is introduced to make the Kirchhoff's law of voltage 2π-periodic. The phase zone, z_P is a set of arbitrary integers, which allows to solve another instance of φ_j. Lastly, Φ_P is the flux through the closed path, P and Φ_0 is a flux quantum. Note that the topological effects are not taken into account for any of the simulations performed. All quantities in this simulation package are dimensionless.

Chapter 8

Concluding remarks

Throughout this thesis we have performed different experiments in search of the topological magnetoelectric effect. In this chapter, we look back at the results of the presented experiments. In the broader scope of this chapter, we also look at possible directions for future studies.

8.1 Conclusions

In the first chapter of this thesis we set out a path to search for the topological magnetoelectric effect. The field theoretical description of the TME has led to several experiments that use distinct materials and techniques to probe different parts of the modified Maxwell's equations. While the experiments have been set out in detail, the requirements for the TME to manifest itself are still unclear. For example, the proposals to measure the TME through the spatial gradient in the axion angle consider only a single surface of a topological insulator, while realistic materials (both flakes and thin films) have two surfaces that can contribute constructively or destructively in their response to the TME. With no clear consensus in the field on the requirements for the observation of the TME, we believe that experiments are crucial in resolving the discrepancies between current experimental observations and theory, and because of that reason we prepared a set of experiments in the rest of this thesis.

In order to study the topological magnetoelectric effect, we deposited thin films of (magnetic) topological insulators on a variety of substrates. Structural characterization confirms the high quality of the deposited materials. We developed fabrication methods to fabricate devices with top gates and devices with Josephson junctions and arrays. Magnetotransport measurements on gate-tunable $(\mathrm{Bi}_{1-x}\mathrm{Sb}_x)_2\mathrm{Te}_3$ thin films have shown that we have excellent control of the electronic properties of the material, and hallmark features, such as a Dirac point in the longitudinal resistance, the change in carrier type in measurements in magnetic field and the presence of weak anti-localization, have been observed in our films. Adding a magnetic dopant to the films paves the way to observe the quantum anomalous Hall effect, which has not been observed in our current films. However, we did gain insight into the magnetic properties of the film that are of importance for the axion-related experiments. The deposited films of both BST and V-BST thus provide a good basis for the search of the topological magnetoelectric effect.

Three experiments have been carried out to measure signatures of the topological magnetoelectric effect. Signatures of the chiral magnetic effect, related to the temporal gradient of the axion angle in Weyl semimetals, were found in structured devices of the Dirac semimetal $\mathrm{Bi}_{0.97}\mathrm{Sb}_{0.03}$. Here, we measured the effect in a non-local setup to ensure that the observed negative magnetoresistance is not caused by conventional effects such as current jetting, and we therefore strongly believe that the measured magnetoresistance is induced by the special $\mathbf{E} \cdot \mathbf{B}$ coupling of axion electrodynamics.

In addition, the standard magnetotransport measurements show no ferroelectric or ferromagnetic behavior, and hence the measured magnetoelectric coupling does not originate from multiferroicity in the material.

The other experiments, regarding the monopole detecting with a flip-chip SQUID setup and the interference of fractional charges in a Josephson junction array, consider spatial gradients of the axion angle. In both experiments, no signature of the topological magnetoelectric effect were observed. There are two possible reasons for this: either the theory is incorrect, or our experiments are unable to provide definitive proof for the presence or absence of the TME. For both experiments, we believe that the latter is currently true. For the monopole experiment, we believe that the material needs to be improved, such that for V-BST, the measurement can be executed in the QAH state. Our experiment shows that operating a SQUID in a dilution refrigerator is possible, but that combining transport measurements with SQUID measurements must be performed carefully to make sure that Joule heating effects are taken into account in the analysis. The phase interference experiments on the JJA devices show that clear oscillations are present in the critical current as function of the applied magnetic field, which can be modeled accurately with a RCSJ-model when a prefactor in the effective area is considered. The fact that just a few oscillations were resolved, makes it difficult to attribute the absence of the TME to the limited device size or to the cancellation of the effect on both surfaces of the TI. We present first steps to resolve the former by fabricating JJA devices on thin films of BST, but show that the inhomogeneity of the critical current, in addition to the small coherence length, put additional limitations on the experimental realization of the TME in a JJA setup.

8.2 Perspectives

In the preceding section we already discussed the improvements of the experiments regarding the spatial gradient in the axion angle by improving either the film quality and properties or by optimizing the device layout. In this section, we consider a broader outlook where we also consider materials which have not been investigated or used in this work, but which can be relevant for future experiments as well.

We first consider the monopole experiment. As discussed before, we believe that the QAH state (or even the axion insulator state, depending on possible cancellation of the contributions of the different surfaces) is important in finding the answer to whether the topological magnetoelectric effect can be measured or not. We also have seen that the existence of axion insulators is under debate, and that even QAH systems are regarded to be ideal for axion electrodynamics, but only when they are 3D systems [31]. We propose that the monopole experiment can provide more insight into this open question. By preparing a set of QAH films with different thicknesses, we have access to both '2D' and '3D' QAH samples. By using the flip-chip SQUID, we can measure the response for every device. If we measure a response in all samples, both the 2D and 3D QAH systems exhibit the TME and the different flow of $\sigma_{\mathrm{xx}}(\sigma_{\mathrm{xy}})$ that was considered in Ref. [31] does not alter the axion physics. If the TME is only present for the thicker films, this would directly confirm the difference between the two. If the effect is absent in both cases, the experiment could be performed on axion insulator devices, provided that either the coercive fields are lowered considerably, so that the magnet current can be driven by a Keithley SMU (such as in Sec. 7.2), or that the stability of the supply current for the magnet can be improved such that the SQUID can operate reliably under applied field.

The challenge of the monopole experiment is twofold: next to the requirements for the materials, as discussed in the previous section, the extremely low temperature required for the experiment brings additional challenges, as we have seen in Chapter 6. Over the past few years, efforts have been made to increase the temperature at which the QAH state can be observed. Magnetic modulation doping, where heterostructures of heavily doped Cr-BST layers that sandwich a normal BST layer are deposited by MBE, leads to an increased temperature of 2 K [114] and seems to be the most promising method to enhance the temperature limit in V- or Cr-based films. More recently, the QAH was also observed in intrinsic septuple-layer $\mathrm{MnBi_2Te_4}$ single crystals [115], where a fully quantized platform was reported up to 1.4 K without applied field, and even 6.5 K under applied field. The material can be an interesting alternative to the V- or Cr-based films, as we believe that intrinsic ordering of magnetic atoms will likely lead to more homogeneous and more reproducible results. Provided that both materials (either Cr- or V- modulation doped BST films or $\mathrm{MnBi_2Te_4}$ films) are suitable for the detection of the monopole experiment[1], the measurements could be performed in different cryostats, such as cryostats with a ^{3}He insert, which provides a stable temperature of 300 mK and thus eliminates the sample's Joule heating problem of the dilution refrigerator setup.

Lastly, we want to point out that a new class of materials has been in-

---

[1] The modulation doped samples are again layered systems and therefore the question would be whether these would be classified as '2D' or '3D', as discussed above.

vestigated for their topological (magnetoelectric) properties as well. Rather than synthesizing ferromagnetic topological insulators (such as for the QAH systems), the focus has been to create antiferromagnetic topological insulators. The antiferromagnetic state was predicted to also occur in $MnBi_2Te_4$ [177]. Although an odd number of septuple layers can lead to the QAH state as observed in Ref. [115], an axion insulator state was reported for an even number of layers [62]. This makes the intrinsic material an even more interesting candidate for axion-related physics, as both QAH and axion states could be observed within the same material. While current work on the material is all based on single crystals [62, 115, 178–180], manganese can be incorporated into molecular beam epitaxy systems in a standard effusion cell and as such it would be interesting to deposit thin films of the material as well. We should note that extensive studies are required for the optimization of the layer thickness, which for this system seems to be even more critical.

Summary

We started our search for the topological magnetoelectric effect in **Chapter 2** by reviewing the theoretical aspects of axion electrodynamics in topological matter. It was found that for such materials, an additional term can be added to the Lagrangian density, which leads to the modification of Maxwell's equations. These modifications arise due to spatial or temporal changes in the axion angle, which is non-zero in topological materials. Several experiments have been proposed to measure the resulting topological magnetoelectric effects, of which we consider three experiments which are related to electronic properties. Two experiments, the search for the magnetic monopole and the interference experiment for fractional charge, are related to a spatial gradient in the axion angle, while the chiral magnetic effect relates to temporal changes in the axion angle of Weyl semimetals. We discussed some points of concern regarding the contributions of different surfaces, the requirements regarding the direction of magnetization at the surfaces, the axion insulator state and optical experiments. We noted that more experimental proof is required to clarify these points.

In order to study these topological effects, we make use of different topological insulator materials. While part of the research is performed on devices that were fabricated on exfoliated flakes of single crystals, the more recent experiments focus on thin films of topological insulators that were deposited by molecular beam epitaxy. We have deposited high quality films of $(\mathrm{Bi}_{1-x}\mathrm{Sb}_x)_2\mathrm{Te}_3$ on SrTiO_3, $\mathrm{Al}_2\mathrm{O}_3$, and InP substrates, as shown in **Chapter 3**. While misoriented crystals are present in films grown on SrTiO_3 and $\mathrm{Al}_2\mathrm{O}_3$, they are absent for films grown on InP. We develop fabrication methods that allow us to fabricate top-gated devices of different shapes and enable us to create Josephson junctions and arrays on topological films that are deposited on one of the aforementioned substrates. The magnetotransport measurements on the BST films show that, upon applying gate voltages, the material can be tuned through the Dirac point, and both the associated peak in the longitudinal resistance, as well as the change in (dominant) carrier type are observed in the films. We furthermore show that the films deposited on SrTiO_3 can be tuned by both top and back gates, where a strong interlayer coupling was found between the two surfaces. At low temperatures, the fabricated junctions do not turn superconducting, but signs of electron-electron interactions are present in both junctions and Hall bar devices.

In **Chapter 4** we incorporated vanadium dopants into the BST films. The resulting magnetic topological insulator thin films have been shown elsewhere to exhibit a quantum anomalous Hall state when the doping is optimized and when subsequently the Fermi level is tuned into the gap. Despite the high quality of our films, no QAH state was observed so far. Nevertheless, the films have provided a valuable insight into the magnetism of the MTI films. While both Van Vleck and RKKY magnetism are observed in telluride materials that are doped with either vanadium or chromium, our gate-dependent Arrott analysis shows that the Curie temperature does not change as a function of gate voltage. The Curie temperature does increase when the vanadium content is increased, as was confirmed in a different set of samples. Both observations strongly point towards the Van Vleck mechanism as dominant contribution to the magnetism in our films. We discuss possible explanations for not observing a QAH state in our films and also discuss recent developments regarding the ‘2D’ and ‘3D’ versions of the QAH effect.

We studied the chiral magnetic effect in the Dirac semimetal $Bi_{0.97}Sb_{0.03}$ in **Chapter 5**. The chiral magnetic effect, leading to a negative magnetoresistance when the applied electric and magnetic fields are parallel, can hardly be distinguished from other effects that lead to a similar response, such as current jetting. To resolve this problem, we fabricated nanodevices on exfoliated flakes of $Bi_{0.97}Sb_{0.03}$. In a non-local measurement setup, we locally apply parallel electric and magnetic fields, which leads to a chiral charge polarization. This polarization diffuses into the rest of the nanodevice, where it couples to the magnetic field to lead to a measurable voltage. By measuring the voltage at different distances, we were able to extract a chiral charge diffusion length of 1 μm. The temperature dependence of the diffusion length indicates that the relaxation of chiral charges mainly occurs through inelastic processes.

We integrated a superconducting quantum interference device in a dilution refrigerator in **Chapter 6** to measure the modulation of flux as a consequence of changing the electric field at the surface of a magnetic topological insulator at temperatures of 20 mK. We verified the working of the SQUID sensor by using a test setup in the refrigerator. Upon measuring the gate dependence of the detected flux of both axion devices and top-gated Hall bar devices that were fabricated on V-BST thin films, we found no sign of a topological magnetoelectric effect. We argue that either the non-quantized anomalous Hall state of the V-BST sample is not sufficient for the observation of the TME, or that, if present, the signal may still be too weak. By simultaneously performing electrical transport measurements, we show that sample heating influences the magnetization of the magnetic topological insulator film, which is reflected in the SQUID measurements. It is thus of importance for future measurements to be able to distinguish any temperature-induced effects from possible topological magnetoelectric effects.

In **Chapter 7** we fabricated Josephson junction devices on topological materials in search for fractional charges. We started with Josephson junction arrays that contain a hole on exfoliated flakes of $BiSbTeSe_2$ and also fabricated reference samples on Au thin films. In magnetotransport measurements we observe an oscillation in the critical current as function of the magnetic field, which was reproduced by simulations on similar geometries, where a prefactor was introduced for the effective area corresponding to the oscillations. No contributions from fractional charge were observed in the topological insulator device. While several reasons for this were given, we focus on the limited number of observed oscillations and therefore seek to improve this by making the transition to thin film devices. We first fabricate Josephson junctions and find that the supercurrent distribution is inhomogeneous in the junctions. The coherence length was found to be 10 nm, which puts a limit to the lattice constant of the Josephson junction array. A first Josephson junction array on a thin film shows that the homogeneity of the supercurrent distribution needs to be improved in order to observe the desired amount of oscillations.

Samenvatting

We zijn onze zoektocht naar het topologische magnetoelektrische effect gestart in **Hoofdstuk 2** door de theoretische aspecten van axionische elektrodynamica in topologische materialen te beschouwen. Voor zulke topologische materialen was gevonden dat een additionele term in de Langrangiaanse dichtheid kan worden toegevoegd, die vervolgens leidt tot aanpassingen aan Maxwell's vergelijkingen. Deze aanpassingen onstaan door spatiële en temporale veranderingen in de de axion parameter die een andere waarde dan nul heeft in topologische materialen. Er zijn verschillende experimenten voorgesteld om de resulterende topologische magnetoelektrische effecten te meten, waarvan wij er hier drie beschouwen die te maken hebben met de elektronische eigenschappen van de materialen. Twee experimenten hiervan, de zoektocht naar een magnetische monopool en het interferentie effect voor fractionele lading, zijn gerelateerd aan de spatiële gradiënt van de axion parameter, terwijl het chirale magnetische effect gerelateerd is aan de temporale veranderingen in de axion parameter van Weyl semimetalen. We hebben een aantal aandachtspunten met betrekking tot de theorie bediscussieerd, zoals de bijdrages van de verschillende oppervlaktetoestanden, de vereisten voor de richting van de magnetisatie van de verschillende oppervlaktes, de axionische isolatortoestand en optische experimenten. We hebben opgemerkt dat meer experimenteel bewijs nodig is om deze aandachtspunten op te helderen.

Om deze topologische effecten te kunnen bestuderen maken we gebruik van verschillende topologische isolatoren. Hoewel een deel van dit onderzoek is uitgevoerd met nanostructuren die gefabriceerd zijn op geëxfolieerde kristallen van éénkristallen, zijn de meer recente experimenten uitgevoerd op dunne lagen van topologische isolatoren waarvan epitaxiale lagen zijn gedeponeerd door middel van moleculaire bundels. In **Hoofdstuk 3** laten we zien dat we dunne lagen van $(Bi_{1-x}Sb_x)_2Te_3$ (BST) met een hoge kwaliteit hebben gedeponeerd op $SrTiO_3$, Al_2O_3 en InP substraten. Hoewel kristallen met een onverwachte oriëntatie waarneembaar zijn in de lagen die zijn gedeponeerd op $SrTiO_3$ en Al_2O_3, zien we dit niet terug in de lagen op InP. We hebben fabricagemethodes ontwikkeld die ons in staat stellen om structuren te maken die lijken op een veldeffecttransistor, waarbij we een diëlektricum en goudlaag deponeren op de eerder gedeponeerde dunne laag, en waarmee we Josephson verbindingen en patronen van Josephson verbindingen kunnen deponeren op de dunne lagen. De magnetotransport metingen op de BST films laten zien dat het aanbrengen van een elektrisch veld, door gebruik te maken van de gefabriceerde veldeffecttransistorstructuur, ons in staat stelt om de materiaaleigenschappen zo te beïnvloeden dat het Dirac punt bereikt en gepasseerd kan worden, wat we terugzien in een maximum in de longitudinale weerstand als functie van het aangebrachte elektrisch veld, samen met een verandering van het dominante ladingsdragertype. We laten verder zien dat een veldeffect kan worden bereikt met zowel de toplaag van goud, alsook met een elektrode aan de onderzijde van een $SrTiO_3$ substraat, waarbij het substraat de rol van diëlektricum vervult. Beide elektrodes zijn in staat om de transporteigenschappen van de gehele dunne laag van BST zo te beïnvloeden dat we concluderen dat er een sterke koppeling tussen de twee oppervlaktes van de laag bestaat. Verder zien we op lage temperaturen dat gefabriceerde Josephson verbindingen op $SrTiO_3$ substraten niet supergeleidend worden, maar dat ze tekenen van interacties tussen elektronen vertonen, die we terugzien in zowel Josephson verbindingen en Hall bar structuren.

In **Hoofdstuk 4** introduceren we vanadium als dotering in onze dunne lagen van BST. Elders is aangetoond dat de resulterende magnetische topologische isolator (MTI) een gekwantiseerde versie van het abnormale Hall effect (QAH) kan laten zien wanneer de dotering geoptimaliseerd is en wanneer bovendien het Fermi niveau in de bandkloof is gebracht. Hoewel onze gedeponeerde dunne lagen van hoge kwaliteit zijn hebben wij deze QAH toestand nog niet waargenomen. Desalniettemin geven de lagen ons wel waardevol inzicht in de rol van het magnetisme in deze MTI lagen. Hoewel zowel het Van Vleck en RKKY magnetisme geobserveerd zijn in telluurgebaseerde materialen die gedoteerd zijn met ofwel vanadium of chromium, laat onze elektrisch veldafhankelijke Arrott analyse zien dat de Curie temperatuur niet afhangt van het aangebrachte elektrisch veld. De Curie temperatuur neemt wel toe wanneer de mate van dotering toeneemt, wat we bevestigen in een andere set van dunne lagen. Beide observaties wijzen sterk in de richting van Van Vleck magnetisme als de dominante bijdrage van het magnetisme in onze dunne lagen. Tot slot bediscussiëren we verschillende redenen voor het niet observeren van de QAH toestand in onze lagen, en we beschouwen ook recente ontwikkelingen met betrekking tot de ‘2D’ en ‘3D’ versies van het QAH effect.

We bestuderen het chiraal magnetische effect in het Dirac semimetaal $Bi_{0.97}Sb_{0.03}$ in **Hoofdstuk 5**. Het chiraal magnetische effect, dat leidt tot een negatieve magnetoweerstand wanneer de aangebrachte elektrische en magnetische velden parallel zijn aan elkaar, is lastig te onderscheiden van andere effecten die leiden tot een vergelijkbare resultaten, zoals bijvoorbeeld het focusseren van het stroompad. Om aan te tonen dat onze resultaten enkel ten gevolge zijn van het chiraal magnetische effect hebben we nanostructuren gemaakt op geëxfolieerde vlokken van $Bi_{0.97}Sb_{0.03}$. In een niet-lokale meetopstelling brengen we lokaal parallelle elektrische en magnetische velden aan, wat leidt tot een polarisatie van de chirale lading. Deze polarisatie diffundeert vervolgens door de rest van de nanostructuur, waar het koppelt aan het magnetische veld om zo voor een meetbare potentiaal te zorgen. Door deze potentiaal op verschillende afstanden van de lokale bron te meten konden we deduceren dat de chirale lading diffundeert over een lengteschaal van 1 μm. De temperatuurafhankelijkheid van deze diffusielengte geeft aan dat de chirale lading voornamelijk relaxeert via inelastische processen.

In **Hoofdstuk 6** integreren we een supergeleidend kwantum interferentie apparaat (SQUID) in een mengkoeler om de modulatie van de flux ten gevolge van een veranderd elektrisch veld aan het oppervlak van een magnetische topologische isolator te meten op een temperatuur van 20 mK. We hebben eerst geverifieerd dat de SQUID sensor werkt door een test uit te voeren in de koeler. Vervolgens, tijdens het moduleren van het elektrisch veld op bovengenoemde MTI structuren via veldeffecttransistorstructuren en axion structuren, werd geen teken van een topologisch magnetoelektrische bijdrage gevonden in het gemeten signaal. We beargumenteren dat de afwezigheid van het topologisch magnetoelektrische effect verklaard kan worden door ofwel het niet hebben van een QAH toestand in de huidige V-BST lagen, ofwel dat het effect te zwak is om waargenomen te worden. Door tegelijkertijd elektronische transportmetingen uit te voeren op de MTI lagen laten we zien dat dissipatie de magnetisatie van de dunne laag beïnvloedt, wat duidelijk naar voren komt uit de SQUID metingen. Het is dus van groot belang voor toekomstige metingen om elke temperatuurgerelateerde bijdrage te onderscheiden van een mogelijke topologisch magnetoelektrische bijdrage.

In onze zoektocht naar fractionele ladingen hebben we in **Hoofdstuk 7** structuren met Josephson verbindingen gefabriceerd op topologische materialen. We begonnen met patronen van Josephson verbindingen, die een gat in het midden bevatten, op geëxfolieerde vlokken van $BiSbTeSe_2$. Daarnaast zijn controlestructuren gefabriceerd op dunne lagen van goud. In magnetotransport metingen zien we een oscillatie in de kritische stroom als functie van een aangelegd magneetveld, wat gereproduceerd is in simulaties die uitgevoerd zijn op vergelijkbare geometrieën ten opzichte van de gefabriceerde nanostructuren. De conversie van de dimensieloze eenheden naar reële dimensies vereist het gebruik van een additionele voorfactor die tot een effectieve oppervlakte leidt. Er zijn geen contributies van fractionele lading gevonden in de nanostructuur die gefabriceerd is op een TI. Hoewel we meerdere redenen noemen voor de afwezigheid hiervan, focusseren we op het beperkte aantal observeerbare oscillaties. We trachten het aantal oscillaties te vergroten door de nanostructuren op dunne lagen te fabriceren, waarvoor we eerst Josephson verbindingen op deze lagen maken. Middels deze verbindingen leren we dat de distributie van de superstroom inhomogeen is in de verbinding, en dat de coherentielengte 10 nm is, wat een limiet geeft voor de roosterconstante van patronen van Josephson verbindingen op zulke dunne lagen. Een eerste reeks op een dunne laag laat zien dat de homogeniteit van de superstroom eerst verbeterd moet worden om het gewenste aantal oscillaties te kunnen waarnemen.

Dankwoord

Nadat ik een half uur geleden uit het vliegtuig ben gestapt na een conferentie en nu in de trein zit richting Enschede, de stad waar ik negen jaar geleden begon met studeren, begin ik met het schrijven van mijn dankwoord. Want, de resultaten in dit proefschrift waren nooit tot stand gekomen zonder de hulp en bijdragen van vele mensen die ik graag allemaal hier persoonlijk voor wil bedanken.

Ten eerste wil ik graag **Alexander** bedanken. In 2015 klopte ik samen met Luca bij je deur aan voor een bacheloropdracht. Het enthousiasme waarmee jij een mogelijke opdracht voor ons schetste maakte dat ik hier erg graag mee aan de slag wilde gaan. Wie had destijds gedacht dat ik in mijn proefschrift me nog veel dieper in hetzelfde onderwerp zou storten? Jouw enthousiasme en het vermogen om gecompliceerde natuurkundige problemen op een toegankelijke manier uit te leggen heb ik elke keer als heel prettig ervaren, en ik weet zeker dat het enorm bijdraagt aan de fijne sfeer binnen de groep. Ik kijk er erg naar uit om na mijn promotie nog bij de groep te blijven waarin we ongetwijfeld veel mooie fysica gaan uitpluizen.

While my train stops at Amersfoort Centraal, I would also like to thank the person that lives opposite of that specific train station and likes to rather take the train to Utrecht CS instead of walking a few minutes to the shopping center in Amersfoort itself. **Chuan**, thank you for the countless discussions that we had. I genuinely love how our discussions cover a great variety of subjects, while always revolving around the core of physics. Your knowledge of both theoretical and experimental physics is something I deeply admire. I also greatly acknowledge our personal friendship and am still very honored that I have been a witness at your marriage.

Frank, ik wil jou heel erg bedanken voor al het werk binnen en buiten het lab dat ons in staat stelt om onderzoek te doen. Je bent altijd bereid om te helpen, en zorgt er (soms met het nodige gevloek) altijd voor dat alles weer werkt als er weer iets mis is gegaan. Ik ben verder ook erg dankbaar voor het feit dat, hoewel ik vorig jaar al met je samen ging werken op technisch vlak, je me altijd de ruimte hebt gegeven om mijn proefschrift te voltooien, en ik bewonder het dan ook enorm hoe je met mijn mindere beschikbaarheid alsnog alles klaar weet te spelen. Ik kijk er ook naar uit om verder met jou samen te werken (en ja, ik zal binnenkort echt bij je op kantoor intrekken).

Dick, hoewel jij een jaar geleden met pensioen bent gegaan wil ik je toch bedanken voor de afgelopen vier jaren, dus inclusief het laatste jaar. In de eerste jaren omdat je het vaste duo met Frank vormde en onze laboratoria draaiende hield, maar in de laatste jaren ook vooral voor de kennisoverdacht, het vele werk aan de Triton om de integratie van de SQUID mogelijk te maken, en ook na je pensioen nog je uitgebreide antwoorden op vragen die ik nog aan je stelde.

Al vroeg in mijn studie kwam **Luca** op mijn pad. We hebben talloze vakken samen doorlopen en ook onze bacheloropdracht samen gedaan. Hoewel we op natuurkundig vlak elkaar goed konden vinden en aanvullen, ben ik zeker net zo blij met onze vriendschap die we hebben opgebouwd. Waar mijn bewondering (of eigenlijk meer verwondering) voor jou eerst vooral nog bestond voor hoe jij na talloze avonden met je dispuut, jaarclub of vereniging in de kroeg toch altijd weer scherp op in de collegebanken zat, veranderde dit later naar de bewondering van hoe je je buiten je studie en promotietraject altijd breed inzet voor allerlei mooie initiatieven. Je bent enorm gedreven, en ik weet zeker dat jouw natuurkundige en sociale talenten je nog heel ver gaan brengen.

Liesbeth, ik wil jou graag bedanken voor je oneindige doorzettingsvermogen en het feit dat jij altijd bereid was om iedereen te helpen, of het nou om natuurkunde of andere dingen ging. Je aanwezigheid heeft altijd een positieve uitwerking op de gehele groep, en de vraag “Heb je Liesbeth toevallig al gezien?” wordt niet voor niets vaak gesteld wanneer je eens een dagje niet aanwezig bent. Ik vind het bijzonder knap dat je, naast je toewijding aan de natuurkunde, ook nog een aerial silk school hebt, waar je in de avonden ook erg druk mee bent.

Erik, **Sergi**, **Tess**, **Julia**, **Rik** en **Tjerk**, ik ben erg dankbaar voor het feit dat jullie samen met mij allerlei avontuurlijke projecten zijn aangegaan waarin ik jullie dagelijks mocht begeleiden. Ik heb genoten van jullie enthousiasme, nieuwsgierigheid en kundigheid, die stuk voor stuk hebben bijgedragen aan dit proefschrift.

Omar, thank you for being part of the MBE adventure and for all your help and discussions. While I could not get used to the Mexican candy, for which it seemed that you had an endless supply of it, I really enjoyed having you in my office.

Daniel, when you joined the group you immediately brought a lot of knowledge on nanostructures and junctions to our MBE team. While figuring out a procedure for e-beam lithography on our films often came with frustrations, I genuinely loved how we were solving many puzzles in the cleanroom to get everything up and running.

Hoewel mijn promotietraject tegelijk plaats heeft gevonden met die van Luca en Liesbeth heb ik ook veel overlap gehad met de vorige generatie, waardoor ik ze nog altijd als een groot onderdeel van mijn huidige tijd binnen de groep beschouw. Ik wil Jorrit, Joris, Sander, Pim, Bob en Martijn dan ook graag bedanken voor deze erg fijne tijd. **Jorrit**, ik weet nog goed hoe ik op dag twee van mijn masteropdracht een eigen NERF-gun heb moeten kopen om mijzelf te kunnen verdedigen terwijl ik je kantoor binnenliep om een vraag te stellen over natuurkunde. Het project dat we destijds begonnen en later hebben afgerond was een prachtig avontuur dat zich zeker niet liet limiteren tot kantoortijden. Integendeel, discussies in de avonduren (al dan niet in een kroeg) konden rustig gaan over hoe allerlei natuurkundige fenomenen zich nou precies zouden gedragen. Jouw enthousiasme (maar ook “kritische” blik op zo ongeveer alles dat er gebeurde) heeft er mede tot bijgedragen dat ik graag wilde promoveren. Al was het alleen al zodat je me nog wat langer af kon zeiken.

Wanneer je Jorrit zegt, kun je niet anders dan daarna Joris zeggen. **Joris**, ik wil jou graag bedanken voor je vrolijkheid en enthousiasme waarmee je altijd in het lab bezig was, of dat nou voor jezelf was of omdat je weer iemand anders aan het helpen was. Je stond altijd voor iedereen klaar en maakte zo ook onze bacheloropdracht een prachtig avontuur. Zelfs na jouw PhD schroomde je niet me uit de brand te helpen met RAM geheugen voor mijn computer of een 3D-printer knutselwerkje voor mijn Switch. Ik ben blij dat ik jou heb mogen helpen met Python en ik hoop dat je binnenkort Ganon ook zult verslaan.

Sander, jouw gedrevenheid en passie voor de natuurkunde zijn heel sterk vertegenwoordigd. Je had er geen probleem mee om terwijl ik mijn jas pakte na een lange werkdag nog even een Origin project met tientallen figuren te openen om dan in uiterst detail te gaan uitleggen wat je had gemeten en waarom dat zo gaaf was. Hoewel ik eerlijk moet bekennen dat mijn concentratie hierbij wel eens afdwaalde, vond (en vind) ik jou een prachtig voorbeeld van een gepassioneerde wetenschapper.

Pim, **Bob** en **Martijn**, jullie waren ook vanaf het begin van mijn bachelorproject bij ICE aanwezig en hebben altijd voor veel gezelligheid in de groep gezorgd. Een bijkomend wekelijks hoogtepunt was de ICE band, waar jullie deel van uitmaakten. Ik vond het elke week weer leuk om met jullie samen de studio in te duiken en een breed scala aan muziek te spelen!

Nu ik zelf ook onderhand bij de oudere generatie hoor maak ik ook graag plaats voor de nieuwe garde. **Xing**, **Zhen**, **Thies**, **Femke**, **Maarten** en Sofie (en ja, ze is met opzet nog niet dikgedrukt). Xing and Zhen, thank you for the positive vibes that you always bring to the office. Thies, bedankt voor jouw humor die soms net zo droog(gelegd) is als het (Flevo)land waar je vandaan komt. Femke, ik vind het erg leuk dat ik zowel bij je introductie als bij je promotie aanwezig mag zijn! Maarten, met je passie voor zeilen, muziek en spelletjes ben ik er zeker van dat de komende jaren nog zeker erg gezellig zullen zijn. Ik hoop dat we snel weer een ICE band kunnen opzetten!

I also want to thank all colleagues of the ICE / QTM group for all the moments we've shared together, from scientific discussions to flipping canoes in de Bornse Beek, and all the fun activities and conferences in between. I really enjoy the positive mindset of the group and how we do many fun things together. Thank you **Hans**, **Sasha**, **Inanc**, **Jaap**, **Simone**, **Ans**, **Carlos**, **Joost** and all the master and bachelor students for the wonderful time. I am looking forward to keep working with all of you!

Werken op de universiteit gebeurt niet alleen binnen de eigen onderzoeksgroep, en daarom wil ik ook graag nog meer collega's en vrienden bedanken. **Yorick**, bedankt voor je hulp met alle diffractie experimenten en voor je sterke mening die je altijd overal wel voor hebt. **Lisanne**, bedankt voor de gezellige wandelingen en voor het aansporen van het doen van een salto vanaf de duikplank, waarvan de harde klap op het water nog goed in mijn geheugen zit. **Vera**, wij begonnen tegelijkertijd ons promotietraject in twee compleet verschillende richtingen. Ik vond het leuk hoe we elkaar toch konden uitleggen wat we aan het doen waren, en vond het altijd erg gezellig om tijdens de fitness weer bij te praten. **Peter**, bedankt voor je hulp en tijd bij de fabricage van onze dielektrische lagen. Het kalibreren van de lagen is nog steeds erg waardevol en ik ben blij dat we daar samen de eerste stappen in hebben gezet.

Ik wil al mijn vrienden van de band **Headline** bedanken voor alle optredens, repetities, barbecues en sushi-avonden die we al samen hebben gehad. Samen muziek maken is een van mijn favoriete dingen en ik ben blij dat ik het al ruim zes jaar lang samen met jullie mag doen!

Ik wil ook graag mijn sportieve vrienden van **IJSCH**, **Inlineskaters Twente** en **Nightskate Twente** bedanken voor de talloze trainingen, skeelerroutes en andere sportieve activiteiten. Ik hoop dat we samen nog vele kilometers mogen rijden.

Lieke, **Daniek**, **Koen**, **Aniek**, **Nina** en **Jessica**, bedankt dat jullie er altijd voor me zijn en dat jullie de afgelopen jaren vele natuurkundige avonturen van mij hebben aangehoord. We hebben samen al vele mooie momenten beleefd en ik hoop dat er nog lang veel meer momenten zullen volgen.

Ik ben blij dat ik tijdens mijn promotie steun krijg van twee geweldige paranimfen, Linde en Luca. **Linde**, toen jij nog jouw masteropdracht in Enschede deed waren we lange tijd kantoorgenoten en gingen we elke week samen naar de repetitie van de ICE band na een goede maaltijd waarbij jij altijd weer met leuke recepten aan kwam. Ik ben blij dat we na de start van jouw PhD in Cambridge nog bijna elke maand lang met elkaar bellen. Ik zal nooit vergeten hoe we Jorrit op de kast konden jagen nadat we spekkoek meenamen naar kantoor op zijn vrije dag, en hoe jij me er fijntjes aan herinnerde dat je nog een pak vla mee had genomen naar kantoor.

Pap, **mam**, en **Floor**, natuurlijk mogen jullie ook niet ontbreken. Jullie staan altijd voor me klaar, hebben altijd me altijd gesteund in mijn keuzes en waren altijd erg geïnteresseerd in mijn werk. Hoewel ik sinds mijn promotietraject op een iets grotere afstand van jullie woon dan voorheen (procentueel gezien zelfs een enorme verandering) heb ik het gevoel dat we dichter bij elkaar zijn gekomen, en daar ben ik erg dankbaar voor.

Als laatste wil ik **Sofie** bedanken. Ons avontuur startte met jouw afstudeeropdracht in onze groep, en waar mijn promotietraject nu tot een einde komt is die van jou pas net begonnen. Hoewel we beide een sterke passie hebben voor natuurkunde kon ik altijd mijn ei bij jou kwijt over allerlei problemen in het lab, waarbij er soms naast opluchting ook nog een oplossing naar boven kwam. Ik geniet elke keer weer van onze muzikale en sportieve activiteiten waarbij we onze grenzen blijven verleggen en ik kijk uit naar alle volgende avonturen die we samen gaan beleven.

Bibliography

[1] J.B. Carlson, *Science* **189**, 4205, 753-760 (1975).

[2] J.C. Maxwell, *Philosophical Transactions* **155**, 459-512 (1865).

[3] R.D. Peccei, H.R. Quinn, *Physical Review Letters* **38**, 1440 (1977).

[4] J. Preskill, M.B. Wise, F. Wilczek, *Physics Letters B* **120**, 1-3, 127-132 (1983).

[5] A. Arvanitaki, A.A. Geraci, *Physical Review Letters* **113**, 161801 (2014).

[6] L. Zhong, S. Al Kenany, K.M. Backes, B.M. Brubaker, S.B. Cahn, G. Carosi, Y.V. Gurevich, W.F. Kindel, S.K. Lamoreaux, K.W. Lehnert, S.M. Lewis, M. Malnou, R.H. Maruyama, D.A. Palken, N.M. Rapidis, J.R. Root, M. Simanovskaia, T.M. Shokair, D.H. Speller, I. Urdinaran, K.A. van Bibber, *Physical Review D* **97**, 092001 (2018).

[7] J.L. Ouellet, C.P. Salemi, J.W. Foster, R. Henning, Z. Bogorad, J.M. Conrad, J.A. Formaggio, Y. Kahn, J. Minervini, A. Radovinsky, N.L. Rodd, B.R. Safdi, J. Thaler, D. Winklehner, L. Winslow, *Physical Review Letters* **122**, 121802 (2019).

[8] K.M. Backes, D.A. Palken, S. Al Kenany, B.M. Brubaker, S.B. Cahn, A. Droster, G.C. Hilton, S. Ghosh, H. Jackson, S.K. Lamoreaux, A.F. Leder, K.W. Lehnert, S.M. Lewis, M. Malnou, R.H. Maruyama, N.M. Rapidis, M. Simanovskaia, S. Singh, D.H. Speller, I. Urdinaran, L.R. Vale, E.C. van Assendelft, K. van Bibber, H. Wang, *Nature* **590**, 238-242 (2021).

[9] F. Wilczek, *Physical Review Letters* **58**, 1799 (1987).

[10] X.-L. Qi, T.L. Hughes, S.-C. Zhang, *Physical Review B* **78**, 195424 (2008).

[11] D.J.E. Marsh, K.C. Fong, E.W. Lentz, L. Šmejkal, M.N. Ali, *Physical Review Letters* **123**, 121601 (2019).

[12] A. Sekine, K. Nomura, *Journal of Applied Physics* **129**, 141101 (2021).

[13] X.-L. Qi, E. Witten, S.-C. Chang, *Physical Review B* **87**, 134519 (2013).

[14] N.W. Ashcroft, N.D. Mermin, *Solid State Physics* (Brooks/Cole, 1976).

[15] H. Zhang, C.-X. Liu, X.-L. Qi, X. Dai, Z. Fang, S.-C. Zhang, *Nature Physics* **5**, 438-442 (2009).

[16] D. Hsieh, Y. Xia, D. Qian, L. Wray, J.H. Dil, F. Meier, J. Osterwalder, L. Patthey, J.G. Checkelsky, N.P. Ong, A.V. Fedorov, H. Lin, A. Bansil, D. Grauer, Y.S. Hor, R.J. Cava, M.Z. Hasan, *Nature* **460**, 1101-1105 (2009).

[17] M. He, H. Sun, Q.L. He, *Frontiers of Physics* **14**, 43401 (2019).

[18] A. Hirohata, K. Yamada, Y. Nakatani, I.-L. Prejbeanu, B. Diény, P. Pirro, B. Hillebrands, *Journal of Magnetism and Magnetic Materials* **509**, 166711 (2020).

[19] R. Yu, W. Zhang, H.-J. Zhang, S.-C. Zhang, X. Dai, Z. Fang, *Science* **329**, 5987, 61-64 (2010).

[20] C.-Z. Chang, J. Zhang, X. Feng, J. Shen, Z. Zhang, M. Guo, K. Li, Y. Ou, P. Wei, L.-L. Wang, Z.-Q. Ji, Y. Feng, S. Ji, X. Chen, J. Jia, X. Dai, Z. Fang, S.-C. Zhang, K. He, Y. Wang, L. Lu, X.-C. Ma, Q.-K. Xue, *Science* **340**, 6129, 167-170 (2013).

[21] A.C. Mahoney, J.I. Colless, L. Peeters, S.J. Pauka, E.J. Fox, X. Kou, L. Pan, K.L. Wang, D. Goldhaber-Gordon, D.J. Reilly, *Nature Communications* **8**, 1836 (2017).

[22] Q.L. He, L. Pan, A.L. Stern, E.C. Burks, X. Che, G. Yin, J. Wang, B. Lian, Q. Zhou, E.S. Choi, K. Murata, X. Kou, Z. Chen, T. Nie, Q. Shao, Y. Fan, S.-C. Zhang, K. Liu, J. Xia, K.L. Wang, *Science* **357**, 6348, 294-299 (2017).

[23] B. Lian, X.-Q. Sun, A. Vaezi, X.-L. Qi, S.-C. Zhang, *PNAS* **115**, 43, 10938-10942 (2018).

[24] X.-L. Qi, R. Li, J. Zang, S.-C. Zhang, *Science* **323**, 5918, 1184-1187 (2009).

[25] F. Wilczek, *Physical Revieew Letters* **40**, 279 (1978).

[26] F. Wilczek, *Current Contents* **16**, 8 (1991).

[27] M.E. Tobar, B.T. McAllister, M. Goryachev *Physics of the Dark Universe* **26**, 100339 (2019).

[28] Y. Tokura, K. Yasuda, A. Tsukazaki, *Nature Reviews Physics* **1**, 126-143 (2019).

[29] J. Wang, B. Lian, S.-C. Zhang, *Physical Review B* **93**, 045115 (2016).

[30] N.P. Armitage, L. Wu, *SciPost Physics* **6**, 046 (2019).

[31] K.M. Fijalkowski, N. Liu, M. Hartl, M. Winnerlein, P. Mandal, A. Coschizza, A. Fothergill, S. Grauer, S. Schreyeck, K. Brunner, M. Greiter, R. Thomale, C. Gould, L.W. Molenkamp, *Physical Review B* **103**, 235111 (2021).

[32] J.C. Maxwell, *Philosophical Magazine* **90:S1**, 11-23 (1861).

[33] L. Visinelli, *Modern Physics Letters A* **28**, 35, 1350162 (2013).

[34] A.M. Essin, J.E. Moore, D. Vanderbilt, *Physical Review Letters* **102**, 146805 (2009).

[35] D.E. Kharzeev, *Progress in Particle and Nuclear Physics* **75**, 133-151 (2014).

[36] V. Fatemi, B. Hunt, H. Steinberg, S.L. Eltinge, F. Mahmood, N.P. Butch, K. Watanabe, T. Taniguchi, N. Gedik, R.C. Ashoori, P. Jarillo-Herrero, *Physical Review Letters* **113**, 206801 (2014).

[37] S.K. Chong, K.B. Han, T.D. Sparks, V.V. Deshpande, *Physical Review Letters* **123**, 036804 (2019).

[38] P. Reith, *SQUIDs, fits and other magnetic bits*, PhD thesis, University of Twente (2019).

[39] F.S. Nogueira, J. van den Brink, *arXiv* 1808.08825v3 (2020).

[40] F.S. Nogueira, Z. Nussinov, J. van den Brink, *Physical Review Letters* **121**, 227001 (2018).

[41] F.S. Nogueira, Z. Nussinov, J. van den Brink, *Physical Review Letters* **117**, 167002 (2016).

[42] E. Witten, *Physics Letters B* **86**, 3-4, 283-287 (1979).

[43] Y. Wenbin, K.H. Lee, D. Stroud, *Physical Review B* **47**, 5906 (2003).

[44] M.S. Rzchowski, S.P. Benz, M. Tinkham, C.J. Lobb, *Physical Review B* **42**, 2041 (1990).

[45] N.P. Armitage, E.J. Mele, A. Vishwanath, *Reviews of Modern Physics* **90**, 015001 (2018).

[46] M.M. Vazifeh, M. Franz, *Physical Review Letters* **111**, 027201 (2013).

[47] A.A. Burkov, *Physical Review Letters* **113**, 247203 (2014).

[48] H.B. Nielsen, M. Ninomiya, *Physics Letters* **130B**, 6, 389-396 (1983).

[49] S. Adler, *Physical Review* **177**, 2426 (1969).

[50] J.S. Bell, R. Jackiw, *Nuovo Cimento* **60A**, 4 (1969).

[51] Q. Li, D.E. Kharzeev, C. Zhang, Y. Huang, I. Pletikosić, A.V. Fedorov, R.D. Zhong, J.A. Schneeloch, G.D. Gu, T. Valla, *Nature Physics* **12**, 550–554 (2016).

[52] D.T. Son, B.Z. Spivak, *Physical Review B* **88**, 1–4 (2013).

[53] S. Liang, J. Lin, S. Kushwaha, J. Xing, N. Ni, R.J. Cava, N.P. Ong, *Physical Review X* **8**, 031002 (2018).

[54] C. Zhang, E. Zhang, W. Wang, Y. Liu, Z.G. Chen, S. Lu, S. Liang, J. Cao, X. Yuan, L. Tang, Q. Li, C. Zhou, T. Gu, Y. Wu, J. Zou, F. Xiu, *Nature Communications* **8**, 13741 (2017).

[55] B. Cheng, T. Schumann, S. Stemmer, N.P. Armitage, *Science Advances* **7**, 16, eabg0914 (2021).

[56] R. Li, J. Wang, X.-L. Qi, S.-C. Zhang, *Nature Physics* **6**, 284-288 (2010).

[57] Q.N. Meier, M. Fechner, T. Nozaki, M. Sahashi, Z. Salman, T. Prokscha, A. Suter, P. Schoenherr, M. Lilienblum, P. Borisov, I.E. Dzyaloshinskii, M. Fiebig, H. Luetkens, N.A. Spaldin, *Physical Review X* **9**, 011011 (2019).

[58] N.A. Spaldin, M. Fiebig, *Science* **309**, 5733, 391-392 (2005).

[59] M. Mogi, M. Kawamura, R. Yoshimi, A. Tsukazaki, Y. Kozuka, N. Shirakawa, K.S. Takahashi, M. Kawasaki, Y. Tokura, *Nature Materials* **16**, 516-521 (2017).

[60] D. Xiao, J. Jiang, J.-H. Shin, W. Wang, F. Wang, Y.-F. Zhao, C. Liu, W. Wu, M.S.W. Chan, N. Samarth, C.-Z. Chang, *Physical Review Letters* **120**, 056801 (2018).

[61] M. Mogi, M. Kawamura, A. Tsukazaki, R. Yoshimi, K.S. Takahashi, M. Kawasaki, Y. Tokura, *Science Advances* **3**, 10, eaao1669 (2017).

[62] C. Liu, Y. Wang, H. Li, Y. Wu, Y. Li, J. Li, K. He, Y. Xu, J. Zhang, Y. Wang, *Nature Materials* **19**, 522-527 (2020).

[63] S. Grauer, K.M. Fijalkowski, S. Schreyeck, M. Winnerlein, K. Brunner, R. Thomale, C. Gould, L.W. Molenkamp, *Physical Review Letters* **118**, 246801 (2017).

[64] L. Wu, M. Salehi, N. Koirala, J. Moon, S. Oh, N.P. Armitage, *Science* **354**, 6316, 1124-1127 (2016).

[65] K.N. Okada, Y. Takahashi, M. Mogi, R. Yoshimi, A. Tsukazaki, K.S. Takahashi, N. Ogawa, M. Kawasaki, Y. Tokura, *Nature Communications* **7**, 12245 (2016).

[66] C. Beenakker, *Journal Club Condensed Matter Physics, Leiden University* (2016).

[67] D.M. Nenno, C.A.C. Garcia, J. Gooth, C. Felser, P. Narang, *Nature Review Physics* **2**, 682-696 (2020).

[68] D. Hsieh, D. Qian, L. Wray, Y. Xia, Y.S. Hor, R.J. Cava, M.Z. Hasan, *Nature* **452**, 970 (2008).

[69] Y.L. Chen, J.G. Analytis, J.-H. Chu, Z.K. Liu, S.-K. Mo, X.L. Qi, H.J. Zhang, D.H. Lu, X. Dai, Z. Fang, S.C. Zhang, I.R. Fisher, Z. Hussain, Z.-X. Shen, *Science* **325**, 5937, 178-181 (2009).

[70] A. Koma, *Journal of Crystal Growth* **201-202**, 246-241 (1999).

[71] K.S. Novoselov, A.K. Geim, S.V. Morozov, D. Jiang, Y. Zhang, S.V. Dubonos, I.V. Grigorieva, A.A. Firsov, *Science* **306**, 5696, 666-669 (2004).

[72] J. Zhang, C.-Z. Chang, Z. Zhang, J. Wen, X. Feng, K. Li, M. Liu, K. He, L. Wang, X. Chen, Q.-K. Xue, X. Ma, Y. Wang, *Nature Communications* **2**, 574 (2011).

[73] C. Weyrich, M. Drögeler, J. Kampmeier, M. Eschbach, G. Mussler, T. Merzenich, T. Stoica, I.E. Batov, J. Schubert, L. Pluckinski, B. Beschoten, C.M. Schneider, C. Stampfer, D. Grützmacher, T. Schäpers, *Journal of Physics: Condensed Matter* **28**, 495501 (2016).

[74] L. He, X. Kou, K.L. Wang, *Physica Status Solidi RRL* **7**, 1-2, 50-63 (2013).

[75] G. Mussler, *Physica Status Solidi B* 202000007 (2020).

[76] Y.-Y. Li, G. Wang, X.-G. Zhu, M.-H. Liu, C. Ye, X. Chen, Y.-Y. Wang, K. He, L.-L. Wang, X.-C. Ma, H.-J. Zhang, X. Dai, Z. Fang, X.-C. Xie, Y. Liu, X.-L. Qi, J.-F. Jia, S.-C. Zhang, Q.-K. Xue, *Advanced Materials* **22**, 4002-4007 (2010).

[77] A.A. Taskin, S. Sasaki, K. Segawa, Y. Ando, *Physical Review Letters* **109**, 066803 (2012).

[78] S.E. Harrison, S. Li, Y. Huo, B. Zhou, Y.L. Chen, J.S. Harris, *Applied Physics Letters* **102**, 171906 (2013).

[79] P. Ngabonziza, R. Heimbuch, N. de Jong, R.A. Klaassen, M.P. Stehno, M. Snelder, A. Solmaz, S.V. Ramankutty, E. Frantzeskakis, E. van Heumen, G. Koster, M.S. Golden, H.J.W. Zandvliet, A. Brinkman, *Physical Review B* **92**, 035405 (2015).

[80] J. Kellner, M. Eschbach, J. Kampmeier, M. Lanius, E. Młyńczak, G. Mussler, B. Holländer, L. Pluckinski, M. Liebmann, D. Grützmacher, C.M. Schneider, M. Morgenstern, *Applied Physics Letters* **107**, 251603 (2015).

[81] J. Chen, H.J. Qin, F. Yang, J. Liu, T. Guan, F.M. Qu, G.H. Zhang, J.R. Shi, X.C. Xie, C.L. Yang, K.H. Wu, Y.Q. Li, L. Lu, *Physical Review Letters* **105**, 176602 (2010).

[82] G. Zhang, H. Qin, J. Chen, X. He, L. Lu, Y. Li, K. Wu, *Advanced Functional Materials* **21**, 2351-2355 (2011).

[83] X. Guo, Z.J. Xu, H.C. Liu, B. Zhao, X.Q. Dai, H.T. He, J.N. Wang, H.J. Liu, W.K. Ho, M.H. Xie, *Applied Physics Letters* **102**, 151604 (2013).

[84] N.V. Tarakina, S. Schreyeck, T. Borzenko, C. Schumacher, G. Karczewski, K. Brunner, C. Gould, H. Buhmann, L.W. Molenkamp, *Crystal Growth & Design* **12**, 1913-1918 (2012).

[85] S. Gariglio, A. Fête, J.-M. Triscone, *Journal of Physics: Condensed Matter* **27**, 283201 (2015).

[86] G. Koster, B.L. Kropman, A.J.H.M. Rijnders, D.H.A. Blank, H. Rogalla, *Applied Physics Letters* **73**, 2920 (1998).

[87] M. Jourdan, N. Blümer, H. Adrian, *The European Physical Journal B* **33**, 25-30 (2003).

[88] W.M. Lau, R.N.S. Sodhi, S. Ingrey, *Applied Physics Letters* **52**, 386 (1988).

[89] N.V. Tarakina, S. Schreyeck, M. Luysberg, S. Grauer, C. Schumacher, G. Karczewski, K. Brunner, C. Gould, H. Buhmann, R.E. Dunin-Borkowski, L.W. Molenkamp, *Advanced Materials Interfaces* **1**, 1400134 (2014).

[90] M. Lanius, J. Kampmeier, C. Weyrich, S. Kölling, M. Schall, P. Schüffelgen, E. Neumann, M. Luysberg, G. Mussler, P.M. Koenraad, T. Schäpers, D. Grützmacher, *Crystal Growth & Design* **16**, 4, 2057-2061 (2016).

[91] S. Hasegawa, *Reflection High-Energy Electron Diffraction* (John Wiley & Sons, 2012).

[92] I. Levy, T. Axtmann Garcia, S. Shafique, M.C. Tamargo, *Journal of Vacuum Science & Technology B* **36**, 02D107 (2018).

[93] Y. Liu, M. Weinert, L. Li, *Physical Review Letters* **108**, 115501 (2012).

[94] A. Richardella, A. Kandala, J.S. Lee, N. Samarth, *APL Materials* **3**, 083303 (2015).

[95] D.W. Reagor, V.Y. Butko, *Nature Materials* **4**, 593-596 (2005).

[96] F. Yang, A.A. Taskin, S. Sasaki, K. Segawa, Y. Ohno, K. Matsumoto, Y. Ando, *Applied Physics Letters* **104**, 161614 (2014).

[97] S. Datta, *Electronic Transport in Mesoscopic Systems* (Cambridge University Press, 1995).

[98] X. He, T. Guan, X. Wang, B. Feng, P. Cheng, L. Chen, Y. Li, K. Wu, *Applied Physics Letters* **101**, 123111 (2012).

[99] L. Mulder, *Private communications.*

[100] C. Li, B. de Ronde, A. Nikitin, Y. Huang, M.S. Golden, A. de Visser, A. Brinkman, *Physical Review B* **96**, 195427 (2017).

[101] F. Yang, A.A. Taskin, S. Sasaki, K. Segawa, Y. Ohno, K. Matsumoto, Y. Ando, *ACS Nano* **9**, 4, 4050-4055 (2015).

[102] R.C. Neville, B. Hoeneisen, C.A. Mead, *Journal of Applied Physics* **43**, 2124-2131 (1972).

[103] C. Yin, A.E.M. Smink, I. Leermakers, L.M.K. Tang, N. Lebedev, U. Zeitler, W.G. van der Wiel, H. Hilgenkamp, J. Aarts, *Physical Review Letters* **124**, 017702 (2020).

[104] M. Veldhorst, M. Snelder, M. Hoek, C.G. Molenaar, D.P. Leusink, A.A. Golubov, H. Hilgenkamp, A. Brinkman, *Physica Status Solidi RRL* **7**, 1-2, 26-38 (2013).

[105] M. Liu, C.-Z. Chang, Z. Zhang, Y. Zhang, W. Ruan, K. He, L.-L. Wang, X. Chen, J.-F. Jia, S.-C. Zhang, Q.-K. Xue, X. Ma, Y. Wang, *Physical Review B* **83**, 165440 (2011).

[106] V.F. Gantmakher, *Electrons and Disorder in Solids* (Oxford University Press, 2005).

[107] J. Wang, A.M. DaSilva, C.-Z. Chang, K. He, J.K. Jain, N. Samarth, X.-C. Ma, Q.-K. XUe, M.H.W. Chan, *Physical Review B* **83**, 245438 (2011).

[108] P.A. Lee, T.V. Ramakrishnan, *Reviews of Modern Physics* **57**, 2 (1985).

[109] E.H. Hall, *American Journal of Mathematics* **2**, 287-292 (1879).

[110] E.H. Hall, *The London, Edinburgh, and Dublin Philosophical Magazine and Journal of Science* **12:74**, 157-172 (1881).

[111] K. v. Klitzing, G. Dorda, M. Pepper, *Physical Review Letters* **45**, 494 (1980).

[112] C.-Z. Chang, W. Zhao, D. Y. Kim, H. Zhang, B.A. Assaf, D. Heiman, S.-Z. Zhang, C. Liu, M.S.W. Chan, J.S. Moodera, *Nature Materials* **14**, 473-477 (2015).

[113] Y. Ou, C. Liu, G. Jiang, Y. Feng, D. Zhao, W. Wu, X.-X. Wang, W. Li, C. Song, L.-L. Wang, W. Wang, W. Wu, Y. Wang, K. He, X.-C. Ma, Q.-K. Xue, *Advanced Materials* **30**, 1703062 (2018).

[114] M. Mogi, R. Yoshimi, A. Tsukazaki, K. Yasuda, Y. Kozuka, K.S. Takahashi, M. Kawasaki, Y. Tokura, *Applied Physics Letters* **107**, 182401 (2015).

[115] Y. Deng, Y. Yu, M.Z. Shi, Z. Guo, Z. Xu, J. Wang, X.H. Chen, Y. Zhang, *Science* **367**, 6480, 895-900 (2020).

[116] J.H. Van Vleck, *The Theory of Electronic and Magnetic Susceptibilities* (Oxford University Press, 1932).

[117] X. Kou, Y. Fan, M. Lang, P. Upadhyaya, K.L. Wang, *Solid State Communications* **215-216**, 34-53 (2015).

[118] C.Z. Chang, J. Zhang, M. Liu, Z. Zhang, X. Feng, K. Li, L.-L. Wang, X. Chen, X. Dai, Z. Fang, X.-L. Qi, S.-C. ZHang, Y. Wang, K. He, X.-C. Ma, Q.-K. Xue, *Advanced Materials* **25**, 1065-1070 (2013).

[119] M. Li, C.-Z. Chang, L. Wu, J. Tao, W. Zhao, M.H.W. Chan, J.S. Moodera, J. Li, Y. Zhu, *Physical Review Letters* **114**, 146802 (2015).

[120] X. Kou, L. He, M. Lang, Y. Fan, K. Wong, Y. Jiang, T. Nie, W. Jiang, P. Upadhyaya, Z. Xing, Y. Wang, F. Xiu, R.N. Schwartz, K.L. Wang, *Nano Letters* **13**, 4587-4596 (2013).

[121] Z. Zhou, C. Uher, M. Zabcik, P. Lostak, *Applied Physics Letters* **88**, 192502 (2006).

[122] W. Wang, Y. Ou, C. Liu, Y. Wang, K. He, Q.-K. Xue, W. Wu, *Nature Physics* **14**, 791-795 (2018).

[123] Y. Ou, C. Liu, L. Zhang, Y. Feng, G. Jiang, D. Zhao, Y. Zang, Q. Zhang, L. Gu, Y. Wang, K. He, X. Ma, Q.-K. Xue, *APL Materials* **4**, 086101 (2016).

[124] J. Wang, B. Lian, S.-C. Zhang, *Physica Scripta* **T164**, 014003 (2015).

[125] J. Wang, B. Lian, X.-L. Qi, S.-C. Zhang, *Physical Review B* **92**, 081107 (2015).

[126] M. Winnerlein, S. Schreyeck, S. Grauer, S. Rosenberger, K.M. Fijalkowski, C. Gould, K. Brunner, L.W. Molenkamp, *Physical Review Materials* **1**, 011201(R) (2017).

[127] M.V. Tarakina, S. Schreyeck, M. Duchamp, G. Karczewski, C. Gould, K. Brunner, R.E. Dunin-Borkowski, L.W. Molenkamp, *CrystEngComm* **19**, 3633 (2017).

[128] C.L. Richardson, J.M. Devine-Stoneman, G. Divitini, M.E. Vickers, C.-Z. Chang, M. Amado, J.S. Moodera, J.W.A. Robinson, *Scientific Reports* **7**, 12061 (2017).

[129] W. Li, M. Claassen, C.-Z. Chang, B. Moritz, T. Jia, C. Zhang, S. Rebec, J.J. Lee, M. Hashimoto, D.-H. Lu, R.G. Moore, J.S. Moodera, T.P. Devereaux, Z.-X. Shen, *Scientific Reports* **6**, 32732 (2016).

[130] C.-Z. Chang, W. Zhao, J. Li, J.K. Jain, C. Liu, J.S. Moodera, M.H.W. Chan, *Physical Review Letters* **117**, 126802 (2016).

[131] N. Nagaosa, J. Sinova, S. Onoda, A.H. MacDonald, N.P. Ong, *Reviews of Modern Physics* **82**, 1539 (2010).

[132] X. Feng, Y. Feng, J. Wang, Y. Ou, Z. Hao, C. Liu, Z. Zhang, L. Zhang, C. Lin, J. Liao, Y. Li, L.-L. Wang, S.-H. Ji, X. Chen, X. Ma, S.-C. Zhang, Y. Wang, K. He, Q.-K. Xue, *Advanced Materials* **28**, 30, 6386-6390 (2016).

[133] A. Arrott, *Physical Review* **108**, 1394 (1957).

[134] R. Watanabe, R. Yoshimi, M. Kawamura, M. Mogi, A. Tsukazaki, X.Z. Yu, K. Nakajima, K.S. Takahashi, M. Kawasaki, Y. Tokura, *Applied Physics Letters* **115**, 102403 (2019).

[135] J. Jiang, D. Xiao, F. Wang, J.-H. Shin, D. Andreoli, J. Zhang, R. Xiao, Y.-F. Zhao, M. Kayyalha, L. Zhang, K. Wang, J. Zang, C. Liu, N. Samarth, M.H.W. Chan, C.-Z. Chang, *Nature Materials* **19**, 732-737 (2020).

[136] J.S. Dyck, P. Hájek, P. Lostak, C. Uher, *Physical Review B* **65**, 115212 (2002).

[137] E.O. Lachman, A.F. Young, A. Richardella, J. Cuppens, H.R. Naren, Y. Anahory, A.Y. Meltzer, A. Kandala, S. Kempinger, Y. Myasoedov, M.E. Huber, N. Samarth, E. Zeldov, *Science Advances* **1**, 10, e1500740 (2015).

[138] Y.-J. Chien, *Transition Metal-Doped Sb_2Te_3 and Bi_2Sb_3 Diluted Magnetic Semiconductors*, PhD thesis, The University of Michigan (2007).

[139] C.-X. Liu, H. Zhang, B. Yan, X.-L. Qi, T. Frauenheim, X. Dai, Z. Fang, S.-C. Zhang, *Physical Review B* **81**, 041307 (2010).

[140] L. Pan, X. Liu, Q.L. He, A. Stern, G. Yin, X. Che, Q. Shao, P. Zhang, P. Deng, C.-Y. Yang, B. Casas, E.S. Choi, J. Xia, X. Kou, K.L. Wang, *Scientific Reports* **6**, 25, eaaz3595 (2020).

[141] J. Wang, B. Lian, S.-C.-Zhang, *Physical Review B* **89**, 085106 (2014).

[142] M. Offidani, A. Ferreira, *arXiv* 1801.07713v3 (2018).

[143] J. Safarian, T.A. Engh, *Metallurgical and Materials Transactions A* **44**, 747-753 (2013).

[144] J.W. Arblaster, *Journal of Phase Equilibria and Diffusion* **38**, 51-64 (2017).

[145] H.-J. Kim, K.-S. Kim, J.-F. Wang, M. Sasaki, N. Satoh, A. Ohnishi, M. Kitaura, M. Yang, L. Li, *Physical Review Letters* **111**, 246603 (2013).

[146] C. Li, J.C. de Boer, B. de Ronde, S.V. Ramankutty, E. van Heumen, Y. Huang, A. de Visser, A.A. Golubov, M.S. Golden, A. Brinkman, *Nature Materials* **17**, 875–880 (2018).

[147] B.J. Yang, N. Nagaosa, *Nature Communications* **5**, 4898 (2014).

[148] S.A. Parameswaran, T. Grover, D.A. Abanin, D.A. Pesin, A. Vishwanath, *Physical Review X* **4**, 031035 (2014).

[149] P.J.W. Moll, N.L. Nair, T. Helm, A.C. Potter, I. Kimchi, A. Vishwanath, J.G. Analytis, *Nature* **535**, 266–270 (2016).

[150] A.A. Zyuzin, A.A. Burkov *Physical Review B* **86**, 115133 (2012).

[151] H. Li, H. He, H.Z. Lu, H. Zhang, H. Liu, R. Ma, Z. Fan, S.Q. Shen, J. Wang *Nature Communications* **7**, 10301 (2016).

[152] C.Z. Li, L.X. Wang, H. Liu, J. Wang, Z.M. Liao, D.P. Yu, *Nature Communications* **6**, 10137 (2015).

[153] Y. Liu, R.E. Allen, *Physical Review B* **52-3**, 1566-1577 (2017).

[154] D. Shin, Y. Lee, M. Sasaki, Y.H. Jeong, F. Weickert, J.B. Betts, H.-J. Kim, K.-S. Kim, J. Kim *Nature Materials* **16**, 1096–1099 (2017).

[155] M. Hirschberger, S. Kushwaha, Z. Wang, Q. Gibson, S. Liang, C.A. Belvin, B.A. Bernevig, R.J. Cava, N.P. Ong, *Nature Materials* **15**, 1161–1165 (2016).

[156] R.D. dos Reis, M.O Ajeesh, N. Kumar, F. Arnold, C. Shekhar, M. Naumann, M. Schmidt, M. Nicklas, E. Hassinger, *New Journal of Physics* **18** (2016).

[157] D. Halbertal, J. Cuppens, M. Ben Shalom, L. Embon, N. Shadmi, Y. Anahory, H.R. Naren, J. Sarkar, A. Uri, Y. Ronen, Y. Myasoedov, L.S. Levitov, E. Joselevich, A.K. Geim, E. Zeldov, *Nature* **539**, 407-410 (2016).

[158] H. Weinstock, *SQUID Sensors: Fundamentals, Fabrication and Applications* (Kluwer Academic Publishers, 1996).

[159] D.A. Pesin, A.H. MacDonald, *Physical Review Letters* **111**, 016801 (2013).

[160] B. de Ronde, C. Li, Y. Huang, A. Brinkman, *Nanomaterials* **10**(4), 794 (2020).

[161] N. Poccia, T.I. Baturina, F. Coneri, C.G. Molenaar, X.R. Wang, G. Bianconi, A. Brinkman, H. Hilgenkamp, A.A. Golubov, V.M. Vinokur, *Science* **349**, 6253, 1202-1205 (2015).

[162] J. Bardeen, L.N. Cooper, J.R. Schrieffer, *Physical Review* **108**(5), 1175-1204 (1957).

[163] D.E. McCumber, *Journal of Applied Physics* **39**, 3113 (1968).

[164] H. Courtois, M. Meschke, J.T. Peltonen, and J.P. Pekola, *Physical Review Letters* **101**, 067002 (2008).

[165] G.E. Blonder, M. Tinkham, T.M. Klapwijk, *Physical Review B* **25**, 4515 (1982).

[166] G. Niebler, G. Cuniberti, T. Novotný, *Superconductor Science and Technology* **22**, 085016 (2009).

[167] G. Kunakova, T. Bauch, E. Trabaldo, J. Andzane, D. Erts, F. Lombardi, *Applied Physics Letters* **115**, 172601 (2019).

[168] V. Barzykin, A.M. Zagoskin, *Superlattices and Microstructures* **25**, 5-6, 797-807 (1999).

[169] C.G. Molenaar, D.P. Leusink, X.L. Wang, A. Brinkman, *Superconductor Science and Technology* **27**, 104003 (2014).

[170] B.W. Maxfield, W.L. McLean, *Physical Review* **139**, A1515 (1965).

[171] K. Le Calvez, L. Veyrat, F. Gay, P. Plaindoux, C.B. Winkelmann, H. Courtois, B. Sacépé, *Communications Physics* **2**, 4 (2019).

[172] P. Schüffelgen, D. Rosenbach, C. Li, T.W. Schmitt, M. Schleenvoigt, A.R. Jalil, S. Schmitt, J. Kölzer, M. Wang, B. Bennemann, U. Parlak, L. Kibkalo, S. Trellenkamp, T. Grap, D. Meertens, M. Luysberg, G. Mussler, E. Berenschot, N. Tas, A.A. Golubov, A. Brinkman, T. Schäpers, D. Grützmacher, *Nature Nanotechnology* **14**, 825-831 (2019).

[173] K.D. Usadel, *Physical Review Letters* **25**, 507 (1970).

[174] M. Yu. Kuprianov, V.F. Lukichev, *Journal of Experimental and Theoretical Physics* **94**, 149 (1988).

[175] B.A. Assaf, T. Phuphachong, V.V. Volobuev, A. Inhofer, G. Bauer, G. Springholz, L.A. de Vaulchier, Y. Guldner, *Scientific Reports* **6**, 20323 (2016).

[176] M. Lankhorst, GitHub - martijnLankhorst/JJAsim: Josephson circuit simulator for arrays `https://github.com/martijnLankhorst/JJAsim`.

[177] M.M. Otrokov, I.I. Klimovskikh, H. Bentmann, D. Estyunin, A. Zeugner, Z.S. Aliev, S. Gaß, A.U.B. Wolter, A.V. Koroleva, A.M. Shikin, M. Blanco-Rey, M. Holffmann, I.P. Rusinov, A. Yu. Vyazovskaya, S.V. Eremeev, Y.M. Koroteev, V.M. Kuznetsov, F. Freyse,

J. Sánchez-Barriga, I.R. Amiraslanov, M.B. Babanly, N.T. Mamedov, N.A. Abdullayev, V.N. Zverev, A. Alfonsov, V. Kataev, B. Büchner, E.F. Schwier, S. Kumar, A. Kimura, L. Petaccia, G. Di Santo, R.C. Vidal, S. Schatz, K. Kißner, M. Ünzelmann, C.H. Min, S. Moser, T.R.F. Peixoto, F. Reinert, A. Ernst, P.M. Echenique, A. Isaeva, E.V. Chulkov, *Nature* **576**, 416-422 (2019).

[178] Y. Gong, J. Guo, J. Li, K. Zhu, M. Liao, X. Liu, Q. Zhang, L. Gu, L. Tang, X. Feng, D. Zhang, W. Li, C. Song, L. Wang, P. Yu, X. Chen, Y. Wang, H. Yao, W. Duan, Y. Xu, S.-C. Zhang, X. Ma, Q.-K. Xue, K. He, *Chinese Physics Letters* **36**, 076801 (2019).

[179] C. Hu, K.N. Gordon, P. Liu, J. Liu, X. Zhou, P. Hao, D. Narayan, E. Emmanouilidou, H. Sun, Y. Liu, H. Brawer, A.P. Ramirez, L. Ding, H. Cao, Q. Liu, D. Dessau, N. Ni, *Nature Communications* **11**, 97 (2020).

[180] J.-Q. Yan, Q. Zhang, T. Heitmann, Z. Huang, K.Y. Chen, J.-G. Cheng, W. Wu, D. Vaknin, B.C. Sales, R.J. McQueeney, *Physical Review Materials* **3**, 064202 (2019).